UCLouvain

École polytechnique de Louvain

Zero-point band gap renormalization in semiconductors for optoelectronic applications

Author: **André Magerat**
Supervisor: **Xavier Gonze**
Readers: **Samuel Ponce, Guillaume Brunin, Laurent Francis**
Academic year 2024–2025
Master [120] in Physical Engineering

Acknowledgements

I would like first and foremost to thank my supervisor, Mr Gonze. Not only was he available for each step of the way, but also the precious advices he gave me allowed me to take this work as far as I possibly could. With both technical skills and pedagogy, Mr Gonze has cleared every problem and issue I encountered and for that, I am grateful beyond words.

A special thank you to the readers and members of the jury, Mr Poncé, Mr Brunin and Mr Francis for your feedbacks on this present work. Your suggestions and questions allowed me to better understand the topic and to correct errors and misconceptions.

Finally, a huge thank you to the numerous assistants and researchers at the MODL division of UCL who help this master thesis to come to life. Among those, thanks to Julien Bouquiaux, for setting up Abipy in the Nic5 server, thanks to Samare Rostami for explaining and troubleshooting the implementation of the QHA for this work.

Disclaimer

During the redaction of this work, several tools and AI were used :

- ChatGPT was used to enhance the vocabulary and grammar of the text. Some traduction was also done by this software, along with the explanation of several theoretical notions,
- Copilot was used for the 'coding part' of this work. It produced some of the graphics (for the extraction of the ZPR from the q points convergence).
- Abipy and Abiflow were used respectively for the post-processing of the results computed by ABINIT and for the management of large dataset of computations being run simultaneous.

List of Acronyms

- **AHC** : Allen-Hein-Cardona (theory)
- **BO** : Born-Oppenheimer
- **BZ** : Brillouin Zone
- **CPU** : Central Processing Unit
- **DFPT** : Density Functional Perturbation Theory
- **DFT** : Density Functional Theory
- **EPI** : Electron-Phonon Interaction
- **FFT** : Fast Fourier Transform
- **GGA** : Generalized Gradient Approximation
- **IR** : Infrared
- **LDA** : Local Density Approximation
- **LED** : Light Emitting Diode
- **MEMS** : Micro Electronic Mechanical Systems
- **ML** : Machine Learning
- **MP** : Monkhorst-Pack (grid)
- **OTMS** : On The Mass Shell
- **PBE** : Perdew-Burke-Ernzerhof (pseudopotential)
- **PCE** : Power Conversion Efficiency
- **QHA** : Quasi Harmonic Approximation
- **QP** : Quasi-Particle
- **UV** : Ultraviolet
- **V-ZSISA** : Volumetric Zero Static Internal Stress Approximation
- **VDW** : Van Der Waals (forces)
- **ZPLE** : Zero Point Lattice Expansion
- **ZPR** : Zero Point Renormalization
- **ZPVE** : Zero Point Vibrational Energy

Contents

1 Introduction and motivation

One of the major challenges in this 21st century is the energy demand and supply. Lowering our energy needs while using it more efficiently along with durable and clean energy sources is key to achieving ecological transition from fossil fuels to 'green' energy. Several solutions are being proposed, studied and implemented everywhere in the world (solar cells, biomass, hydroelectricity, wind turbines, etc). Among those, solar panels have the advantage of being cheap (compared to a nuclear power plant). Because they provide very little electricity (about a household worth for an installation of few square meters), they are typically used for residential purpose and do not yet meet the energetical needs of typical industrial applications. In addition, they are very quick to manufacture and install. Progress and innovations are steady in this field of research and each new generation of solar cells is directly implemented into the energetic landscape of the world. Figure 1 displays the efficiency increase from 1980 to 2020 for different solar cells.

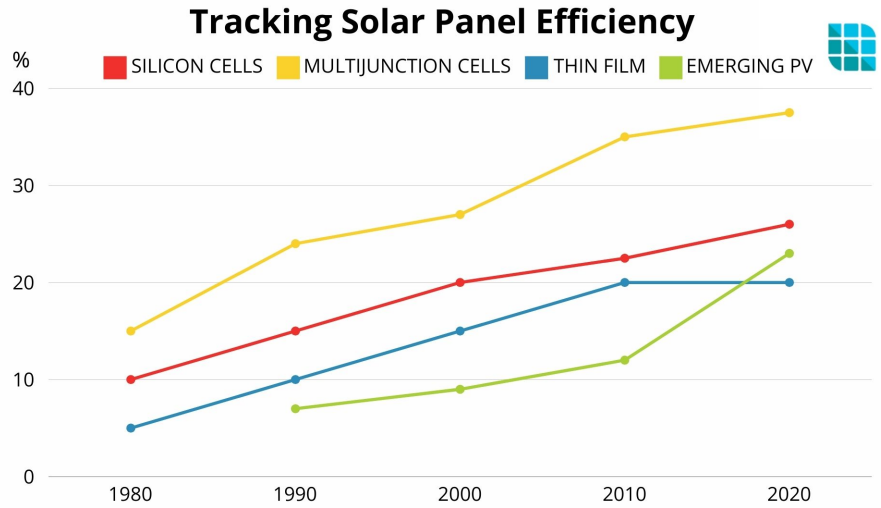

Figure 1: Solar cells efficiency throughout the years for several technologies (emerging solar cells being perovskite solar cells), from Ref. [1].

Part of this increase of efficiency is possible via the discovery of new materials having good optoelectronic properties. Semiconductors show highly tunable electronic properties, important mobilities and - in general - low electrical losses. What is more, their band gap is within the visible range and governs both optical and electrical properties (ideal for photovoltaïc conductive layers).

In the past, the selection of a material was done via a trial-and-error approach. This was a long process and the return on investment was even longer, making this method quite inefficient. Recently, a new approach has been found toward the research of materials having specific properties (mechanical, electrical, etc). Today, new initiatives based on the collaboration between different scientific communities and the availability of computational resources have revolutionized the discovery of materials. High-throughput approaches are used to select from tens of thousands of compounds, based on their properties, the best fit for new technological prospects. In addition to this simple searching algorithm, several machine learning techniques can be coupled with those databases to identify new compounds, different from the ones available in the database, and potentially better suited for specific industrial goals, such as the production of efficient solar cells.

The Material Project website (from the Materials Genome Initiative) is one example among many gathering more than 150.000 materials and aiming to facilitate the access to crystal/molecule informations and properties.

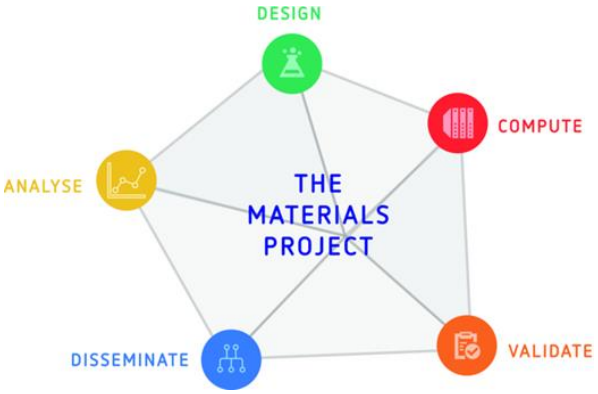

Figure 2: Overview of the Materials Project thrusts. Computed data are validated, disseminated to the user community, and fed into analysis that is ultimately used to design new compounds for subsequent computations, from Ref. [2].

This new, exciting, approach opens the door to plenty of creative ways to couple material science and computer science. The proper modelling of relevant material properties becomes more important than ever and the goal of this work is to contribute to this state-of-the-art modelling of material properties. This present work is part of an effort to correctly characterize the band gap renormalization in ten semiconductors from Density Functional Theory (DFT). It is well known that DFT often underestimates the band gap in solids [3]. One possible correction (the most common one) is the GW method. But to obtain an accurate band gap, a supplementary correction must be included. This correction is the subject of this work : the zero point renormalization energy. The knowledge of the zero point energy contributes to the accurate modelling of semiconductor band gap, a very much needed property in optoelectronic applications. This zero point renormalization energy has two contributions, both detailed and investigated in this work : the energy level renormalization from electron-phonon interaction and the phonon-induced lattice expansion.

The zero point renormalization from electron phonon interactions is developed in the non-adiabatic AHC formalism. This results in a self-energy made of two terms : the Fan-Migdal term and the Debye-Waller term. The thermal lattice expansion of materials is investigated via the quasi harmonic method, resulting on a lattice expansion contribution both at $T = 0$ K and for $T > 0$ K. Both mechanisms have been studied within the ABINIT software. The temperature dependence of the band gap is also computed from those two contributions

To keep this work clear and concise, this present report is divided in several sections. Section 2 will introduce the basic theoretical notions needed to understand the main figures of merit in this work. The band gap and its theoretical temperature dependence will be presented, as well as the formalism for both the electron-phonon interaction and the origin of thermal expansion in materials. Section 3 will present the semiconductors studied in this work, along with their main optical and electronic characteristics. Section 4 will detail the parameters chosen for the different simulations and the typical workflows computed in ABINIT. Finally, section 5 will analyze the results obtained for both contributions and put them in perspective to recent experimental data.

2 Theoretical Background

The purpose of this section is to give the reader a first understanding about the physical concepts explored in this work. As the central property of materials studied here is the electronic band gap, a brief explanation will introduce it and outline its importance in today's technological prospects. Then, since density functional theory will be used throughout this work, a simple introduction to this simulation method will ensure the reader a correct understanding of the main tool providing results. As previously explained, this work is divided in two main branches : the electron-phonon interactions (EPI) band gap correction and the lattice expansion band gap correction. In this section, the electron-phonon interaction will be first derived from quantum mechanical approach, then explained via its implementation into ABINIT. Following the EPI, some theoretical notions about the zero point lattice expansion and the quasi harmonic approximation (QHA) [4] will finally end this section.

2.1 Electronic Band Gap

The electronic band gap of a material is, without a doubt, one of the most important properties to consider when designing an electronic device. It governs the electric behavior (insulators, semiconductors or conductors), the optoelectronic properties (wavelengths emission, transparency, etc) and much more.

2.1.1 Band gap computation

The band gap calculation of a crystalline structure can be formally computed in solid state physics using the time's independent Schödinger equation :

$$\hat{H}\Phi(r) = E\Phi(r) \tag{1}$$

where $\hat{H}$ is the Hamiltonian operator for a single electron:

$$\hat{H} = -\frac{\hbar^2}{2m}\nabla^2 + V(\mathbf{r}), \tag{2}$$

with $V(\mathbf{r})$ a simple ionic potential, depending on the charge and position of the ions considered as well as the interaction with other electrons and $-\frac{\hbar^2}{2m}\nabla^2$, the kinetic energy term. Assuming a perfect crystalline structure, the wave function can be re-written with Bloch's formalism (in order to use the periodicity of the ionic potential):

$$\Psi_{n\mathbf{k}}(\mathbf{r}) = e^{i\mathbf{k}.\mathbf{r}}u_{n\mathbf{k}}(\mathbf{r}), \tag{3}$$

with k the wavevector and n the electronic band considered. The Bloch function $u_{n\mathbf{k}}(\mathbf{r})$ is periodic with respect to the crystal lattice : $u_{n\mathbf{k}}(\mathbf{r}) = u_{n\mathbf{k}}(\mathbf{r} - \mathbf{R})$.

Solving Equation 1, one can obtain a discrete number of energy levels (grouped into bands) allowed for each point in the Brillouin zone (depending on the wavevector $\mathbf{k}$). Usually, the energy is shown with straight lines between high symmetry points in the Brillouin zone such as Fig 3.

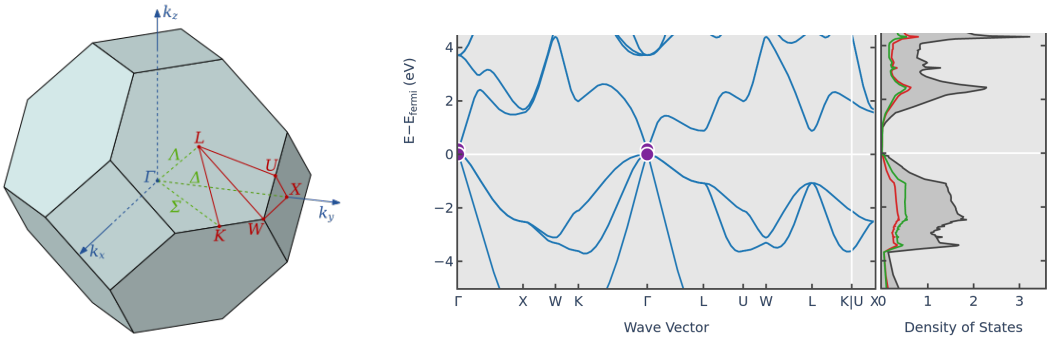

(a) (b) (c)

Figure 3: (a) Brillouin zone for cubic face centered materials with high symmetry points (b) Computed electronic band structure for cubic face centered GaAs (c) Density of states for cubic face centered GaAs (from Materials project website, mp-2534 [2]).

Looking at the density of state (Figure 3c), there is a region with almost no available state (in fact, just above $E = E_{fermi}$, there is no state at all). This is understandably called the band gap. The width of the band gap, E_g determines what type of conductor the material is :

- $E_g > 3$ eV : The maximum of the valence band and the minimum of the conduction band are energetically too far apart, no carrier can pass through the band gap. The material is an insulator.
- 0 eV $> E_g < 3$ eV : Small band gap, tunable with temperature or doping level (for a high doping level, above $\sim 10^{18} cm^{-3}$). At T = 0 K, it behaves like an insulator. The material is a semiconductor.
- $E_g = 0$ eV: No band gap, the conduction band and the valence band overlap leading to high conductivity. The material is a metal.

The bands are filled up to the Fermi energy. For a PV cell, when a carrier gains energy from a photon with a frequency corresponding to the band gap width (or a higher energy), it can jump from the top of the valence band to the minimum of the conduction band, allowing the current to flow. The band gap can either be direct (if the maximum of the valence band and the minimum to the conduction band are located at the same **k** vector) or indirect (if the maximum of the valence band and the minimum of the conduction band are located at different **k** vectors). In the case of an indirect band gap, the carrier also needs phonon momentum (meaning energy from lattice vibration) to jump energy state.

Not only does it affect the electrical behavior of a material, but the band gap also explains a lot about the optical properties of a compound. Semiconductors and insulators can only absorb light above a specific frequency, which depends on their band gap with the relation :

$$E_{photon} = h\nu > E_g, \tag{4}$$

with h, the Planck constant.
That is why, metals having no band gap (no forbidden energy state electron can be in), they appear shiny (thanks to their high density of free electrons) or reflective meaning they absorb a wide range of the light spectrum. Meanwhile, wide band gap materials such as glass ($E_g \approx 9eV$) or diamond ($E_g = 5.47eV$) are often transparent to visible light (their band gap is much larger than the energy of visible photons). Semiconductors can emit light depending on their band gap as well, with a wavelength given by the relation :

$$\lambda_{photon} = \frac{hc}{E_g}, \tag{5}$$

with c, the speed of light in vacuum. This is why narrow band gap semiconductors emit longer wavelengths (IR, red) while wide band gap semiconductors emit shorter wavelength (blue, UV).

This simple model does not take into account every solid-state phenomena and interactions in the crystal. It typically ignores electrons-lattice vibrations (phonons) interactions, the coupling between spin and orbital moment as well as electron-electron interaction. What is more, it only works under severe assumptions such as assuming infinite crystal without defects or interfaces. However, it suffices to explain the underlying physics behind the electronic band gap and its importance in semiconductor design for electronic applications.

This analysis is valid at any given temperature (except T = 0 K, for which semiconductors behaves like insulators). But how does the band gap evolves with a change of temperature? And can it be predicted? The band gap temperature dependance has been exhaustively studied since the sixties.

2.1.2 Band gap temperature dependence

In this work, the focus will be put on the temperature dependence of E_g, strongly depending on two phenomena : the electron-phonon interaction and the thermal expansion of the lattice. Experimentally, Y.P. Varshni proposed in 1967 this relation (with α and β, two constants and E_0, the band gap under the T=0K regime) [5]:

$$E_g(T) = E_0 - \frac{\alpha T^2}{T+\beta}. \tag{6}$$

However, this relation while useful for a handful of semiconductors (InAs, InP, Si, Ge, 6H-SiC, GaAs), does not cover every case. Notably, semiconductor band gaps appear to be independent of the temperature for a large range at low temperature, while equation 6 clearly states a quadratic relation. On top of that, the theoretical basis for this relation is rather weak (according to K. O 'Donnell and his colleagues, β, which is supposed to be related to the Debye temperature, may in certain cases be negative [6]). To remedy those issues, A. Manoogian and A. Leclerc issued in 1979 a correction to Varshni's work. The band gap temperature dependence could be written [7] :

$$E_g(T) = E_0^D(1 + AT^X) + B\left(\theta_1 \coth\left(\frac{\theta_1}{2T}\right) + \theta_2 \coth\left(\frac{\theta_2}{2T}\right)\right), \tag{7}$$

with $A, B, X, \theta_1, \theta_2$ empirical constants. The first term aims to replicate the effect of the lattice dilatation via the two parameters A and X, while the second term represents the contribution from the electron-phonon interaction (with θ_1 one effective optical mode and θ_2 one effective acoustic mode being treated separately). $\theta = h\nu/k$, with ν, the average phonon frequency. One of the biggest drawbacks of this model is the simultaneous fitting of 6 different parameters, which can be computationally demanding. About ten years later, in 1990, K. P. O 'Donnell and X. Chen presented yet another semi-empirical formula for the temperature dependence of the band gap [6]:

$$E_g(T) = E_g(0) - S\langle\hbar\omega\rangle\left[\coth\left(\frac{\langle\hbar\omega\rangle}{2k_BT}\right) - 1\right], \tag{8}$$

with $\langle\hbar\omega\rangle$, the average phonon energy and S, a dimensionless coupling constant. This was proven to be giving better results than Varshni's expression. Finally, efforts were made in 2002 by Pässler and coworkers [8] to develop a novel dispersion-related model for the temperature dependencies of fundamental band gaps. It notably takes into account $\theta = \langle\hbar\bar{\omega}\rangle / k_B$ ($\bar{\omega}$ being the average phonon pulsation) and the average phonon temperature as well as the phonon dispersion coefficient $\Delta = \sqrt{\langle(\hbar\omega - \hbar\bar{\omega})^2\rangle}/\hbar\bar{\omega}$:

$$\begin{aligned} E_g(T) =& E_g(0) - \alpha\theta\frac{1-3\Delta^2}{exp(\theta/T)-1} \\ &+\alpha\theta\frac{3\Delta^2}{2}\left(\sqrt[6]{1 + \frac{\pi^2}{3(1+\Delta^2)}\left(\frac{2T}{\theta}\right)^2 + \frac{3\Delta^2-1}{4}\left(\frac{2T}{\theta}\right)^3 + \frac{8}{3}\left(\frac{2T}{\theta}\right)^4 + \left(\frac{2T}{\theta}\right)^6} - 1\right). \end{aligned} \tag{9}$$

It is worth noting that there exists plenty of other models, all refining or correcting Varshni's empirical model (due to its inability to correctly predict band gap behavior at very low or high temperature, or in materials with strong electron-phonon interaction). However, as outlined by those few models, the band gap of materials decrease with increasing temperature. That is, except for few exeptions such as $CH_3NH_3PbI_3$, a metal–halide hybrid perovskite. For this materials, the band gap opens with increasing temperature. This behavior has not been described by any model [9].

Of course, when considering band gap temperature dependence, experimental data cannot disentangle precisely the contribution of the thermal dilatation or the electron-phonon interaction. Those points will be detailed in the following sections.

2.2 Density Functional Theory

Density functional theory is one of the most popular simulation technique in material science. Used in multiple domains (such as research, in the academic world, in the industry) its capability is not to be proven. DFT can be used for a wide range of goals. It can accurately describe the energy ground state of a molecule but also find optical, mechanical, vibrational properties of a given material.

One of the main advantages of the DFT (and ab initio methods in general) is that it only requires informations about the unit cell and approximate location of the nuclei of the considered crystal and the pseudo-potential of its constituent to derive all its properties. Absolutely no other knowledge about the material is needed. However those methods have a rather high computational cost that is not to be underestimated.

2.2.1 DFT Working principle

The goal is to characterize a system of N electrons evolving in a potential generated by ions considered as fixed (under the Born-Oppenheimer approximation). Such a system of electron can be described by a wavefunction $\Phi(\mathbf{r_1}, .., \mathbf{r_N})$ solving the time-independent Schödinger equation :

$$\hat{H}\Phi = E\Phi, \tag{10}$$

$$\left(\sum_{ij}^{N} \frac{-\hbar^2 \nabla_i^2}{2m_i} + V(\mathbf{r}_i) + U(\mathbf{r}_i, \mathbf{r}_j) \right) \Phi = E\Phi, \tag{11}$$

where the first term describes the kinetic energy of the moving electrons, the second term is the potential induced by the ions seen by the electrons and the third term represents the potential induced by other electrons.

Solving exactly this equation for a small number of electrons in simple potential is easy enough. However, as the number of electrons N increases, the number of operations needed becomes too demanding in computational resources and the resolution of more complex systems is challenging (sometimes even impossible, depending on the system and the ressources allocated). To tackle this problem, DFT was developed.

Equation (11) can be easily treated if the $U(\mathbf{r}_i, \diagdown_j)$ term is neglected. That is, if the interaction between the electrons is suppressed. The problem become then solvable by separation of variable ($\Phi(\mathbf{r_1}, .., \mathbf{r_N}) = \phi(\mathbf{r_1})\phi(\mathbf{r_2})...\phi(\mathbf{r_N})$) and the eigenvalues are linear combinations of products of solutions of 1-electron Schrödinger equations.
DFT rests on the idea that the ground-state properties of a N electrons system are solely determined by its electron density $\rho(r)$, including the electron-electron interaction effects. $V_{eff}(r)$ is the effective average electrostatic potential created by the electrons. According to Kohn and Sham, the electron density can be written as a function of single-particle orbitals $\phi_i(\mathbf{r})$ [10]:

$$\rho(\mathbf{r}) = \sum_{i}^{N} |\phi_i(\mathbf{r})|^2. \tag{12}$$

One can rewrite the Schrödinger equation with the new effective potential seen by one electron :

$$\left(-\frac{-\hbar^2}{2m}\nabla^2 + V_{eff}(\mathbf{r})\right)\phi_i(\mathbf{r}) = \epsilon_i\phi_i(\mathbf{r}), \tag{13}$$

$$V_{eff}(\mathbf{r}) = V_{nucl}(\mathbf{r}) + \int \frac{\rho(\mathbf{r}')}{|\mathbf{r}-\mathbf{r}'|}d^3\mathbf{r}' + V_{XC}[\rho(\mathbf{r})], \tag{14}$$

where V_{nucl} is the external potential created by the nuclei, the second term is called the Hartree potential and acts as the electron-electron repulsion operator and V_{XC} is the exchange correlation functional, including the effect of the N particles interactions.

The most complex term to approximate in this equation is V_{XC}, the exchange correlation functional. It includes both the electron exchange effects (from Pauli exclusion principle, stating that no 2 electrons can exist in the same quantum state) and the correlation effect (how much one electron moving is affecting the other electrons). Since its exact form is not known, some approximation has to be made. Among the most common ones, there are the Local Density Approximation (LDA) [11] and the Generalized Gradient Approximation (GGA) [12]. The choice of this term affects a great deal the final result of the calculations since it corrects the simplified picture given by the Hartree energy.

The core mechanism of the DFT is the relation between $\rho(\mathbf{r})$, $\phi_i(\mathbf{r})$ and $V_{eff}(\mathbf{r})$. To determine those quantities, softwares applications use a self-consistency cycle to solve the Kohn-Sham equations iteratively. An initial guess about the electron density $\rho(\mathbf{r})$ is used to compute the corresponding $V_{eff}(\mathbf{r})$ in equation (14), which is then replaced in equation (13) to evaluate the eigenvectors $\phi_i(\mathbf{r})$. With those new wavefunctions, a new electron density can be found and so the cycle repeats until convergence is reached with a proper accuracy. This self-consistency cycle is shown on Figure 4

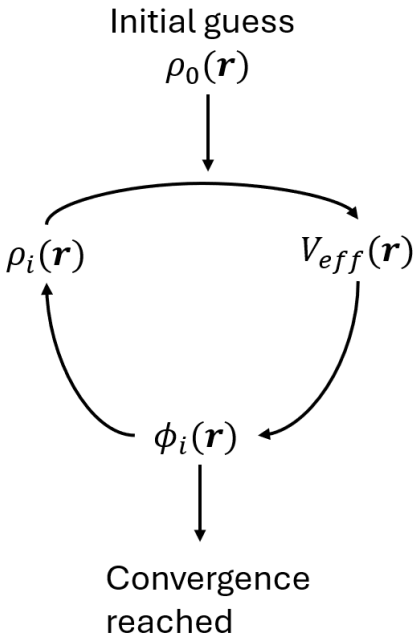

Figure 4: Schematic view of the main DFT iteration cycle.

To stop the cycle, the convergence criteria can either be on the relative error between two iterations on the wavefunction, the total energy, the total potential, the atomic forces. This choice affects the quality of the result as well and should be considered carefully.

2.2.2 DFT Band Gap Error

But Density Functional Theory (DFT), with all its elegance, is not without flaws. Indeed, there are situations in which DFT does not perform well and is not a reliable method for precise results. One of the biggest drawbacks of this theory is its usual underestimation of the electronic band gap value. This is a well-known problem to which there are existing solutions.

While the ground state energy levels are accurately described with simple exchange-correlation functionals, the energy levels of excited states within the Kohn-Sham exchange-correlation energy and potential are, at best, imprecise. The predicted band gap for insulators and semiconductors can range from few tens of eV to few eV off.

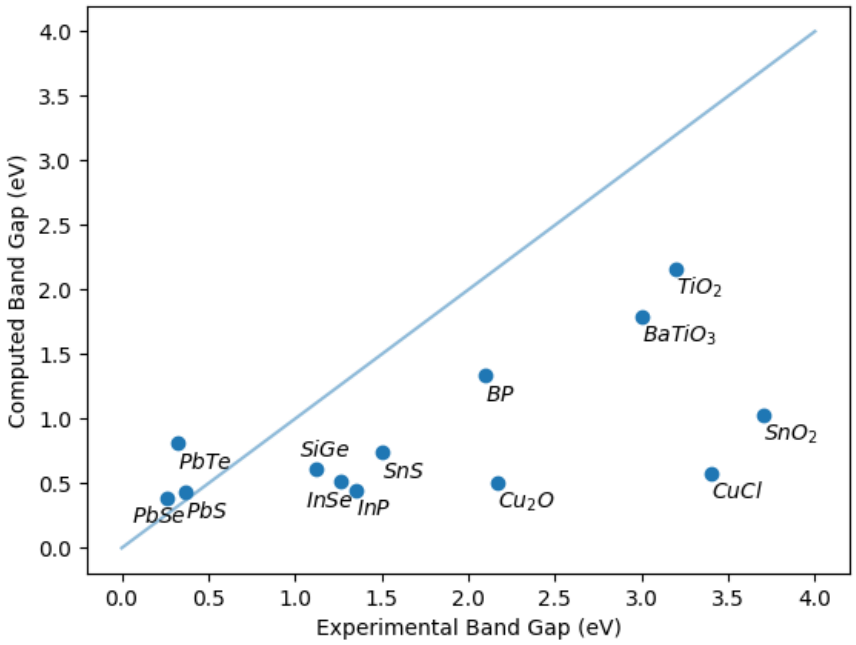

Figure 5: DFT band gaps (computed in this work) versus experimental band gaps for bulk semiconductors.

Figure 5 illustrates this problem for a dozen different semiconductors. The computed band gap have been found using norm-conserving pseudo-potentials from the Pseudo Dojo website [13] and there is no spin-orbit coupling (including the SOC would decrease the band gap value for heavy elements, such as lead). Let us note that for the experimental band gap, the spin-orbit coupling is obviously included (as there is no way to isolate its contribution), making this comparison questionable. However, this should not affect the results obtained, except for the PbX elements. The structures were relaxed beforehand and the ground state parameters have been converged with respect to the total energy/final lattice parameters. The SiGe is an alloy for which there is two atoms in the unit cell (one of silicon and one of germanium). All experimental band gaps were measured at room temperature.

One correction to this underestimation of the band gap value is the GW approximation [14]. The GW approximation incorporates the many-body interactions effect from electrons in the prediction of quasiparticle energies (lacking in the ground-state energies estimated by DFT). However, this technique is not used in the present work. One point worth mentioning is that GW approximation is time-consuming (much more than Kohn-Sham energies) and requires lots of CPU power.

2.3 Harmonic approximation and phonons

As a major part of this work is focused on the electron-phonon interactions as well as the zero point lattice expansion, it seems useful to briefly introduce the 'phonon' concept, for it is a key to understanding the vibrational properties of crystals.

In classical mechanics, to represent a vibrational motion (a phonon) propagating in the lattice, one can make the assumption that the lattice of atoms oscillates at a single frequency. To do so, the lattice is assumed to be a 3D assembly of $3N$ atoms, each having a mass m, linked together by springs (with a spring constant k) of length a. Such a system would require a 4D plot to represent the displacement of ions, which is not convenient. Instead, the main ideas are expressed via a simple unidirectional model, for which analytical solutions are easily understood.

Let us examine such dynamical behavior for a simplified model of a 1D chain (neglecting the influence of the y and z direction forces). The displacement of the n^{th} atom of this network in the x-direction can be written using recurrence equations :

$$-2ku_n + k(u_{n+1} + u_{n-1}) = m\frac{d^2u_n}{dt^2}, \tag{15}$$

with the indices $n+1$, $n-1$ refers to atoms respectively before and after the n^{th} atom. To solve this set of coupled equations, the solution is of the form :

$$u_n = \Re\left[\sum_{k=1}^{M} A_k e^{i(kna+\omega_k t)},\right] \tag{16}$$

$$u_n = \Re\left[\sum_{k=1}^{M} A_k \left[\cos(kna+\omega_k t) + i\sin(kna+\omega_k t)\right]\right]. \tag{17}$$

$$u_n = \sum_{k=1}^{M} A_k \cos(kna+\omega_k t) \tag{18}$$

with $M = Na/2\pi$ for $k = 0, 1, ..., N$ and A_k, a multiplication factor (coming from the discrete Fourier Transform). This expression emphasizes the wavy nature of the phonons. They can be seen as a sum of cosinus oscillating at a specific frequency around the equilibrium position. ω_k is the dispersion relation between the angular frequency and the wavenumber k (known as a normal mode):

$$\omega_k = \sqrt{\frac{2k}{m}(1-\cos(ka))}. \tag{19}$$

However, for a linear chain made of two alternating atoms (of mass m_1 and m_2), the dispersion relation is easily shown (Figure 6).

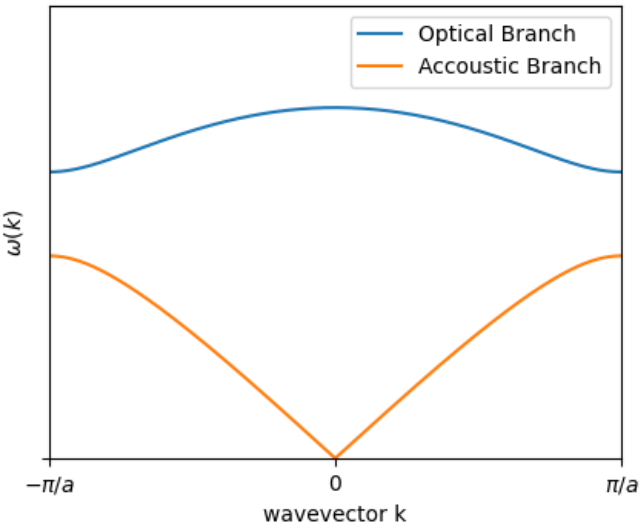

Figure 6: Dispersion relation for a diatomic chain in a classical mechanics treatment.

Solving the recurrence equation, the solution has two distinct modes (acoustic, in which atoms moves in the same direction, and optical, in which atoms motion is out of phase). This simple, harmonic model of the lattice motion is very useful and has already proven itself to be reliable within DFPT in numerous studies.

Density Functional Perturbation Theory (DFPT) is the theoretical framework used to compute the response functions of materials when subject to small perturbations. The applied perturbations are typically an external electric/magnetic field, an atomic displacement, strains, etc. The responses can be first order (forces, stress, moments), second order (piezoelectricity, born effective charges, elastic constants) or higher order (non linear dielectric susceptibility, phonon-phonon interactions, etc). The full derivation of the DFPT implementation is not the topic of this work, thus is not shown here.

However, to explore thermal expansion coefficient from first principles, this simple harmonic model is not enough and an extra approximation has to be made : the quasi-harmonic approximation (see Sec. 2.6).

2.4 Electron-phonon interaction

Electron-phonon interaction (EPI) is responsible for a wide range of properties in solid-state physics. From common phenomena like thermal and temperature dependent electric conductivity to more exotic ones such as superconductivity or phonon assisted optical processes. This work will focus on the temperature dependence and the zero-point renormalization of the band gap. Indeed, EPI is responsible for many temperature dependent properties in the solid, but it also significantly contributes to the modification, through zero-point motion at T = 0K (called Zero-Point Renormalization, ZPR).

A complete theory of the electronic energy shift due to atomic vibrations was formulated in 1979 by Allen, Heine and Cardona (leading to a theory named AHC) [15] [16] [17]. Their starting point was the earlier attempts of Fan (1951)[18][19] in which the modification of the wavefunctions due to atomic motion had been included, giving an 'electron self-energy' correction. Following that, Antoncik (in 1955) [20] had included the second-order modification of the potential due to atomic motion, giving a 'Debye-Waller' correction'. It was believed that those two terms were 'in some sense equivalent', so only one or the other should be used. AHC theory developed a second-order theory drawing the missing link between the two terms and showing that they were not equivalent

and that both should be used.

In the adiabatic case, the change of energy level in a band n for a k wavevector of an electron due to ion motion in the i direction of the α atom, $\frac{\partial \epsilon_{n,\mathbf{k}}}{\partial r_{\alpha,i}}$ can be derived from simple relations such as :

- $\langle \phi_{n,\mathbf{k}} | \phi_{n,\mathbf{k}} \rangle = 1$, meaning the wavefunction is normalized
- $\epsilon_{n,\mathbf{k}} = \langle \phi_{n,\mathbf{k}} | H | \phi_{n,\mathbf{k}} \rangle$, from the Schödinger equation, multiplied by $\langle \phi_{n,\mathbf{k}} |$.

The energy change with respect to such atomic displacement can be written :

$$\frac{\partial \epsilon_{n,\mathbf{k}}}{\partial r_{\alpha,i}} = \left\langle \frac{\partial \phi_{n,\mathbf{k}}}{\partial r_{\alpha,i}} \right| H \left| \phi_{n,\mathbf{k}} \right\rangle + \langle \phi_{n,\mathbf{k}} | H \left| \frac{\partial \phi_{n,\mathbf{k}}}{\partial r_{\alpha,i}} \right\rangle + \langle \phi_{n,\mathbf{k}} | \frac{\partial H}{\partial r_{\alpha,i}} | \phi_{n,\mathbf{k}} \rangle , \tag{20}$$

$$\frac{\partial \epsilon_{n,\mathbf{k}}}{\partial r_{\alpha,i}} = \epsilon_{n,\mathbf{k}} \left\langle \frac{\partial \phi_{n,\mathbf{k}}}{\partial r_{\alpha,i}} \right| \left. \phi_{n,\mathbf{k}} \right\rangle + \epsilon_{n,\mathbf{k}} \left\langle \phi_{n,\mathbf{k}} \right| \left. \frac{\partial \phi_{n,\mathbf{k}}}{\partial r_{\alpha,i}} \right\rangle + \langle \phi_{n,\mathbf{k}} | \frac{\partial H}{\partial r_{\alpha,i}} | \phi_{n,\mathbf{k}} \rangle , \tag{21}$$

$$\frac{\partial \epsilon_{n,\mathbf{k}}}{\partial r_{\alpha,i}} = \epsilon_{n,\mathbf{k}} \frac{\partial \langle \phi_{n,\mathbf{k}} | \phi_{n,\mathbf{k}} \rangle}{\partial r_{\alpha,i}} + \langle \phi_{n,\mathbf{k}} | \frac{\partial H}{\partial r_{\alpha,i}} | \phi_{n,\mathbf{k}} \rangle , \tag{22}$$

$$\frac{\partial \epsilon_{n,\mathbf{k}}}{\partial r_{\alpha,i}} = \langle \phi_{n,\mathbf{k}} | \frac{\partial H}{\partial r_{\alpha,i}} | \phi_{n,\mathbf{k}} \rangle . \tag{23}$$

This result is known as the Hellmann-Feynman theorem [21], stating that in order to compute the derivative of the energy with respect to a chosen parameter, one does not need the derivative of the wavefunctions with respect to this parameter. This is a rather good news, since it is computationally less demanding to derive the Hamiltonian for a perturbation than to compute the derivative of each wavefunction for each perturbation.

Similarly, to get the second derivative of the energy levels one can use the same principle than previously with the first order perturbation theory to obtain :

$$\frac{\partial \epsilon^2_{n,\mathbf{k}}}{\partial r_{\alpha,i} \partial r_{\beta,j}} = \frac{\partial}{\partial r_{\beta,j}} \left(\langle \phi_{n,\mathbf{k}} | \frac{\partial H}{\partial r_{\alpha,i}} | \phi_{n,\mathbf{k}} \rangle \right) , \tag{24}$$

$$\frac{\partial \epsilon^2_{n,\mathbf{k}}}{\partial r_{\alpha,i} \partial r_{\beta,j}} = \langle \phi_{n,\mathbf{k}} | \frac{\partial^2 H}{\partial r_{\alpha,i} \partial r_{\beta,j}} | \phi_{n,\mathbf{k}} \rangle + \left\langle \frac{\partial \phi_{n,\mathbf{k}}}{\partial r_{\beta,j}} \right| \frac{\partial H}{\partial r_{\alpha,i}} | \phi_{n,\mathbf{k}} \rangle + \langle \phi_{n,\mathbf{k}} | \frac{\partial H}{\partial r_{\alpha,i}} \left| \frac{\partial \phi_{n,\mathbf{k}}}{\partial r_{\beta,j}} \right\rangle . \tag{25}$$

Using first-order perturbation theory for the derivative of $|\phi_{n,\mathbf{k}}\rangle$:

$$\left| \frac{\partial \phi_{n,\mathbf{k}}}{\partial r_{\beta,j}} \right\rangle = \sum_{m \neq n} \frac{|\phi_{m,\mathbf{k}}\rangle \langle \phi_{m,\mathbf{k}}| \frac{\partial H}{\partial r_{\beta,j}} |\phi_{n,\mathbf{k}}\rangle}{\epsilon_{m,\mathbf{k}} - \epsilon_{n,\mathbf{k}}}. \tag{26}$$

If one substitutes this expression in equation 24, the final second derivative of the energy with respect to atomic displacement is :

$$\frac{\partial \epsilon^2_{n,\mathbf{k}}}{\partial r_{\alpha,i} \partial r_{\beta,j}} = \langle \phi_{n,\mathbf{k}} | \frac{\partial^2 H}{\partial r_{\alpha,i} \partial r_{\beta,j}} | \phi_{n,\mathbf{k}} \rangle + 2 \sum_{m \neq n} \frac{\langle \phi_{m,\mathbf{k}}| \frac{\partial H}{\partial r_{\alpha,i}} |\phi_{n,\mathbf{k}}\rangle \langle \phi_{n,\mathbf{k}}| \frac{\partial H}{\partial r_{\beta,j}} |\phi_{m,\mathbf{k}}\rangle}{\epsilon_{m,\mathbf{k}} - \epsilon_{n,\mathbf{k}}}. \tag{27}$$

The first term is the static Debye-Waller term, requiring the second derivative of the Hamiltonian with respect to both nuclear displacements. It describes how the electronic energy changes due to the average displacement of atoms (even in the absence of phonon excitations). The second term is the Fan-Migdal term with $\langle \phi_{m,\mathbf{k}}|$, an other electronic eigenstate. Since it involves a dependency on phonon frequencies (in the non-adiabatic approach anyway) and occupation numbers, it is a dynamical process and it includes both real and virtual phonon processes.

In equations (24) to (27), the adiabatic AHC theory is used. This means that the phonon energy does not contribute to the total energy of the material. Within this approximation, the phonon frequencies can be neglected with respect to electronic excitations. This is why in equation (27), the denominator of the Fan-Migdal term has no phonon frequency dependence, only

electronic eigenvalues are taken into account. Comparison of the renormalization energy due to EPI from different approaches (directly from atomic position fluctuations, from Janak's theorem generalized to the case where the Helmholtz free energy is used as well as from the AHC, relying on the ion-rigid approximation) has been done by S. Poncé et al. [22]. However, such a mathematical formalism is outside the range of this present work.

In the non-adiabatic approach, the electron-phonon self-energy $\sum^{e-ph}$ can be written as :

$$\sum^{e-ph}(\omega, T) = \sum^{FM}(\omega, T) + \sum^{DW}(T). \tag{28}$$

This relation can be represented by way of so-called "Feynman diagrams", on Figure 7.

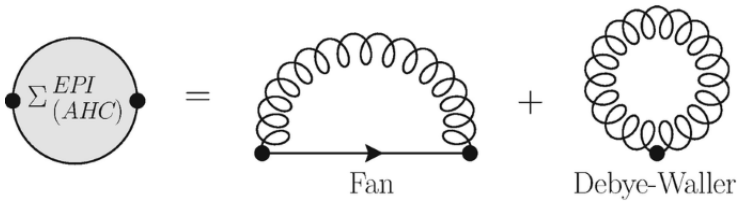

Figure 7: Feynman diagram of electron phonon interaction via the Fan and Debye-Waller self energy contribution (the straight lines are interacting electrons and the curvy lines are the phonon propagators), from ref. [23].

The implementation of those equations into ABINIT will be discussed in section 2.5

2.5 Quasi-particle and Zero Point Renormalization

As previously mentioned, the electron-phonon self energy $\sum^{e-ph}$ has two distinct contributions : the dynamic frequency-dependent Fan-Migdal (FM) self-energy and the static Debye-Waller (DW) terms (illustrated in figure 7).

Within the ABINIT implementation, this means the electron-phonon coupling will be described by DFT using perturbation theory to access the second order in the atomic displacement. Density Functional Perturbation Theory (DFPT) is a well documented method to obtain physical properties linked to the atomic motion of ions in the crystal in response to a stimulus such as magnetic or electric field [24] [25]. Some properties computed within this formalism are phonon band structure, dielectric constant, several thermodynamic properties (specific heat, entropy, ...). In this section, the only property of interest will be the electron-phonon self-energy.

The full derivation of the Fan-Migdal and Debye-Waller terms is quite complex and only the final equations are shown and commented here. The electron-phonon coupling matrix is defined by $g^{\nu}_{mn}(\mathbf{k}, \mathbf{q})$ (showing the scattering effect going from the state $n\mathbf{k}$ to the state $m\mathbf{k}+\mathbf{q}$ via the phonon of branch ν and wavevector $\mathbf{q}$) [26]:

$$g^{\nu}_{mn}(\mathbf{k}, \mathbf{q}) = \frac{1}{\sqrt{2\omega_{\mathbf{q}\nu}}} \langle \psi_{m\mathbf{k}+\mathbf{q}} | \, \Delta_{\mathbf{q}\nu} V \, | \psi_{n\mathbf{k}} \rangle \,, \tag{29}$$

where the indices $\mathbf{k}+\mathbf{q}$ and $\mathbf{k}$ of the wavefunctions illustrate the emission of a virtual phonon and $\Delta_{\mathbf{q}\nu}V$, the perturbation potential, is the first order derivative of the KS potential (from phonon displacement). Having defined the electron-phonon matrix, the FM self energy in the KS basis set can be written :

$$\sum\nolimits^{FM}_{n\mathbf{k}}(\omega, T) = \sum_{m,\nu} \int_{BZ} \frac{d\mathbf{q}}{\Omega_{BZ}} |g^{\nu}_{mn}(\mathbf{k}, \mathbf{q})|^2 \times \left[\frac{n_{\mathbf{q}\nu}(T) + f_{m\mathbf{k}+\mathbf{q}}(T)}{\omega - \epsilon_{m\mathbf{k}+\mathbf{q}} + \omega_{\mathbf{q}\nu} + i\eta} + \frac{n_{\mathbf{q}\nu}(T) + 1 - f_{m\mathbf{k}+\mathbf{q}}(T)}{\omega - \epsilon_{m\mathbf{k}+\mathbf{q}} - \omega_{\mathbf{q}\nu} + i\eta} \right]. \tag{30}$$

This equation is a sum over the m, ν states of an integral over the whole Brillouin Zone (BZ) of $|g^{\nu}_{mn}(\mathbf{k}, \mathbf{q})|^2 = g^{\nu\star}_{mn}(\mathbf{k}, \mathbf{q}) g^{\nu}_{mn}(\mathbf{k}, \mathbf{q})$ times a factor (depending on the electron and phonon occupation numbers and energies; and the frequency ω). $f_{m\mathbf{k}+\mathbf{q}}(T)$ is the Fermi-Dirac distribution and

$n_{\mathbf{q}\nu}(T)$ is the Bose-Einstein distribution. Let us note that the summation over all the phonon modes are normalized by the $1/\sqrt{2\omega_{\mathbf{q}\nu}}$ factor in equation (29). The η parameter is a small infinitesimal, positive, real. In practice, for numerical reasons, it has a non-zero value and this affects the final result. Its influence on the final ZPR value will have to be studied.

As previously explained, within the adiabatic approximation, the phonon frequency at the denominator of the FM term ($\pm\omega_{\mathbf{q}\nu}$) is ignored. Equation (30) can be re-written as :

$$\sum\nolimits_{n\mathbf{k}}^{FM}(\epsilon_{n\mathbf{k}},T)=\sum_{m,\nu}\int_{BZ}\frac{d\mathbf{q}}{\Omega_{BZ}}|g^{\nu}_{mn}(\mathbf{k},\mathbf{q})|^2\times\left[\frac{2n_{\mathbf{q}\nu}(T)+1}{\epsilon_{n\mathbf{k}}-\epsilon_{m\mathbf{k}+\mathbf{q}}+i\eta}\right]. \tag{31}$$

The Debye-Waller, frequency independent, term can be similarly expressed :

$$\sum\nolimits_{n\mathbf{q}}^{DW}(T)=\sum_{\mathbf{q}\nu m}(2n_{\mathbf{q}\nu}(T)+1)\frac{g^{2,DW}_{mn\nu}(\mathbf{k},\mathbf{q})}{\epsilon_{n\mathbf{k}}-\epsilon_{m\mathbf{k}}}, \tag{32}$$

where the Debye-Waller matrix element $g^{2,DW}_{mn\nu}(\mathbf{k},\mathbf{q})$ is found within the ion-rigid approximation (stating that when one ion is moved from its equilibrium position, the whole potential also shifts position but stays rigid). This term can be expressed in term of first order simple $g^{\nu}_{mn}(\mathbf{k},\mathbf{q})$ matrix elements within the rigid-ion approximation.

Knowing the electron-phonon self-energy $\sum^{e-ph}$, to find the Quasi-Particle energies, one can use two different methods (both implemented within ABINIT) : the "on-the-mass-shell" (OTMS) approximation or the the linearized QP equation. Both are corrections of the Kohn-Sham energy level. The OTMS approach estimates the QP energy to be given by the simple real part of the self energy :

$$\epsilon^{QP}_{n\mathbf{k}}=\epsilon^{KS}_{n\mathbf{k}}+\mathfrak{R}\sum\nolimits^{e-ph}(\epsilon_{n\mathbf{k}}). \tag{33}$$

Whereas for the linearized QP equation, a multiplication factor $Z_{n\mathbf{k}}$ is introduced :

$$\epsilon^{QP}_{n\mathbf{k}}=\epsilon^{KS}_{n\mathbf{k}}+Z_{n\mathbf{k}}\mathfrak{R}\sum\nolimits^{e-ph}(\epsilon_{n\mathbf{k}}), \tag{34}$$

with $Z_{n\mathbf{k}}$ the renormalization factor :

$$Z_{n\mathbf{k}}=\left(1-\mathfrak{R}\left[\frac{\partial\sum^{e-ph}_{n\mathbf{k}}}{\partial\epsilon}\bigg|_{\epsilon=\epsilon_{n\mathbf{k}}}\right]\right)^{-1}. \tag{35}$$

Equation (34) illustrates that the quasi-particle energy state and KS state are relatively close. The quasiparticle energy $\epsilon^{QP}_{n\mathbf{k}}$ can be found from the position of the principal peak of the spectral function $A_{n\mathbf{k}}(\omega)$ (with $\omega=\epsilon^{0}_{n\mathbf{k}}$) :

$$A_{n\mathbf{k}}(\omega)=-\frac{1}{\pi}\frac{\left|\mathfrak{Im}\left[\sum^{e-ph}_{n\mathbf{k}}(\omega)\right]\right|}{\left(\omega-\epsilon_{n\mathbf{k}}-\mathfrak{R}\left[\sum^{e-ph}_{n\mathbf{k}}(\omega)\right]\right)^2+\mathfrak{Im}\left[\sum^{e-ph}_{n\mathbf{k}}(\omega)\right]^2}. \tag{36}$$

Figure 8 shows an example of the computed real and imaginary part of $\sum^{e-ph}_{n\mathbf{k}}$ as well as the spectral function $A(\omega)$.

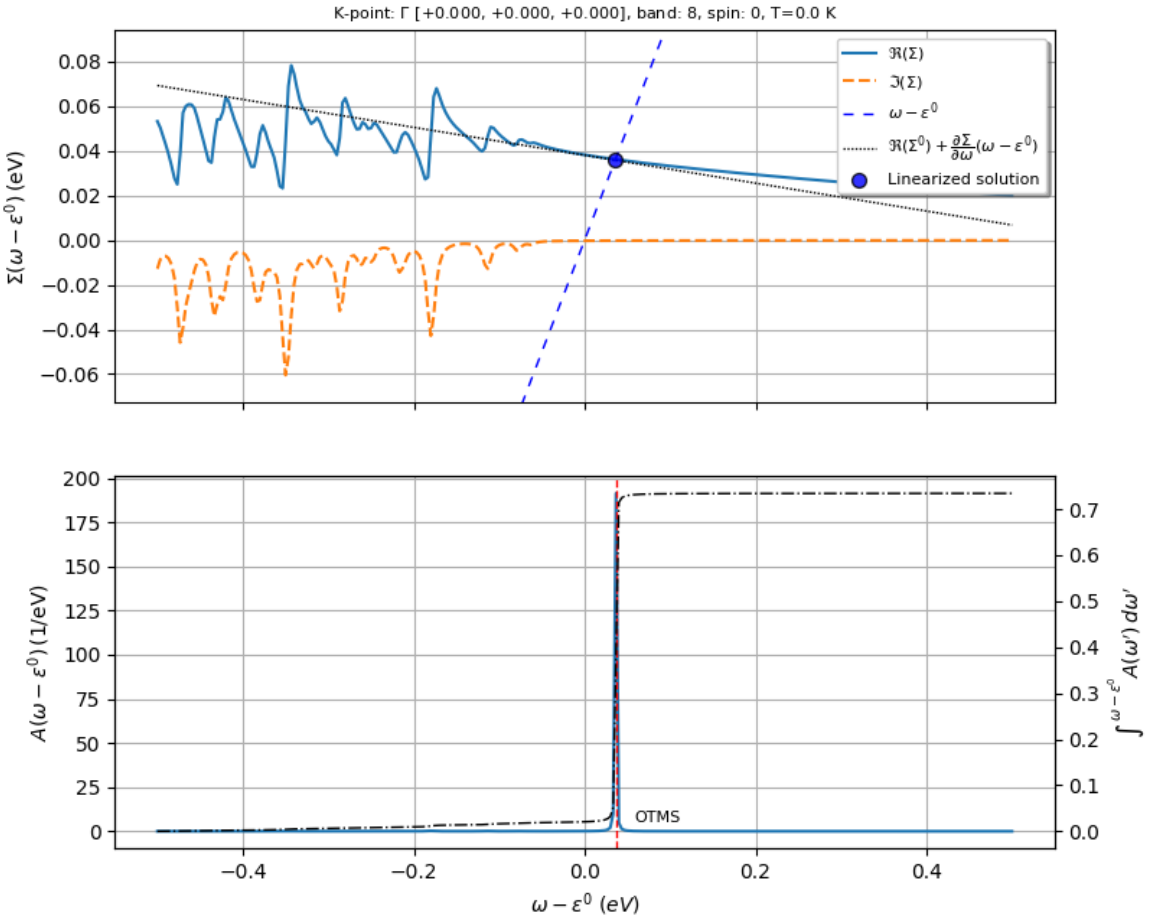

Figure 8: Computed using ABINIT (within this work), (top) InP electron-phonon real and imaginary self-energy part for the maximum of the valence band at the Γ point [0,0,0]. The intersection of the grey dashed line (which approximates the eigenvalue for the self energy real part at $x = y$, the blue dashed line) with the solid blue line $Re\left[\sum\right]$ is the graphical solution of the linearized QP equation. (Bottom) Spectral function $A(\omega)$(solid line) and its integral (dashed line). The position of the sharp peak gives the QP energy correction for this band at the Γ point.

In the context of this work, both methods (OTMS and the linearized QP equation) will be used and their respective results, compared. However, it appears that the on-the-mass-shell provides slightly better results. According to recent studies, the spectral function $A(\omega)$ makes some errors in the weight and energy of the QP peak [27]. A better approach to the self-energy, named the "cumulant" approach, not presented in this work, actually gives electronic eigenenergie shifts in agreement with the OTMS approach [27].

2.6 Thermal Lattice Expansion : a simple view

The second correction to the band gap value is due to the lattice thermal expansion (even at 0K). The lattice parameters change under the influence of temperature and this change leads to a modification of the band gap value :

$$\frac{\partial E_g}{\partial T} = \frac{\partial E_g}{\partial a}\frac{\partial a}{\partial T}. \tag{37}$$

So in order to characterize the change of E_g with respect to temperature, one first needs the change of lattice parameter with respect to temperature, $\frac{\partial a}{\partial T}$.

When a material is heated, the atoms start to oscillate around their equilibrium position due to thermal energy. Those oscillation will shift their equilibrium positions in the crystal depending on the shape of the potential energy of the lattice. For a perfect harmonic potential (with only quadratic terms), the average displacement is zero, $< u >= 0$. However, for an anharmonic potential, the most common case, the average displacement is not null, $< u > \neq 0$, as shown in Figure 9

The anharmonic potential thus leads to a change in the ionic position of the atoms. To quantify how much energy is transferred to the lattice vibration as a function of the temperature, one can use the Bose-Einstein distribution. The Bose-Einstein distribution gives the number of phonon (i.e lattice vibration) in a specific energy state i:

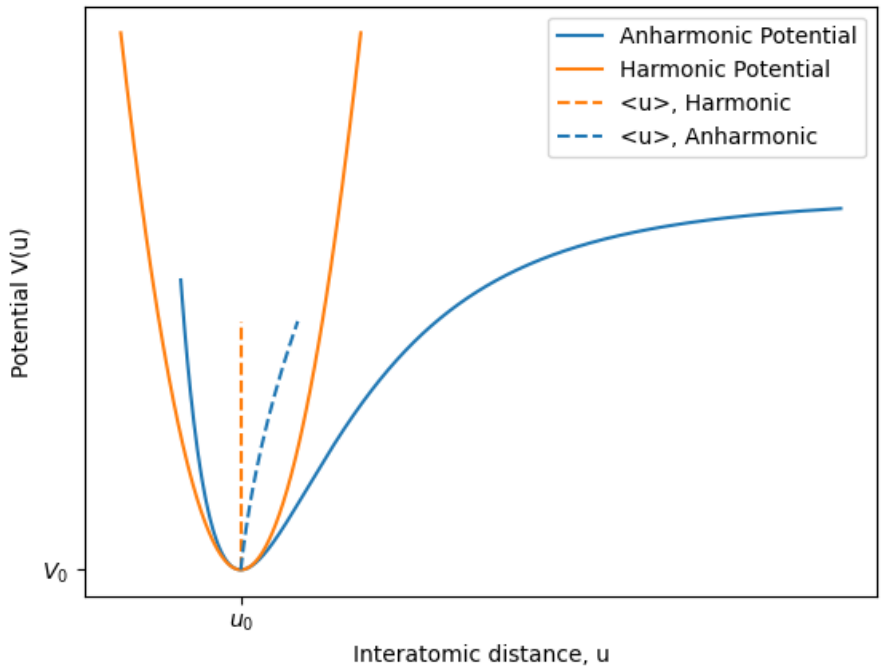

Figure 9: Harmonic and anharmonic potential with their average displacement (neglecting the lattice expansion at T = 0 K).

$$n_i = \frac{g_i}{e^{(\epsilon_i - \mu)/k_B T} - 1}, \qquad (38)$$

where g_i is the degeneracy of the energy level i, μ is the chemical potential ($\mu = 0$, since the number of phonons is not imposed) and k_B is the Boltzmann's constant (in eV/K). The energy ϵ_i of a mode with an angular frequency ω_i is :

$$\epsilon_i = \hbar\omega_i, \qquad (39)$$

with $\hbar$ the Planck's constant.

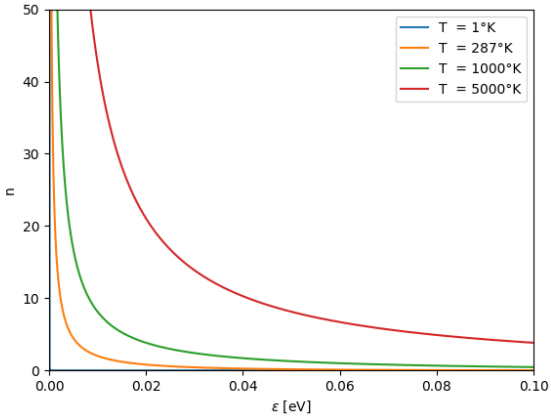

Figure 10: Bose-Einstein distribution for T = 1, 287, 1000, 5000 K and $\mu = 0$.

Thus, at a higher temperature, the higher energy phonon modes are increasingly more populated. Since the total vibrational energy of the lattice is a function of the phonon population, it explains the shift of the equilibrium position of the ions atomic position. The lattice parameter $a(T)$ is then influenced by the phonon total energy, which is written :

$$E_{phonon} = \int g(\omega)\hbar\omega \left(n(\omega) + \frac{1}{2} \right) d\omega, \qquad (40)$$

with $g(\omega)$, the phonon density of state. This equation explains why, even at T=0 K, the contribution of the phonon energy to the total energy is never null. When $T \to 0$, $n(\omega) \to 0$ but the 1/2 factor prevents the phonon energy contribution E_{phonon} from going to zero. This is called the Zero Point Lattice Expansion (ZPLE).

2.7 Quasi Harmonic Approximation and Zero-Point Lattice Expansion

In chapter 2.3, the harmonic model has been introduced, with a simplified - yet correct - view of a phonon. Such a model is useful for the derivation of many important solid properties but does not include the effect mentioned in Sec. 2.6. A more complete theory is the quasi harmonic approximation, presented in this section from a thermodynamic point of view.

The quasi harmonic approximation (QHA) is a widely used method to evaluate volume dependent thermal effects such as temperature dependence of the lattice parameters or, consequently, the thermal expansion coefficient of a material, α_V. Other thermodynamic quantities of interest can also be found within this theory, like the heat capacity C_v and the Grüneisen parameter γ. In the present work, QHA is used to find the volume equilibrium by minimizing the Gibbs free energy for different pressure and different temperature curves.

The main hypothesis of the QHA is that the phonon modes are harmonic, independent from one another, but depend on the ions atomic positions and lattice constants which are adjustable parameters (in contrast with the simple harmonic model). This theory derives from the harmonic phonon model of the lattice behavior, with the addition that phonon frequencies become volume-dependent (to explain the thermal expansion phenomena).

For a given material lattice, the quasi-harmonic approximation allows the Helmholtz free energy F to be written [4]:

$$F(T, V) = E_{lat}(V) + U_{vib}(T, V) - TS_{vib}(T, V), \qquad (41)$$

with E_{lat}, the internal lattice energy (also called the Born-Oppenheimer internal energy), U_{vib} the energy linked to the vibration of the lattice and T, V, S_{vib} respectively the temperature, volume

and entropy (due to the vibrational degree of freedom). The Born-Oppenheimer energy at zero-temperature is solely due to the internal static energy of the covalent links between ions (not affected by temperature, nor by lattice vibration). To empathize this, the relation can then be re-written :

$$F(T,V) = E_{BO}(V) + F_{vib}(T,V). \tag{42}$$

Using a bit of thermodynamic and the definition of enthalpy, the relation between Helmholtz (F) and Gibbs free energy(G) of a system is found to be :

$$G(V,P,T) = F(T,V) + PV, \tag{43}$$

$$G(V,P,T) = E_{lat}(V) + U_{vib}(T,V) - TS_{vib}(T,V) + PV. \tag{44}$$

The equilibrium volume as a function of pressure and temperature is the minimum of $G(V,P,T)$.

Within ABINIT, most of those quantities are easily computed thanks to the usual Bose-Einstein distribution function $n_{\mathbf{q},\nu}(V,T)$ for each phonon mode $\mathbf{q},\nu$. The volume dependence of n comes from the main approximation of the QHA, which is that phonon frequency is volume-dependent. The same way, the phonon frequency $\omega_{\mathbf{q},\nu}$ becomes $\omega_{\mathbf{q},\nu}(V)$. The vibrational internal energy, free energy and entropy per unit cell are expressed as [4]:

$$U_{vib}(T,V) = \frac{1}{\Omega_{BZ}} \int_{BZ} \sum_{\nu} \left(\frac{1}{2} + \bar{n}_{\mathbf{q},\nu}(V,T) \right) \hbar\omega_{\mathbf{q},\nu}(V) d\mathbf{q}, \tag{45}$$

$$F_{vib}(T,V) = \frac{1}{\Omega_{BZ}} \int_{BZ} \sum_{\nu} \left(\frac{\hbar\omega_{\mathbf{q},\nu}(V)}{2} + k_B T \ln\left(1 - e^{\hbar\omega_{\mathbf{q},\nu}(V)/k_B T}\right) \right) d\mathbf{q}, \tag{46}$$

$$S_{vib}(V,T) = \frac{k_B}{\Omega_{BZ}} \int_{BZ} \sum_{\nu} \left(-\ln\left(1 - e^{\hbar\omega_{\mathbf{q},\nu}(V)/k_B T}\right) + \bar{n}_{\mathbf{q},\nu}(V,T) \frac{\hbar\omega_{\mathbf{q},\nu}(V)}{k_B T} \right) d\mathbf{q}. \tag{47}$$

Let us note that all those quantities are normalized by the Brillouin volume cell Ω_{BZ} and the relation $F_{vib} = U_{vib} - TS_{vib}$ is verified.

Knowing those thermodynamic functions, one can derive other properties of interest (in this work, the focus is put on the thermal expansion coefficient α_V):

$$\alpha_V = \frac{1}{V} \left. \frac{\partial V}{\partial T} \right|_T = \frac{1}{V} \left(\left. \frac{\partial^2 F}{\partial V^2} \right|_{V,T} \right)^{-1} \left. \frac{\partial S_{vib}}{\partial V} \right|_{V,T}. \tag{48}$$

Plotting the Gibbs free energy curves for each temperature, one can extrapolate the parabolic relation from the computed points to find for which volume the Gibbs free energy is minimized for each temperature. This volume varies depending on the simulated temperature. This method allows the computation of the volume change with respect to temperature (even at T=0 K). Using finite difference method, one can find the derivative of this curve to get the thermal expansion coefficient $\alpha_v(T)$. This is done with a large enough dV to reduce noise (coming from the numerical derivation) to produce a smooth curve.

3 Materials of interest

This section will present the materials studied in this work. Each type of compound material will be reviewed from literature along with some of their most promising applications in the optoelectronic design. Both electric and optical properties will be reported in order to understand if indeed, those materials have a future in the light-matter interaction technologies.

This present work is following a recent study done by Dr. V. Brousseau-Couture and coworkers, "Zero-point lattice expansion and band gap renormalization: Grüneisen approach versus free energy minimization" in which the zero point renormalization and lattice expansion are evaluated for 22 of the most popular semiconductors (using a similar computational approach than this work). This study presented computation on many popular semiconductors (for both cubic and wurtzite crystal structures) such as AlAs, GaAs, MgO, etc [28]. However, some crucial semiconductors in the microelectronic world were not assessed nor considered in this study. The present work aims to fill this gap by focusing on semiconductors that were overlooked in the prior study. By expanding the scope of materials assessed, this research seeks to provide a more comprehensive understanding of the properties of these essential materials and their potential impact on future optoelectronic technologies.

The 10 materials investigated here are semiconductors with a band gap $0 > E_g < 3$eV. They can be separated on the basis of their composition in five categories : the III-V semiconductors (InAs, InP, BP), the IV-VI semiconductors (PbS, PbSe, PbTe), the layered materials (InSe, GaSe), the SiGe alloy and finally the special case of $BaTiO_3$.

3.1 III-V Semiconductors

In the III-V semiconductor group (that is, formed from an atom of the third column in the Mendeleev Table and an atom from the fifth column), three materials are investigated : InAs, InP and BP. All three exhibit a face-centered cubic, zincblende crystal structure. The III-V semiconductor group is one of the most interesting coupling possible with regards to optoelectronic applications. Most of them exhibit a very high carrier mobility needed for high-frequency and high-power application such as microwave amplifiers. In addition, InP and InAs are both direct band gap semiconductors, meaning that radiative recombination process is quite fast and ideal for the emission of a photon. Applications like diodes, LEDs, lasers and UV light emission often use III-V semiconductors (GaAs, InAs, etc) [29]. Table 1 gathers important electric and optical properties for the InAs, InP and BP (bulk) semiconductors.

III-V	E_g [eV]	$\mu(\frac{cm^2}{V.s})$
InAs	0.35	40000 (electrons)
InP	1.34	5400 (electrons)
BP	2.02	900 (holes)

Table 1: Band gap and carrier mobility for InAs, InP (taken from Ref [30]) and BP, for a doping level of $10^{-18}cm^{-3}$ (taken from Ref [31, 32])

Whereas InAs and InP are mostly used as optical active components due to their direct band gap, BP is a very promising candidate for a transparent conductive film (of p-type). Such a film is used as an electrode in solar cells and needs both a low absorption in the visible light range and a high mobility. BP shows very high conductivity as well but its transparency is affected by its high band bap, with respect to such transparency requirement (decreasing its efficiency).[31]

While it is true that InP receives a lot of attention as a potential optical component in future electronics, its true value resides in the world of radiofrequency (RF) transistor substrate. Since the invention of the first transistors in the 50's, colossal efforts has been made for the sole purpose to make them smaller. As they get smaller and smaller, new problems start to emerge in fabrication,

design, embedding, etc. One of those problems is the parasitic noise level at high frequency. To approach this issue, better and better substrates and transistor implementation have been found throughout the last decades. The leading transistor in the industry was developed on silicon, then GaAs, for its remarkable transport properties and band gap engineering possibilities, then more recently, InP, for its high cut-off frequency (see Figure 11) and its low noise level (see Figure 12). The cut-off frequency of a electronic device is the maximal frequency at which the energy flowing through the system is maximal. Beyond that limit, the energy strongly decreases, along with the performances of the device.

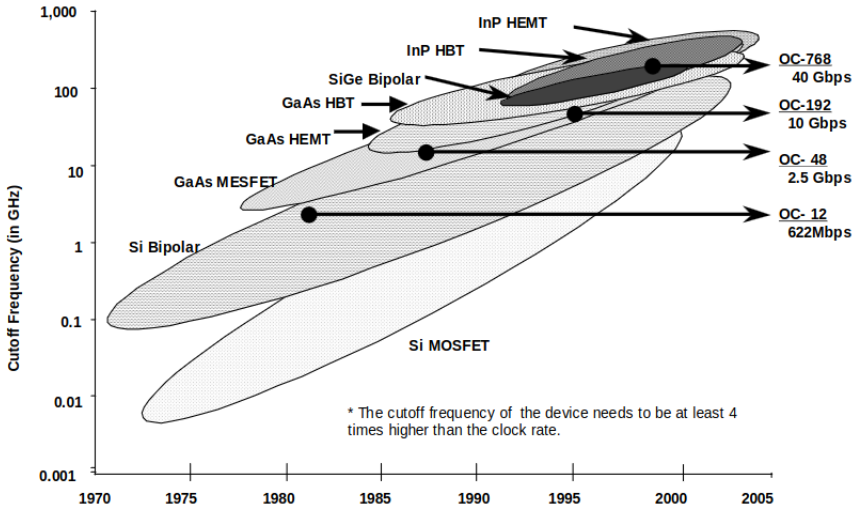

Figure 11: Semiconductor technology roadmap for lightwave electronics, from ref. [33].

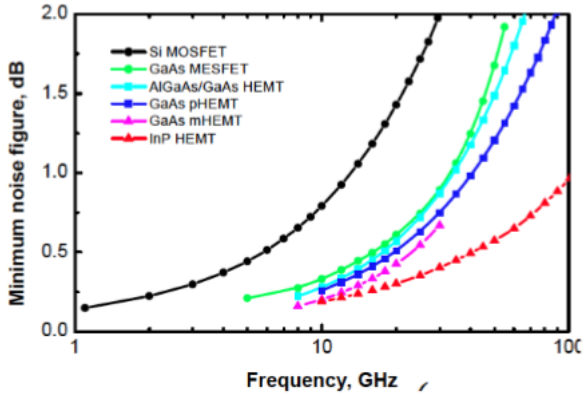

Figure 12: Noise level for most popular substrates in transistor-like applications as a function of the frequency, from ref. [34].

To summarize, InAs as an active light component (LED, Lasers, etc), BP as a transparent p-type conductive film or InP for high power RF transistors (used in aeronautics for airplanes, helicopters, etc) are important semiconductors for optoelectronic technologies.

3.2 IV-VI Semiconductors

In the IV-VI semiconductor group, the main focus is put on the lead chalcogenides elements (that is, PbS, PbSe, PbTe). These materials have a narrow band gap ($E_g < 0.5$ eV) and a quite high

mobility. They show unique structural and electronic properties, making them relevant for many potential applications : thermoelectric, optoelectronic, or spintronic devices [35]. Thanks to their relatively small band gap, one of the most interesting application for the lead chalcogenides is the infrared detection/lasers [36]. The main difference with the more popular III-V semiconductor zinc blende is that the PbX elements (with X = S, Se, Te) are polar salts that crystallize in the rocksalt structure. This leads to specific electronic properties such as a direct band gap at the L symmetry point of the Brillouin zone (explained by the addition of a Pb 6s electron band inside the valence bands, which induces strong repulsion between energy levels, see Figure 13)[37].

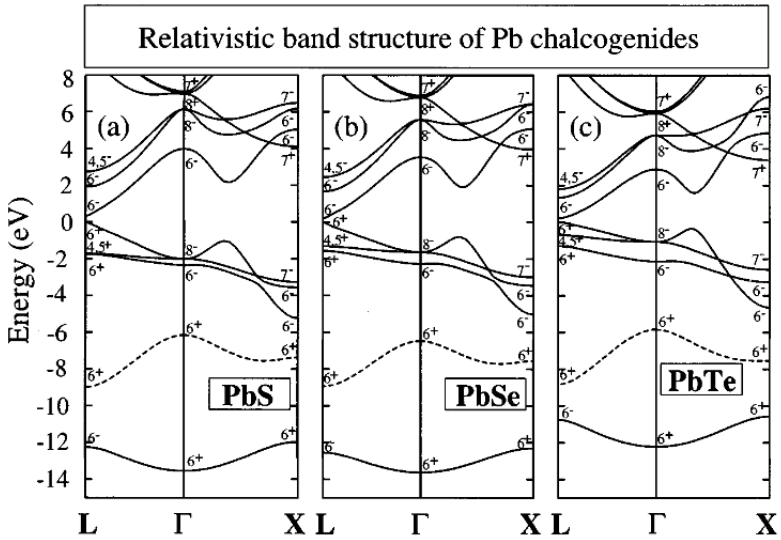

Figure 13: Calculated band structure for PbS, PbSe and PbTe (using the LDA as implemented in the linearized augmented plane-wave method.). The occupied 6s band is represented by the dashed line, from ref. [37].

Lead chalcogenides are suited for photovoltaic devices or IR diode lasers because of their small band gap but also because of their cut-off wavelengths (the smallest wavelength at which a laser can efficiently emit light). These major properties are gathered in Table 2

III-V	E_g [eV]	cut-off wavelength (μm)
PbS	0.42	3.0
PbSe	0.27	4.6
PbTe	0.31	4.0

Table 2: Band gap and cut-off wavelengths for PbS, PbSe and PbTe, from ref. [38].

In addition, these properties can be fine-tuned using an alloy of ternary composition like $Pb_{1-x}Sn_xTe$ or $Pb_{1-x}Sn_xSe$, thus achieving very precise control over the desired light emission wavelength [39].

3.3 Layered Materials

InSe and GaSe belong to the class of layered materials in the III-VI semiconductor group. They are called group III metal chalcogenides and have many interesting potentials applications in the industry. They are formed of hexagonal layers linked with covalent bonding staked together vertically with van der Waals interactions between the layers [40]. Those van der Waals bonds are much weaker than the ionic-covalent bonds, leading to highly anisotropic optical, mechanical and electronic properties [41]. Reducing the dimensions of a materials typically enable the tunability of

the band gap (see Figure 14) as well as its mechanical strength. This is why layered materials are usually considered when designing flexible electronic devices but also for sensor devices, electromechanical systems (MEMS), solar cells and, lastly, photodetectors [42]. In the 2D materials world, the III-VI group (and especially InSe) draws a lot of attention. Indeed, InSe possesses saturated bonds (without dangling electrons), which enforce a very high mobility.

Depending on the staking of the hexagonal layers, there are three distinct phases of the structural lattice : β, ϵ, γ (experimentally determined by a X-ray diffraction pattern).

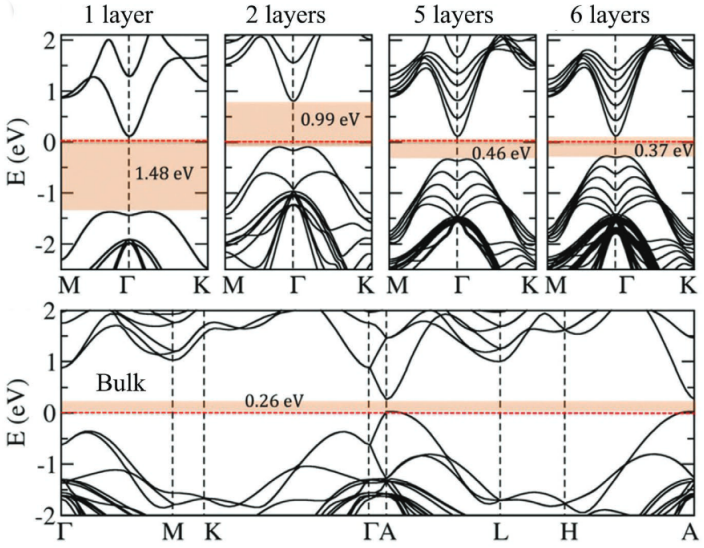

Figure 14: Computed (from DFT) electronic structure for the γ-InSe depending on the number of layers, with the corresponding band gap in red, taken from ref. [43].

Their experimental bulk band gaps and carrier mobility are gather in Table 3.

III-V	E_g [eV]	$\mu(\frac{cm^2}{V.s})$
InSe	1.25	1055
GaSe	2.13	-

Table 3: Band gap for InSe, GaSe and InSe carrier mobility, from ref. [44].

While monolayer materials have outstanding properties, this work will only compute the band gap renormalization for the bulk InSe and GaSe (with a hexagonal lattice).

3.4 SiGe Alloy

SiGe (which, formally should be written Si_xGe_{1-x}) is an alloy formed of two IV semiconductor elements. Its optical properties are the subject of numerous studies throughout the years as the amorphous silicon-germanium is quite promising in the photovoltaic, photo-detector and microelectronic domain [45]. High speed, low power electronic applications such as IR diode, high performance bipolar transistor and integrated circuits are getting better and faster each year, and the development of appropriated, specific materials is one of the key behind this rapidly growing industry. SiGe is interesting with respect to several of its properties.

First of all, due to its alloy nature, the Si_xGe_{1-x} band gap is highly tunable. By adjusting the concentration of silicon respective to the concentration of germanium, the direct band gap can vary between $E_g = 1.12$ eV (for $x = 1$, bulk silicon) and $E_g = 0.66$ eV (for $x = 0$, bulk germanium). This relation is shown on Figure 15a.

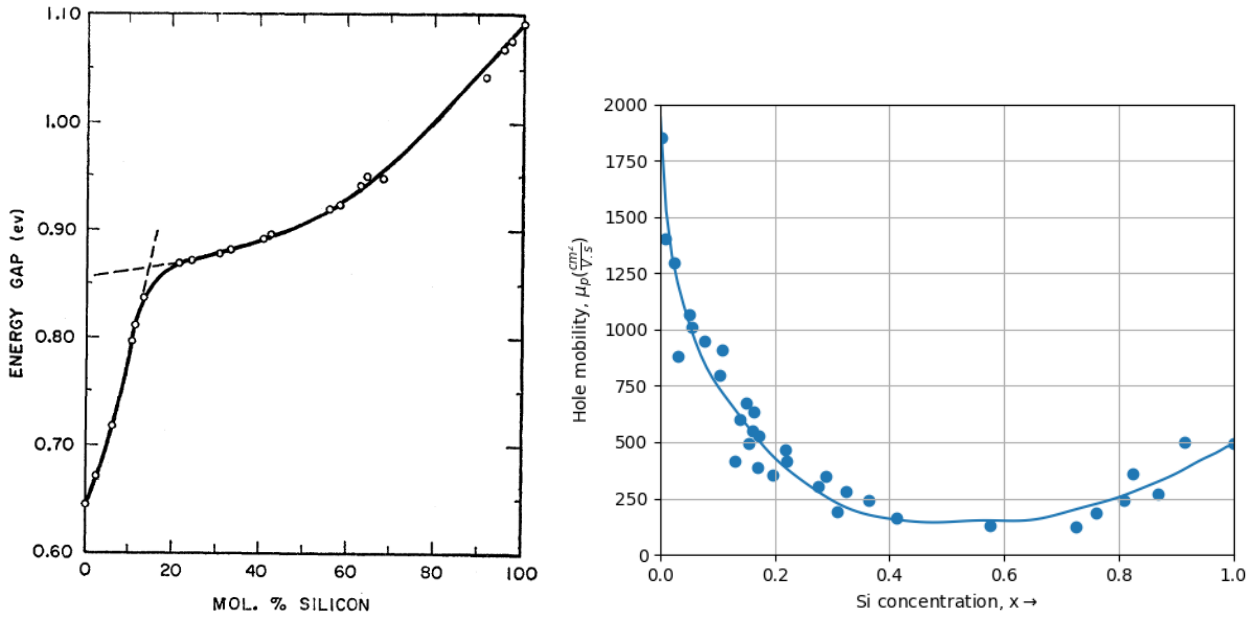

(a) (b)

Figure 15: (a) Composition dependence of the experimental Si_xGe_{1-x} direct band gap (at Γ). The behavior change at $15\%Si$ is due to a change from a Ge-like ([111]) to a Si-like ([100]) conduction band minimum, from ref. [46]. (b) Hole mobility as a function of the % Si concentration, from ref. [47].

Lowering the band gap from the silicon value makes the SiGe more suitable for high speed low power devices.

In addition, fabrication processes are facilitated by the fact that SiGe is compatible with silicon manufacturing. It can be easily integrated in a standard Si-wafer for analog and digital circuits on the same die. Such an approach reduces the $1/f$ noise (also called the pink noise, which power spectral density depends on the frequency) as well as the leakage current by the base [48]. While this is a complicated subject on which a lot can be said, the main problem with growing SiGe on Si-wafer is the lattice mismatch (which increases from 0% to 4.2% going from $x = 0$ to $x = 1$). Along with those considerations, the hole mobility in a SiGe-based heterojunction bipolar transistor can also by fine-tuned, as shown on Figure 15b. While the hole mobility is higher for pure germanium (by a factor 5), it also increases the interfaces traps density when growing a thermal oxide on SiGe with very low Si concentration. A trade-off must be found [49].

The full characterization of the band gap renormalization for each Si concentration would be very interesting, however for this work, the concentration $Si_{0.5}Ge_{0.5}$ is chosen for the sake of simplicity and computational cost (only 2 atoms per unit cell).

3.5 Barium Titanate ($BaTiO_3$)

The Barium Titanate ($BaTiO_3$) is a very peculiar material, with regards to several aspects. It possesses a perovskite structure, that is, of the form ABX_3, with A and B two cations and X, an anion arranged in a simple cubic lattice, with A and B at the corner and center of the primitive cell. Such materials are attracting a lot of attention for solar cell applications (in fact, the most efficient solar panel to this day use perovskite materials [50]). These structures typically have a high power conversion efficiency (PCE), a critical factor to determine whether or not a given material is a suitable candidate for photovoltaic applications. This high PCE is due to a combination of several favorable factors : high absorption coefficient in the visible light range (not $BaTiO_3$ though), appropriate band gap value and a long diffusion length [51]. In addition to those qualities, the cation

replacement of the A or B site allows a great variability of optical and electrical properties

Among perovskite crystals, $BaTiO_3$ in itself exhibits some remarkable properties among which its ferroelectricity, piezoelectricity, a high band gap (E_g = 3.4 eV [52]) and a high dielectric constant. This makes it a viable option for a wide range of application like energy storage device, ceramic capacitive transducers, infrared detectors, etc [53]. In the optoelectronic world alone, it can acts as a semiconductors transport layer for a multilayer solar cell or as a UV light protection layer (otherwise damaging organic solar cells)[54]. Metal doping can improve the electroptical qualities of the barium titanate oxide (with metals such as Fe, Cu, Zn, Mo, and Ag) [55].

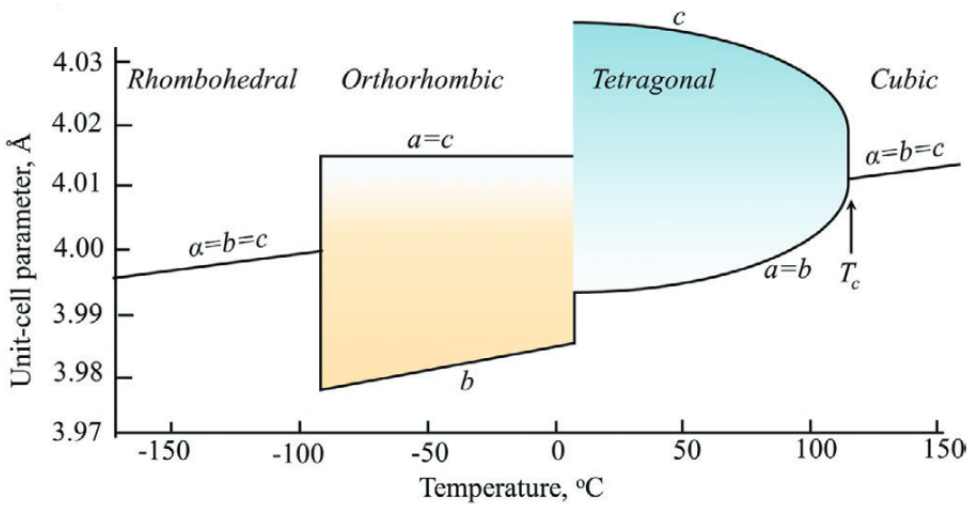

Figure 16: Evolution of the $BaTiO_3$ lattice parameters as a function of temperature, with T_C, the Curie Temperature, from ref. [56].

$BaTiO_3$ is a complex ferroelectric perovskite materials, having 4 different phase transition according to the temperature regime. These transitions occur due to changes in the crystal structure and are the result of the balance between thermal energy and the material internal electrostatic forces. Those transitions are shown in Figure 16. The structure and space group of the $BaTiO_3$ greatly affect the macroscopic properties of the material (even though the order of the lattice parameters changes is about 0.05%). In this work, the rhombohedral phase will be studied, as it is the phase for T = 0 K.

4 Computational details

In this section, all parameters linked to the accuracy of the results are laid out and justified. To ensure the reproducibility of the final calculations and facilitate critical reviews, every choice made, method used, or input variable is documented here. A motivated reader could potentially replicate the work presented in this thesis based on the information in this chapter. The tunable parameters (ensuring reliable and numerically accurate results) in ABINIT are determined through a carefully converged series of tests, referred to as convergence studies.

These convergence studies will be presented for the ground-state properties as well as for the zero-point renormalization (ZPR) from electron-phonon interactions (EPI). Unfortunately, no convergence study was performed for the entire set of materials when computing the Derivative DataBase (DDB files, required for both the ZPR from EPI and the zero-point lattice expansion, ZPLE), due to time constraints. Indeed, DFPT calculations are computationally intensive, and repeating these calculations while varying parameters would not have been feasible within the timeframe of this work. However, when tuning simulation parameters to obtain the DDB files, the values used were ground-state converged, with a post-result convergence check to ensure they provided accurate results. In most cases, these calculations required stricter convergence criteria than simple ground-state calculations.

This chapter gathers informations about the general set-up for which all simulations have been performed. Following the convergence studies, the typical workflows implemented within Abipy and ABINIT for calculating the ZPR from EPI and ZPLE are introduced in Chapter 4.3. The various steps needed are explained to provide the reader a quick overview of the complete chain of calculations for both band gap corrections. Finally, following the workflows, a brief introduction is given to the parallelization capabilities of ABINIT (and Abipy) and how they can significantly accelerate the calculation workflow.

4.1 Generalities

In this work, the main software used is ABINIT v9.10.5 [57]. Its capabilities cover what is needed in order to achieve the goals of this work. Simultaneously, the Abipy package v0.9.1 was used for some useful visualization tools and to automatize the most simple steps of the workflows. Such a work requires an important computational power. The most demanding steps were ran on the Nic5 server (the ULiege/CECI cluster), which possesses a bit less than 5000 CPUs.

Unless stated otherwise, all calculations were performed :

- Without spin-orbit coupling (SOC). Including SOC allows the lifting of the energy levels degeneracy. Indeed, the total angular moment becomes $\hat{J} = \hat{L} + \hat{S}$ with the eigenvalues becoming either $j = l + \frac{1}{2}$ or $j = l + \frac{1}{2}$, splitting each l-orbital into two sublevels. While the energy levels are closer to experimental ones (especially for heavy elements such as lead), the number of electronic bands doubles, increasing quadratically the computation time needed,
- With semi-relativistic norm-conserving pseudopotentials from the Pseudo-Dojo website v0.5 [58]. The pseudopotentials chosen use the GGA-PBEsol functional. Studies were done on the choice of pseudopotentials for ab initio calculations, and it appears that PBEsol pseudopotentials performed better in predicting lattice parameters of ground state compounds [59].
- The starting input structure of the crystals were extracted from the Materials Project website [2].

4.2 Ground state convergence studies

To keep the calculation time to a minimum, but also to trust that the calculation results are precise numerically within an acceptable margin of error, a convergence study is performed on the whole set of materials. The parameters to converge are the total energy of the crystal E_{tot} as well as the

lattice parameters of the structures (which are free to move to minimize the residual intra-forces in the crystal). In this ground state runs, the two varying inputs will be the cut-off energy (which controls the number of planewaves at a given k point) and the number of division of the Brillouin zone (and thus, the number of wavevector in the Brillouin zone - referred to "k points" - in the unit cell). A visual representation of the cut-off energy (referred to as 'ecut') is shown in figure 17.

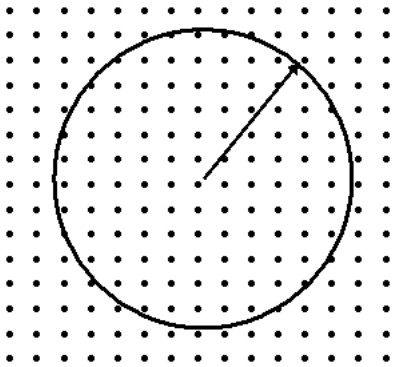

Figure 17: Visual 2D representation of the cut-off energy and the number of planewave coefficients. As the cut-off energy increases, the radius of the circle increases as well, and the number planewave coefficient within the area of the circle increases. The planewaves inside the circle have a lower kinetic energy than ecut ($\frac{1}{2}(2\pi)^2(\vec{k}+\vec{G})^2 < ecut$).Those planewave coefficients allows the correct representation of the unit cell at the interfaces (the more points within the circle, the more it will behave like a 'supercell', without any boundary effects).

The higher the cut-off energy (ecut) and the number of k points (ngkpt) are, the more accurate is the representation of the wavefunction and the sampling of the Brillouin Zone. For a wide-band gap materials, less k points are needed as the energy bands become less parabola-like and flatten. For some insulators, even 1 k point is enough (at the center of the BZ, at the Γ point).

4.2.1 With respect to the total energy

The converging criteria for the total energy is set at ± 0.5 mHa. This is known to provide a good first estimation of the error on the atomization energy and the error on the interatomic distance. Those initial runs were performed using a value of 35 Ha for the ecut and a $4 \times 4 \times 4$ k point grid. Those values should provide decent results (according to common knowledge). The results for all 10 materials are shown in Figure 18 and 19.

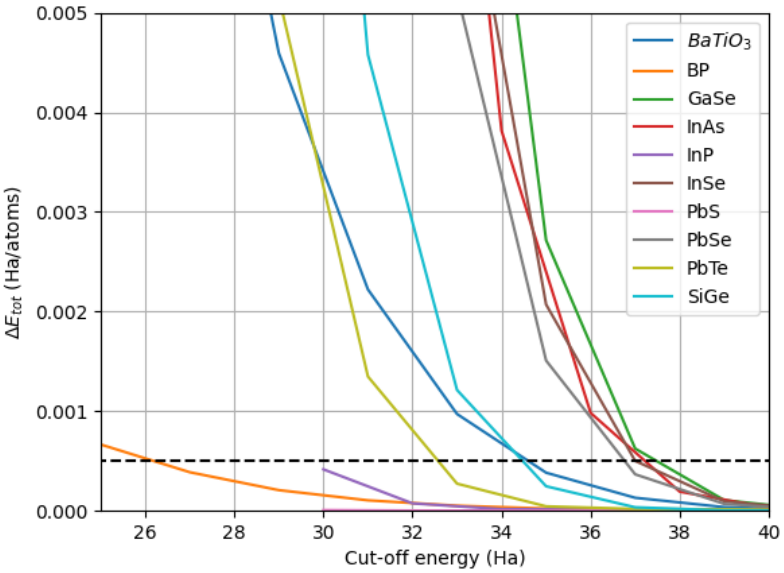

Figure 18: Residual errors on the atomization energies (the total bonding energies between ions) as a function of the cut-off energies (including SOC for the PbX elements). The dotted black line is the convergence criteria.

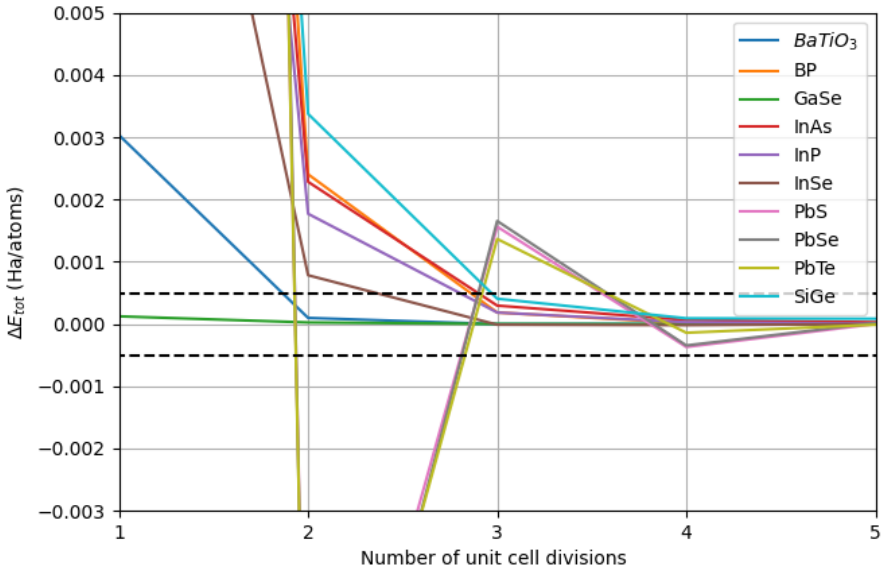

Figure 19: Residual errors on the atomization energies (the total bonding energies between ions) as a function of the number of divisions of the Brillouin zone (including SOC for the PbX elements). The dotted black line is the convergence criteria.

Keeping in mind the arbitrary value of $\Delta E_{tot} < 0.5mHa$, one can easily observe that for a cut-off energy of 40 Ha and 4 divisions par unit cell, the ground state properties should be quite accurate for all of the materials. The lead chalcogenides (PbX elements) exhibit a quite strange, but not unusual, behavior in their convergence via the number of k points.

4.2.2 With respect to the lattice parameters

However, the total energy is not the only criteria to help in the determination of the optimal cut-off energy or number of k points. The internal atomic positions and size of the input cell should also be optimized. This is called a structural relaxation. Thanks to the Broyden-Fletcher-Goldfard-Shanno method implemented within ABINIT, the input structure parameters (size of the input cell and position of the nuclei) will be optimized until the forces reach 5.10^{-5} Ha/Bohr. This relaxation can be performed with different ecut and ngkpt to estimate the optimal parameters. The results are shown in figure 20 and 21.

The ecut and ngkpt used for each of those calculations were the ones from the convergence study with respect to the total energy. The criteria to reach is set to have a 0.2% relative error (or less) on the final lattice parameters.

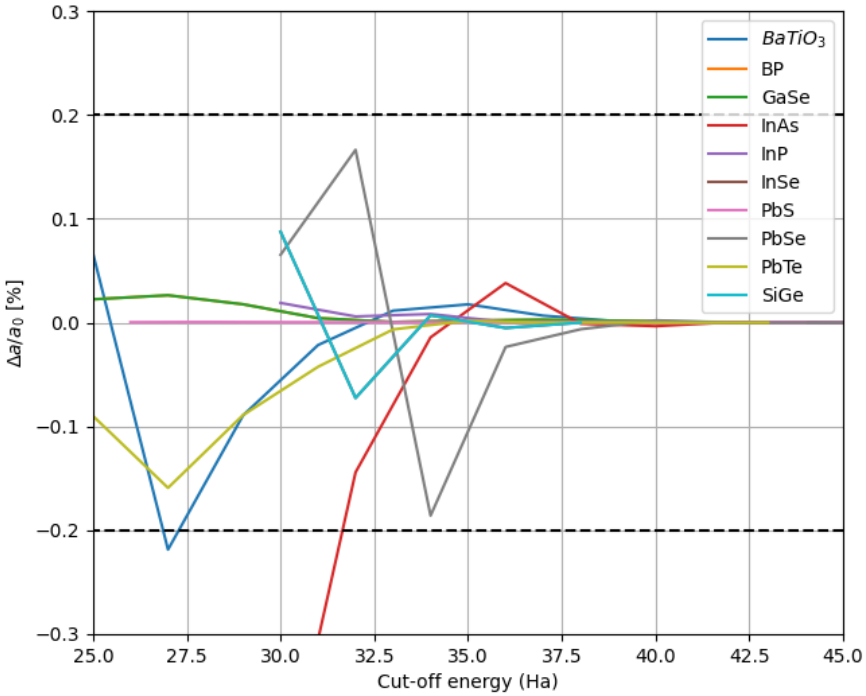

Figure 20: Errors on the lattice parameters as a function of the cut-off energies (including SOC for the PbX elements). The dotted black line is the convergence criteria.

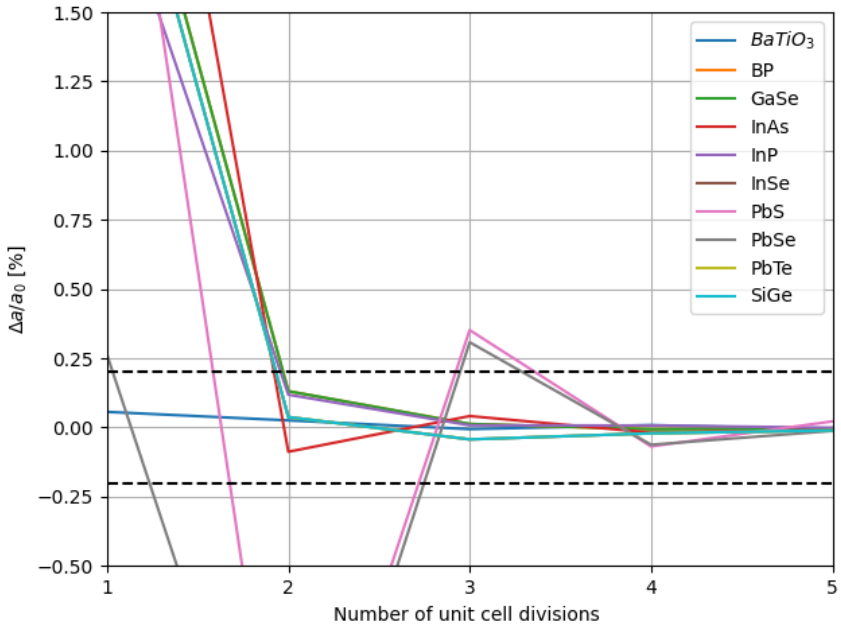

Figure 21: Errors on the lattice parameters as a function of the number of k points in the unit cell (including SOC for the PbX elements). The dotted black line is the convergence criteria.

Since this convergence study uses energy-wise converged parameters as a starting point, the quality of the results is a bit better than previously (meaning that convergence is reached quicker). This explains why in figure 20, all the materials have reached convergence ($\frac{\Delta a}{a_0} < 0.2\%$) for a energy cut-off of 32 Ha. The number of k points is a bit slower to converge but eventually, for 4 division per unit cell, all of the materials appear to reach the equilibrium position within 0.2%.

To ensure to select the best final ecut and ngkpt possible for each material (for the ground state properties), one can re-use the parameters obtained when studying the lattice constants convergence in the convergence study with respect to the total energy. Doing that, then the same procedure to re-evaluate the lattice constant convergence with the new ecut and ngkpt, one can be sure the ground state properties are well-converged. Table 4 gathers the main results so far :

	ID	Space group	Lattice	Sites	ecut [Ha]	k points sampling
InAs	mp-20351	$F\bar{4}3m$	cubic	2	38	$4 \times 4 \times 4$
InP	mp-20305	$F\bar{4}3m$	cubic	2	32	$4 \times 4 \times 4$
BP	mp-1479	$F\bar{4}3m$	cubic	2	31	$3 \times 3 \times 3$
SiGe	mp-1219182	$F\bar{4}3m$	cubic	2	35	$4 \times 4 \times 4$
PbS	mp-21276	$Fm\bar{3}m$	cubic	2	40	$6 \times 6 \times 6$
PbSe	mp-2201	$Fm\bar{3}m$	cubic	2	39	$5 \times 5 \times 5$
PbTe	mp-19717	$Fm\bar{4}m$	cubic	2	35	$4 \times 4 \times 4$
GaSe	mp-568263	$P\bar{6}m2$	hexagonal	8	37	$4 \times 4 \times 2$
InSe	mp-20485	$P\bar{6}m2$	hexagonal	8	37	$5 \times 5 \times 3$
$BaTiO_3$	mp-5020	R3m	rhombohedral	5	35	$3 \times 3 \times 3$

Table 4: Summary of the materials and their converged parameters used for ground state calculations.

The energy cut-off varies between 31 Ha and 40 Ha while the coarser k point sampling of the BZ is $3\times3\times3$ and the finest is $6\times6\times6$. For all materials, the k point sampling must be multiplied by 4 different shifts (the center of the k point sampling is respectively [0.0,0.0,0.0],[0.5,0.0,0.0],[0.0,0.5,0.0] or [0.0,0.0,0.5]). For the materials with a hexagonal crystal structure, the z direction lattice constant is quite high (typically one order of magnitude than the x and y direction), meaning that in reciprocal lattice, this direction is very small, hence the need for less k points in that direction.

While this is only valid for ground state calculations, it is a good starting point for other computations. However, in this work, each electronic and vibrational calculation was studied separately and their parameters were subject to specific post-convergence studies. The convergence of the DFT cycle is handled by ABINIT via some well-thought criteria on either the forces, the wavefunction, the density, etc. Depending on the wanted results, the stopping criteria used is the tolerance on the relative difference of forces (tolrff, for the relaxation of the structure), the tolerance on the potential V(r) residual (tolvrs) or the tolerance on the wavefunction residuals (tolwfr), for the preparatory GS calculations before a RF calculation. No formal convergence studies were done on those parameters, but in line with the literature, it is assumed that tolwfr = 10^{-22} and tolrff = 5×10^{-5} lead to acceptable accuracy (those two criteria were preferred to tolvrs).

4.3 Workflows

Following the convergence study and the structure relaxation, let us now illustrate how is computed the zero point renormalization from electron-phonon interaction and zero point lattice expansion. To speed up the most time-consuming steps, the Abipy workflows are very handy. These workflows handle the communication between all the dataset and file inputs/outputs of the different steps needed. As it is very common to re-use the output of a calculation as an input file for the next, Abipy provides a elegant interface to do this. What is more, it uses python language, which is quite user-friendly.

4.3.1 ZPR from EPI Workflow

The electron-phonon interaction computation in ABINIT is divided in several steps :

1. An initial ground-state calculation, used to produce the wavefunctions and electronic density (WFK and DEN files). This run is usually done with a dense k-point grid to make sure to converge every property (a converged $8 \times 8 \times 8$ k point grid is the recommended value [4])

2. A DFPT calculation for each atom, each direction of displacement, q points in the Brillouin zone (the q grid is the vibrational equivalent of the k grid, dividing the BZ in $q \times q \times q$

segments). For the present work, the q grid used is the same than the k grid. In addition, the Born effective charge and the dielectric matrix are also computed. This is the most time-consuming step handled by Abipy.

3. The merging of all Derivative DataBase and Derivative of V(r) DataBase (DDB and DVDB files), from each run of the DFPT calculation. This is necessary as one DFPT run produces only a partial DDB file and POT file (for one q point and one perturbation of one atom). Merging those is done using the mrgddb and mrgdv utilities of ABINIT.

4. Another WKF computation, to generate WFK file on a denser k mesh. This is not an obligatory step as one can just use the wavefunctions of step 1. However, when the q-mesh interpolation is wanted, the k mesh need to be denser (hence the utility of this step)

5. Finally, the electron-phonon driver uses all the previously computed files to estimates the zero point renormalization from EPI using the procedure described in Section 2.5.

The relation and dependencies of those steps are illustrated in figure 22.

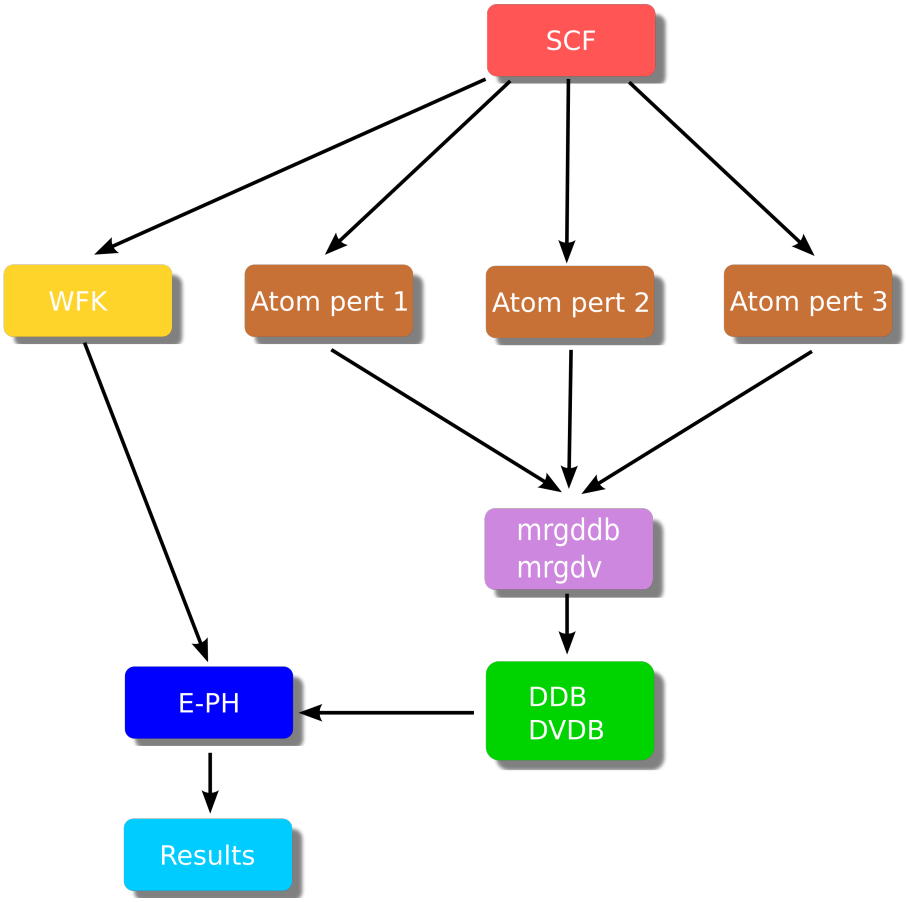

Figure 22: Typical workflow of a electron-phonon matrix computation (taken from the ABINIT website).

One consideration to take into account is the crucial step of the ZPR from EPI with respect to the q mesh sampling. The electron-phonon properties converge slowly with the number of q points in the BZ (if no linear extrapolations are used). Since the DFPT takes an important time to compute, a trade-off has to be found between the accuracy of the results versus the time it can realistically take. This will be detailed in the 'Result and analysis' chapter.

4.3.2 ZPLE workflow

Once the ground state convergence studies and initial structure relaxations are done, the typical workflow of the zero point lattice expansion of a material can be divided in 5 main steps :

1. The computation of volume-constraint structures (including the Born-Oppenheimer volume, without volumic constraint). The volumes used for all materials were 2% spaced ($V_1 = 0.96V_{BO}$, $V_2 = 0.98V_{BO}$, etc). It is the case for every materials, except for the hexagonal materials (GaSe and InSe). For those peculiar cases, the Gibbs energy variation with respect to volume is very weak, and more important volume changes were needed. The value of 2% was found to be effective in reducing the impact of numerical errors on phonon calculations [4].

   Each of the pressured structures were then relaxed keeping their volume constant while all other degrees of freedom were adapted to minimize the residual forces. For most of the materials, varying from -4%V_{BO} to +6%V_{BO} leads to correct phonon band structure (for hexagonal lattice structures, to obtain a good enough relation between Gibbs free energy and volume change, the volumes range from -8%V_{BO} to +18%V_{BO}).

2. For each volume, the DFPT routine in Abipy was taken advantage of to produce the derivative database. For this step, the vibrational wave-vector sampling were $8 \times 8 \times 8$ for all materials (except hexagonal lattice structures, GaSe and InSe, for which the q grid is $8 \times 8 \times 6$, due to very long van der Waals bonds in the z direction). This was chosen to lessen the error from the QHA to a minimum while still keeping the computational time to a manageable minimal value.

3. The partial databases are merged together by the mrgddb utility and the phonon density of state (PHDOS files) are extracted using the Gaussian method, with a DOS smearing value of η =20 mHa. This method gives smoother phonon density curves, which are preferred for the QHA. The phonon density for all materials can be found in the appendix B.

4. Using the PHDOS.nc and GSR.nc (from the ground state calculation) files for all the volumes, the Gibbs free energy can be expressed as a function of temperature and volume change. In this work, the temperature is considered from T = 0K to T = 700K (except for the PbS, PbSe and PbTe, for which the QHA gives accurate results up to $T \sim$ 300K). A finite difference method can then extract the thermal expansion coefficient from the Gibbs free energy derivative, and from that, the volume change as a function of temperature.

5. The last step involves taking the difference between the computed volume for T = 0K and the Born-Oppenheimer volume (from the initial relaxation run) and, assuming a uniform dilatation along the 3 directions x, y and z (hypothesis to be discussed), computing the new primitive lattice parameters from the volume change at T = 0K. With this new unit cell, perform a electronic band structure calculation to estimate the ZPLE.

Those steps are summarized in figure 23.

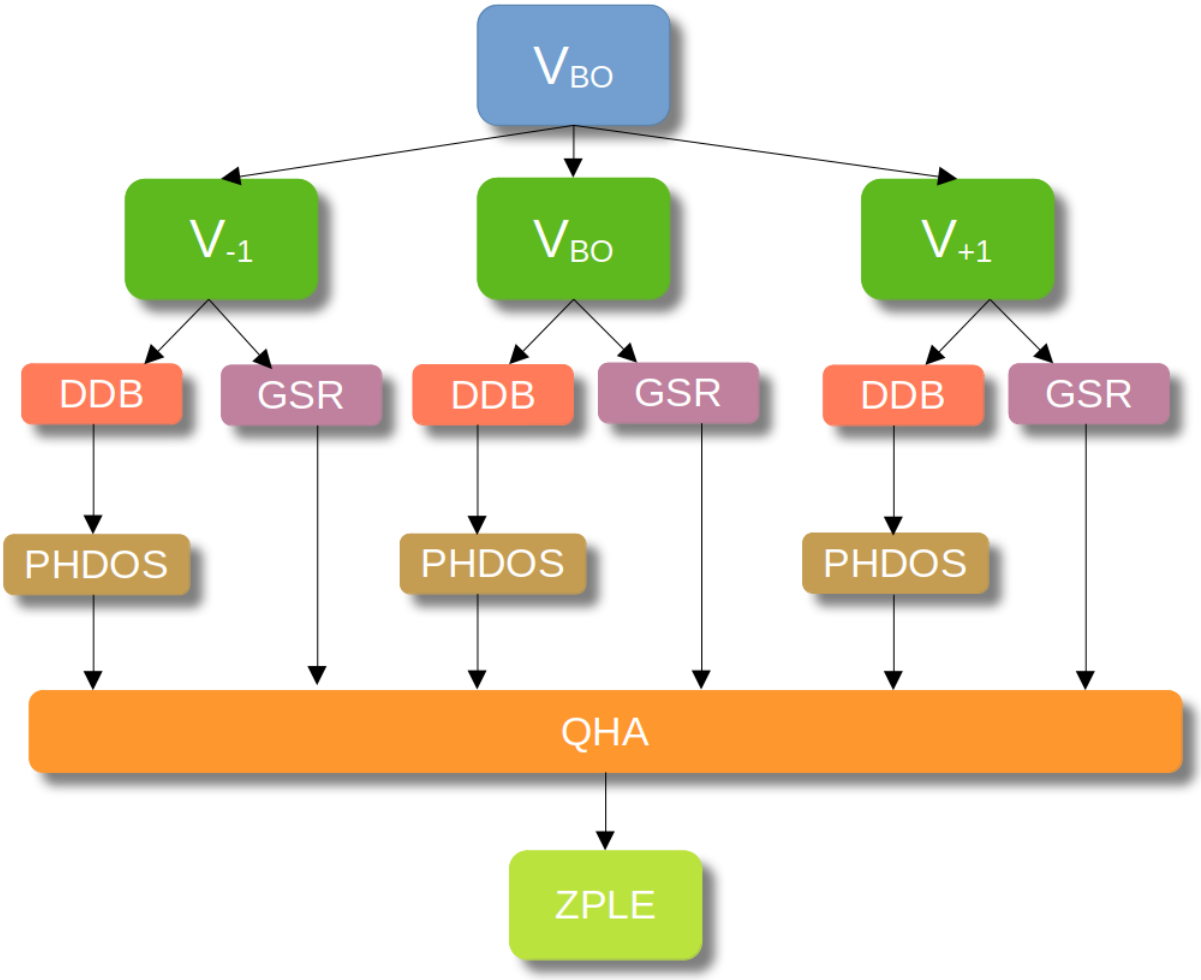

Figure 23: Typical workflow of the determination of the ZPLE via the QHA method.

4.4 Parallelization and computational time

One of the biggest challenge with this type of DFPT calculation is the computer resources available as well as the time taken for the calculation (even more so when studying the convergence with respect to the q point sampling, like in this case, for the zero point renormalization from EPI). Fortunately, parallel computations can speed up the process (up to a certain point). Indeed using more than one processor gives access to more memory, making specific computer operations much more efficient. For modern days computer resources, multi-core processors are a necessary requirement. A local computer usually has about 8 to 16 cores at its disposition (though, one can hardly launch a parallel run on all of them as the system also need resources to operate). The best computer infrastructures have several million cores. This section explains the parallel possibilities of ABINIT and how they were used to perform calculations in this work.

They are two type of possible parallelization : over the k point grid and over the q point grid.

1. The k point parallelization distributes the number of k points in the Brillouin zone among the available CPU resources. The appropriate distribution of those quantities between the number of CPU available is automatically handled by the ABINIT parallelization routine (activated with the flag 'autoparal' = 1). The parallelization of other quantities such as the number of band or the FFT points (from the Fast Fourier Transform) is also possible.

   There is however, a limit to the speed up factor that can be reached with this parallelization. As the number of CPU increases, the communication between the sequential parts of the

calculation start to take more time (relative to the computation time of one CPU). This is known as the Amdahl's law. A trade-off has to be found as if the number of CPU increases, the less time each one will take for its part of the computation, but the more the time of communication between each CPU increases. This relation is shown in figure 24.

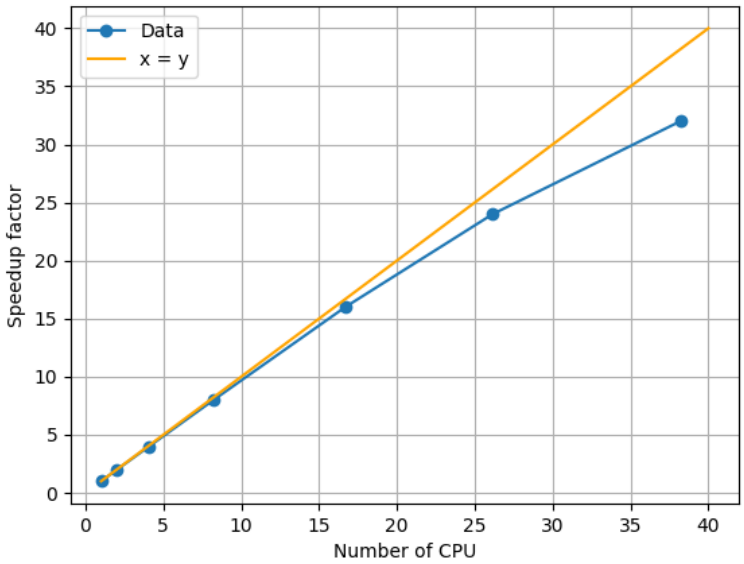

Figure 24: Illustration of the speed-up factor limitation for the lead crystal system (ground state calculation, with $12 \times 12 \times 12$ k point grid, taking into account the BZ symmetries, this represents 182 k points). If the number of k point is not a multiple of the number of the CPU, the distribution of the processes among the processors is not optimal.

Based on this simple test, for 36 CPU, the speedup factor is about 32 (which is still quite good). There is, however, a limit to the number of CPU and to the allocated memory per CPU one can use simultaneously on the Nic5 server.

2. The q point parallelization is handled by the Abiflow routine. Each run is subdivided according to its number of q point, the number of perturbation (3, one in each direction) and the number of atoms. For a 2 atoms system with a $16 \times 16 \times 16$ q grid and no spin, this represents 774 individual runs (of approximately 2 hours each). The biggest limitation when launching calculations (or 'jobs') on the Nic5 server is the number of sequential jobs running at the same time. To guarantee a fair use of the allocated resources, the infrastructure only allow about 30 jobs at the same time for one user (depending on the affluence on the server). Meaning that this system would take about 50 hours to be completed. For bigger systems with 8 atoms (such as the InSe and GaSe), this time increases following the law :

$$T_{CPU} \propto N_{band}.N_{atom}.N_{FFT}.log\left(N_{FFT}\right) \tag{49}$$

Depending on $N_{band}, N_{atom}, N_{FFT}$ respectively the number of band, the number of atoms and the number of point to be treated in the Fourier Transform of the BZ. Overall, for small systems, the time increases roughly $T_{CPU} \propto N_{atom}^2$. For bigger systems, this relation becomes $T_{CPU} \propto N_{atom}^3$ (due to the relation between N_{atom} and N_{FFT}).

5 Results and Analysis

This is the most important chapter of this master thesis. In this chapter, all results will be presented, carefully explained and justified with regard to recent literature.

First, the final lattice parameters from the structural relaxations will be detailed for each material, with comparison with experimental data and similar first-principle studies. Once the input structures are validated, an initial KS band gap calculation will be performed and the results will be, once again, compared to experimental data as well as previous band gap simulations from DFT in recent literature. Then will come the main objectives of this work : the zero point lattice expansion and the zero point renormalization from electron-phonon interactions. The contribution of each mechanism will be studied, and put in perspective of the total band gap. Some specific attention is attributed to the slow convergence of the ZPR from EPI with respect to the q point grid and how it affects the results. In addition to the behavior of those quantities at T = 0 K, this work will evaluate the total band gap temperature dependence for temperature above 0 K. This section will allow the fair comparison with the experimental band gap temperature dependence found in literature and this work.

5.1 Structural relaxation

After determining the optimal converged parameters values for the cut-off energy and the number of k points par unit cell, a last structural relaxation is done in order to find the final cell size and nuclei positions for each material. The Material Project [2] input positions and lattice parameters are an approximate starting point but the structure has to be adapted depending on the exchange-correlation functional or the choice of the pseudo-potentials. Usually, there is a relative error of a few % on the lattice constants (with respect to the exact, experimental, lattice constants) before relaxation. The relaxation allows the decrease of this relative error of about one order of magnitude. Typically, after relaxation, the relative errors are on the order of a few tens of % of the lattice constants (for most materials at least). This is shown in the table 5:

		This work	Experimental data		Other DFT works	
Materials	Lattice	a,c,γ [Å]	a,c,γ [Å]	diff. [%]	a,c,γ [Å]	diff. [%]
InAs	cub.	a = 6.189	a = 6.058 [60]	+2.166	a = 6.188 [61]	+0.019
InP	cub.	a = 5.881	a = 5.868 [62]	+0.233	a = 5.972 [63]	-1.503
BP	cub.	a = 4.735	a = 4.777 [64]	-0.880	a = 4.810 [32]	-1.559
SiGe	cub.	a = 5.539	a = 5.538 [45]	+0.027	a = 5.48 [46]	+1.086
PbS	cub.	a = 6.009	a = 6.055 [65]	-0.751	a = 5.922 [65]	+1.478
PbSe	cub.	a = 6.217	a = 6.259 [65]	-0.655	a = 6.104 [65]	+1.867
PbTe	cub.	a = 6.390	a = 6.619 [65]	-3.455	a = 6.470 [65]	-1.231
ϵ-GaSe	hex.	a = 3.820	a = 3.823 [41]	-0.072	a = 3.743 [41]	+2.064
		c = 18.471	c = 17.848 [41]	+3.485	c = 15.919 [41]	+11.93
ϵ-InSe	hex.	a = 4.058	a = 3.999 [66]	+1.492	a = 4.159 [67]	-2.412
		c = 17.467	c = 16.699 [66]	+4.602	c = 17.365 [67]	-0.590
$BaTiO_3$	rhomb.	a = 3.993	a = 4.004 [68]	-0.274	a = 4.073 [68]	-1.964
		γ = 89.861	γ = 89.9 [68]	-0.043	γ = 89.710 [68]	-0.168

Table 5: Final structure of each material. The other DFT works chosen used a GGA exchange-correlation functional along with PBE pseudopotentials (while this work uses PBEsol pseudopotentials, the results are very similar). For the hexagonal elements, a and c are different, so they are both gathered here (similarly to $BaTiO_3$, $\gamma \neq 90°$).

As expected, the agreement between the results of this work and the experimental data is rather good. For the major part of the material dataset, the relative difference is lower than 1%. Some material lattice constants appear to still be a few % off the experimental structure (the InAs is 2.1 % off and the PbTe is 3.4% off). Moreover, when comparing our results to other simulation works using the same pseudopotentials and model, the relative difference is not increasingly more

important than for other materials, which is reassuring.

When investigating the relaxation of layered materials, they appear to be rather inaccurate with respect to experimental data (for GaSe, a difference of 3.4% and for InSe, a difference of 4.6 %) or with respect to recent similar studies (for GaSe, with an astonishing 11% difference between other DFT work and our result). In both case, it occurs in the z-direction. This is because while the LDA, GGA or other common popular exchange-correlation functionals accurately describe the ground state properties of most materials, they fail to properly address the nonlocal dispersion effects in density-functional theory. Those effects play an important part in the van der Waals and weak bond interaction modelling (present in layered hexagonal materials). One need to adapt the choice of the exchange-correlation functional when treating with GaSe and InSe, to obtain a correct lattice prediction in the z-direction.

Within ABINIT, they are several choices of exchange-correlation functionals including the van der Waals effects. In this work, the three most common corrections are investigated : the vdw-DFT-D2, the vdw-DFT-D3 and the vdw-DFT-D3(BJ). The tolerance criteria is set to 10^{-10}. This means that if a pair of atoms contributes for less the 10^{-10} eV to the total energy, it is not included in the dispersion potential. The results obtained for InSe and GaSe are gathered in table 6.

	GGA		DFT-D2		DFT-D3		DFT-D3(BJ)	
	a,c [Å]	diff. [%]	a,c [Å]	diff. [%]	a,c [Å]	diff. [%]	a,c [Å]	diff. [%]
ϵ-GaSe	a=3.820	0.072	a=3.751	1.806	a=3.797	0.602	a=3.774	1.204
	c=18.471	3.485	c=17.593	1.262	c=17.633	1.038	c=17.565	1.419
ϵ-InSe	a=4.058	1.492	a=3.917	2.050	a=4.095	2.400	a=4.014	0.0375
	c=17.467	4.602	c=17.265	1.156	c=16.830	3.646	c=16.944	2.994

Table 6: Comparison table of the lattice parameters obtained with different van der Waals exchange correlation functional (DFT-D2, DFT-D3 and DFT-D3 (BJ)) and their difference with respect to experimental results.

Based on this table, it seems that for the ϵ-GaSe, the best van der Waals functional is the DFT-D3 (less than 1% difference on the covalent bonds and about 1% difference for the van der Waals bonds). However, the ϵ-InSe is best described by the DFT-D2 functional (even if it fails to predict with accuracy the other lattice constant). In this work, to standardize the results obtained for the two layered materials, the last vdw functional was used (DFT-D3 (BJ)). While it does not correctly describe the van der Waals bonds for ϵ-InSe, it is the most acceptable trade-off between the three.

Since the van der Waals functionals are not implemented for PBEsol pseudopotentials, simple PBE pseudopotentials are used in those relaxation runs (still with the stopping criteria being that that the residual forces are below 5.10^{-5}Ha/Bohr).

Overall, the use of those exchange-correlation functionals is not perfect (for those two systems at least) as the results are not much better than for the simple PBEsol-GGA case. Indeed the relative errors in the z-direction are much decreased, but it seems it comes at the price of the covalent bonds accuracy, which decreases with the use of VdW functionals. In other systems however (such as argon, graphite or benzene, done in other studies), the simulation/experimental data agreement is much better with specific VdW functionals. This is because in those systems, the initial first relaxation is far off the theoretical value (about 10 %)[69, 70], whereas in both ϵ-GaSe and ϵ-InSe, the initial agreement was already rather good.

5.2 Kohn-Sham band gap

As the electronic band gap is a critical property in this work, its computation is done with a finer k mesh grid than the GS properties. The electronic path in the Brillouin zone depends on the structure of the material, since the high-symmetry points are not situated at the same relative coordinates for each structure. The band gap is found in an automatized manner with an Abipy script. For the lead chalcogenides (PbS, PbSe, PbTe), the spin-orbit coupling was included as it has a significant contribution to the difference of energy levels (and not in other materials). Unfortunately, with the spin orbit coupling, the degeneracy of the levels is lift up and the band gap is reduced to 0 (while ABINIT still find an energy difference of few meV, this is called a numerical zero). If the band gap is decreased to 0, the materials does not behave like a semiconductor anymore and the computation of the ZPR from EPI and ZPLE is not possible. To solve this issue, it has been chosen to study those materials under artificial pressure to create a band gap. This is also the case for InAs, which has a very small experimental band gap. This is a questionable choice as such a pressure would also change the lattice parameters and ionic positions of the atoms (meaning the phonon dispertion relation is also changed, along with the properties). The hydrostatic pressures were chosen so that the KS direct band gaps were approximately the same than experimental ones.

The main results are gathered in table 7.

Materials	Direct/Indirect	KS band gap [eV]	Exp. band gap [eV]	Refs
InAs (@ 16.97 GPa)	direct	0.344	0.35	[30]
InP	direct	0.556	1.34	[30]
BP	indirect	1.228	2.02	[31]
SiGe	indirect	0.606	0.95	[71]
PbS (@ 9.51 GPa)	direct	0.424	0.42	[38]
PbSe (@2.47 GPa)	direct	0.267	0.27	[38]
PbTe (@13.23 GPa)	indirect	0.247	0.31	[38]
ϵ-GaSe	direct	1.367	2.13	[44]
ϵ-InSe	direct	0.463	1.25	[44]
$BaTiO_3$	indirect	2.761	3.4	[52]

Table 7: Kohn-Sham band gaps (computed in this work) versus experimental band gaps (at T = 300K).

While DFT cannot correctly predict the value of the band gap (as previously explained in chapter 2.2.2), it can however predict the position of the minimum of the conduction band and the maximum of the valence band, determining the type of the gap (direct or indirect). As suspected, the error on the band gap is rather important (up to about 1 eV). But the focus of this work is put on the temperature dependence of the band gap, not the band gap itself. This is why this - very inaccurate - electronic band gap suffices for this work goal. The calculation is about $\Delta\epsilon_g(T)$, and in previous investigations [8],[72], the accuracy has been shown to be largely independent on on the KS value ϵ_g^{KS}. For the PbTe, one can observe that if the band gap opens under the pressure, it is no longer a direct band gap but an indirect one.

The total electronic structures for each material are available in the appendix A.

To summarize, due to the inability to correctly model the van der Waals interaction with PBE or PBEsol, InSe and GaSe have been relaxed with DFT-D3(BJ) functional (and therefore, its pseudopotentials are PBE not PBEsol like the rest of the materials), PbS, PbSe and PbTe are including the spin orbit coupling in all their calculations (except DFPT phonon structure calculation, since SOC has little effect on vibrational properties, while enormously increasing the CPU time) and are under artificial pressure, like InAs (to open its band gap).

5.3 Temperature dependence of the lattice parameters and zero point lattice expansion

5.3.1 Gibbs free energy

As explained in the theoretical background, for each material, the Gibbs free energies are plotted for each temperature (from T = 0 K to T = 800 K) and the minimum of the interpolation curve slightly changes with respect to temperature. This is shown in figures 25-34.

The blue curves are the energies for different temperature (with the first curve at the top being the energy at T=0 K with phonon energy, not the Born-Oppenheimer volume). For increasing temperature, at constant volume, the free energy decreases. The lowest curves correspond to T = 800K. The red dots are the volume minima of the interpolated curves. The fitting interpolation is a fourth degree polynomial.

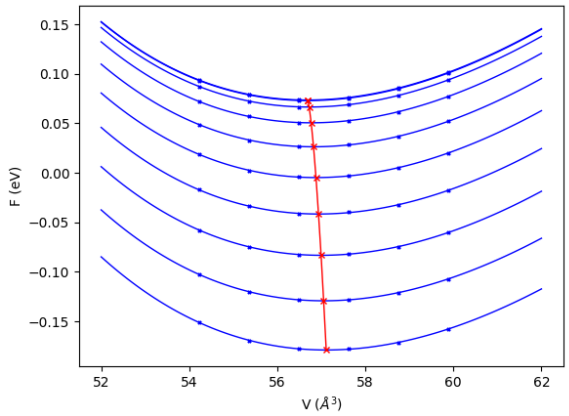

Figure 25: Gibbs free energy per unit cell as a function of the unit cell volume, for InAs, for different temperatures, ranging from 0K (upper blue curve) to 800K (lower blue curve) by steps of 100K. The red line indicates the position of the minimum. This determines the optimal volume at each temperature.

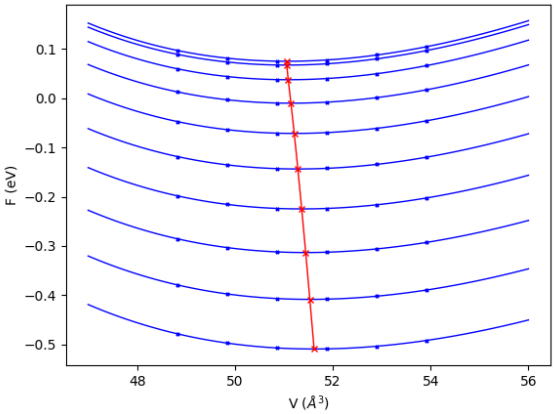

Figure 26: Same as Fig 25, for InP.

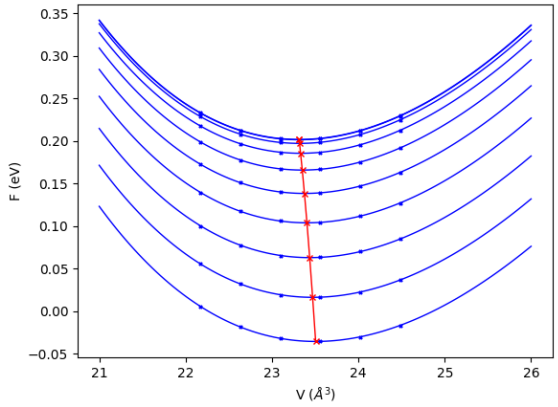

Figure 27: Same as Fig 25, for BP.

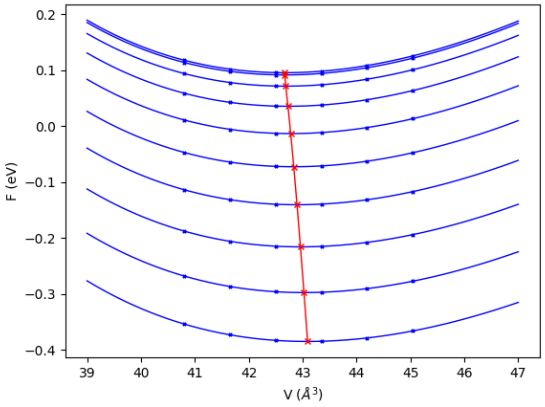

Figure 28: Same as Fig 25, for SiGe.

For simple cubic structures with $F\bar{4}3m$ space group (zincblende materials) such as InAs, InP, BP and SiGe, the computed curves seems to behave as wide parabolas. The highest energy range

for those volumes (from 0.96%V_{Bo} to 1.06%V_{BO}) and temperature is about 0.6 eV per unit cell (for the InP).

For layered materials, the energy profiles is much less parabola-looking. The free energy minima appears to be located on an energy plateau, having a very flat behavior. This means that around the energy equilibrium, an important change in volume does not lead to a significant change in the Gibbs free energy. The energy range for a constant volume from T = 0K to T = 800K is much more important than it was for zincblende materials: about 3 eV. However, the energy shown here is for the entire unit cell. Since GaSe and InSe have 8 atoms per unit cell, they also have a proportionally larger energy in the unit cell. Also, the equilibrium volumes for the hexagonal primitive cell are much bigger than for other materials (due to, once again, the important c lattice constant in the structure). More volumes have been plotted for the GaSe to obtain an accurate energy profile and a good fitting. However, it appeared that there was no need for such detailed profile as 6 different volumes with enough spacing between them lead to somewhat acceptable fitting (such as the InSe energy profile).

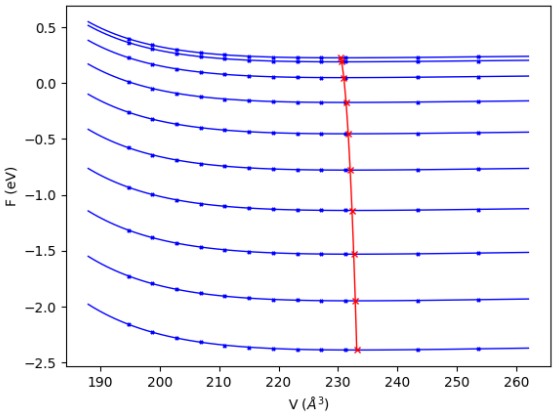

Figure 29: Same as Fig 25, for GaSe.

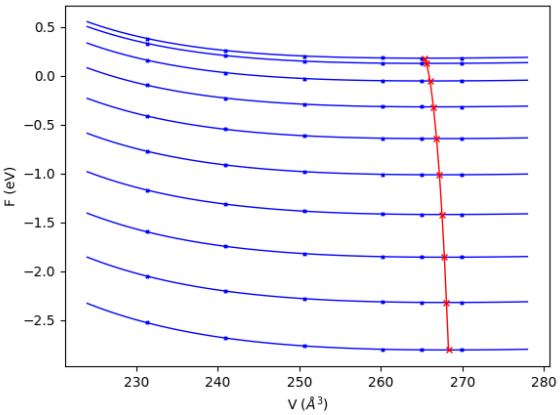

Figure 30: Same as Fig 25, for InSe.

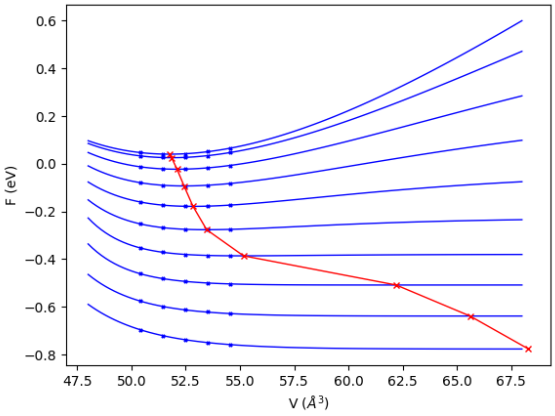

Figure 31: Same as Fig 25, for PbS.

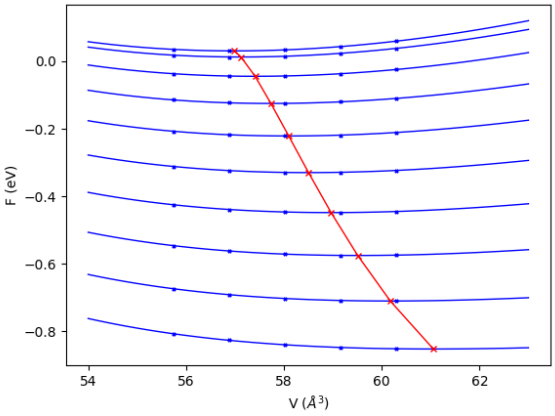

Figure 32: Same as Fig 25, for PbSe.

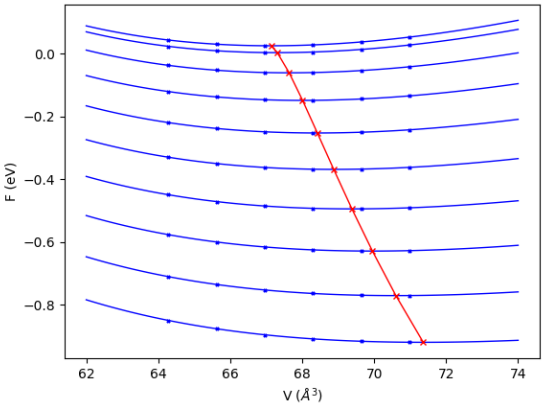

Figure 33: Same as Fig 25, for PbTe.

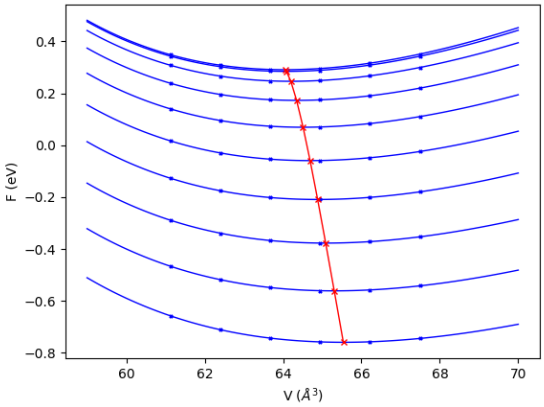

Figure 34: Same as Fig 25, for $BaTiO_3$.

The lead chalcogenides exhibit a very peculiar behavior at high temperature. The volume equilibrium seems to shift relatively fast compared to classic, homogeneous dilatation. This is due to their strongly anharmonic lattice dynamics. Their rocksalt structure causes a large off-centering of the Pb cation at high temperature (reported in literature [73]) which amplitude is still under discussion. The motion of the central ion changes the input cell structure (the cell size and obviously the nuclei positions) and the QHA, counting on the volumic relaxation under hydrostatic pressure constraint, does not provides accurate results anymore. For those materials, the maximum temperature for which the QHA would still stand is about T = 300K. Above T = 300K, the structure changes and the method is doomed to fail. This effect is particularly visible with the PbS case, for which the minimum of the fitting curves is located between our initial volumes at T = 0K but when the temperature increases, this minimum goes 'out' of the initial -4%V_{BO} - +6%V_{BO} range (for approximately T > 500K).

Knowing the equilibrium volume for each temperature in each material, the temperature dependent volume can be found.

5.3.2 Temperature dependent volume

Figure 35-44 show the computed temperature dependence of the volume for all materials considered.

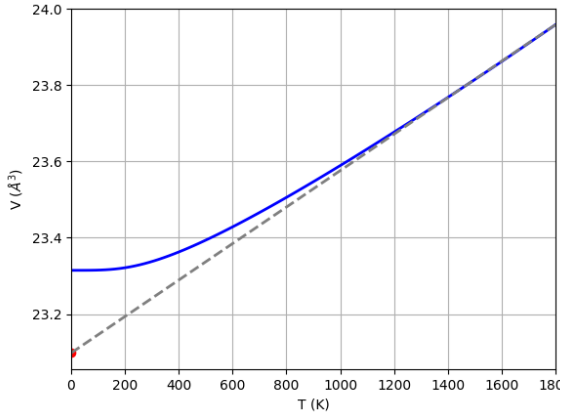

Figure 35: Temperature-dependent volume per unit cell curve (in blue) for InAs. The Born-Oppenheimer volume at T = 0K is the volume without the phonon energy contribution (red dot). The gray dashed line is the linear relation extrapolated toward $T \to 0$K

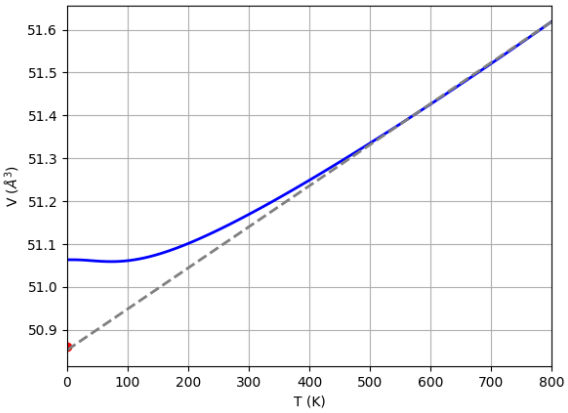

Figure 36: Same as Fig 35, for InP

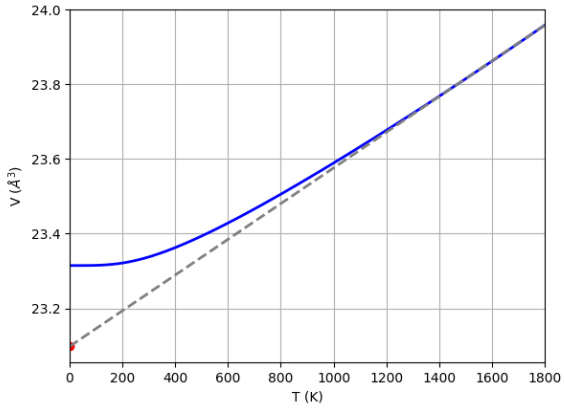

Figure 37: Same as Fig 35, for BP

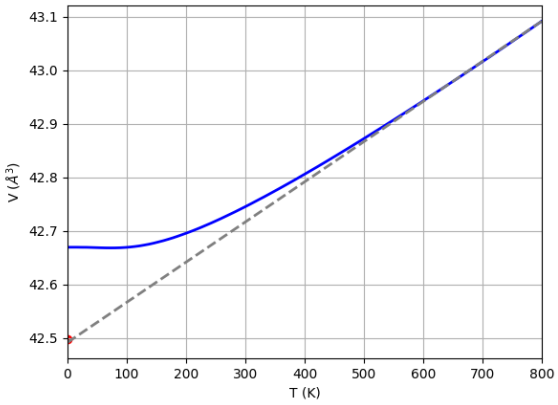

Figure 38: Same as Fig 35, for SiGe

The blue curves are the volume computed from the phonon energy from T = 0K to T = 800K while the red dot is the Born-Oppenheimer volume (without any phonon energy). Those figures illustrates the non-zero volume contribution from the lattice vibrations (even at T = 0K). The vertical distance between the Born-Oppenheimer volume and the volume from QHA at T = 0K is linked to the $\frac{1}{2}$ in equation 40 and 45 (since the Bose-Einstein distribution vanishes when $T \to 0$). This effect is called the zero-point lattice expansion (since it expands the lattice parameter at T = 0K).

The zero-point lattice expansion for typical cubic materials is about 0.1% to 0.5% [28], meaning that InAs, InP, BP and SiGe all fall in the expected range.

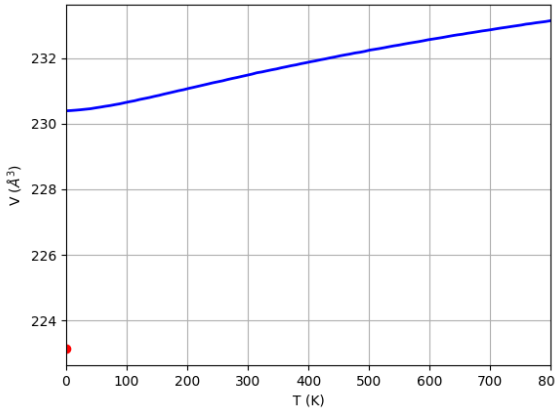

Figure 39: Same as Fig 35, for GaSe

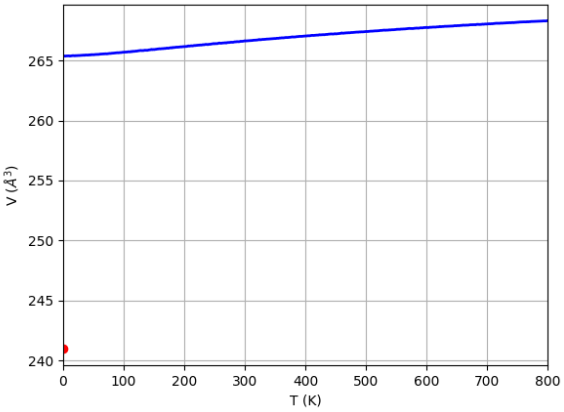

Figure 40: Same as Fig 35, for InSe

Our two hexagonal materials GaSe and InSe are not well described within the QHA method. Indeed, the phonon energy contribution to the volume is too important with respect to the Born-Oppenheimer volume (shown here in figures 39 and 40). There are several possibilities to explain this phenomena :

- The van der Waals functionals used for the cell relaxation do not provide accurate DFPT results, hence the phonon density of states may be a few percent off;
- The van der Waals weak bonding along the z-direction in the crystal leads to serious anharmonic effects that are not well modelled within the quasi harmonic approximation.
- Taking only the volume change into consideration might yield an error since for anisotropic systems, the v-ZSISA (volumetric Zero Static Internal Stress Approximation) method used in this work does not treat the a lattice parameter and the z lattice parameter separately.

The phonon properties were well-converged with respect to the q and k point grid, with a rather high energy cut-off, eliminating the possibility that this is a numerical error linked to a too coarse grid or underconverged parameters.

A more correct approach would be to plot the free Gibbs energy as an hypersurface, function of both the a and z parameters. Different hypersurfaces would be obtained for different temperatures and for each global minimum, the corresponding a and z values would be a better description of the unit cell under thermal stress. This is actually being investigating by S. Rostami and colleagues at UCLouvain, but is outside of the range of this work. Unfortunately, this means that the ZPLE obtained for bidimensional materials such as GaSe and InSe are not realistically correct (as the phonon energy cannot physically contributes for 10% of the total cell volume).

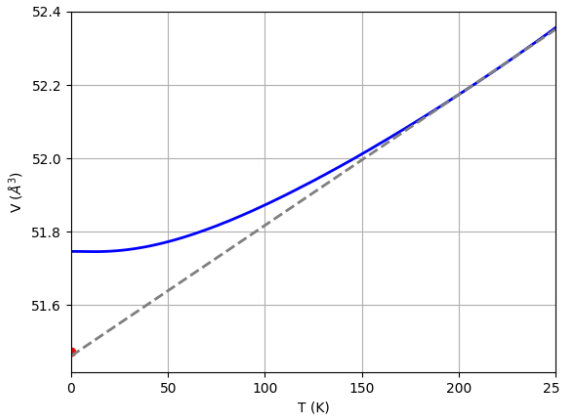

Figure 41: Same as Fig 35, for PbS

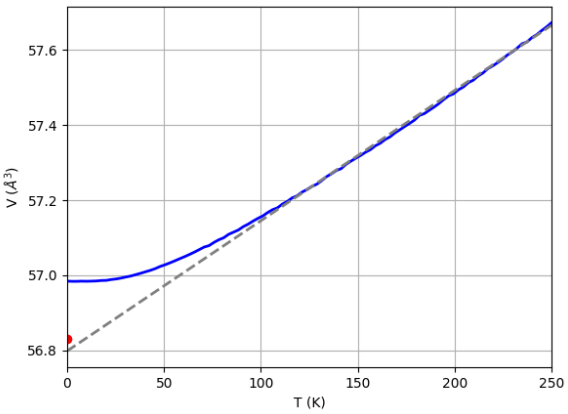

Figure 42: Same as Fig 35, for PbSe

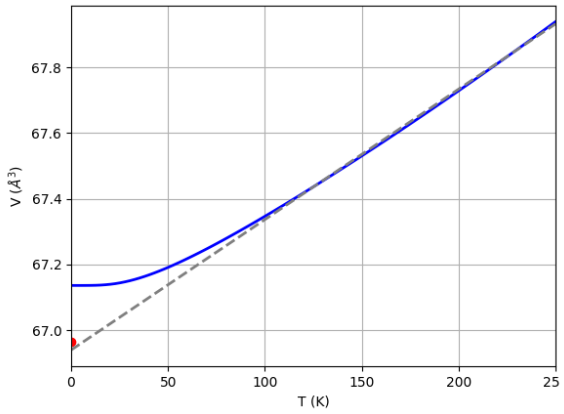

Figure 43: Same as Fig 35, for PbTe

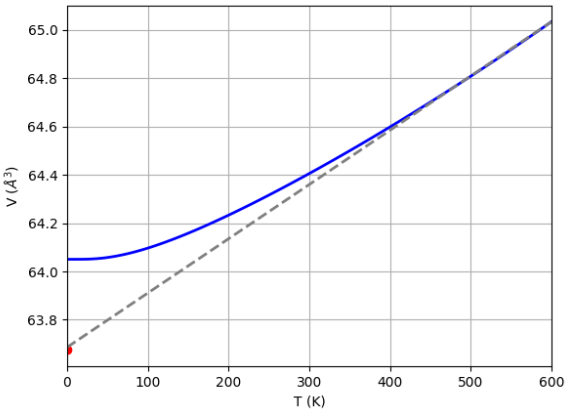

Figure 44: Same as Fig 35, for $BaTiO_3$

As mentioned above, for the lead chalcogenide materials, the results are considered for temperature ranging from T = 0K to T = 250K. For most materials, the extrapolation of the linear region of the temperature dependent volume toward $T \to 0$ gives the Born-Oppenheimer volume. The exception being the hexagonal materials, GaSe and InSe, for which the QHA method does not work (under these conditions).

5.3.3 ZPLE and temperature dependence

Finally, the zero point lattice expansion can be found, assuming a homogeneous dilatation in all three directions for each materials. This is an additional hypothesis, for non-cubic materials. For cubic materials, the dilatation is uniform in all three directions. On the contrary, hexagonal materials do no have uniform dilatation in x, y, z direction but rather most of the change in the volume cell comes from the z direction. The van der Waals bonds are more easily stretched out and compressed since there are weak bonds. This induces errors, but it simplifies the following treatment of the volume changes from the figures 35-44 as the change in lattice constant is assumed to the difference between the volumes with and without phonon energy at T = 0K, both elevated to the $\frac{1}{3}$ power:

$$\Delta a(T=0) = \sqrt[3]{V(T=0)} - \sqrt[3]{V_{BO}} \tag{50}$$

Once the change in the lattice parameters is found for T = 0K, a new KS electronic band structure is computed with the new parameters (from the original BO volume, with an additional uniform

scalingof the structure). Taking the difference between this band gap and the band gap for the Born-Oppenheimer volume previously calculated, one can evaluate the phonon energy contribution to the electronic band gap.

The results of the ZPLE (at T = 0K) and for T = 300K (ambient temperature) are gathered in table 8.

		T = 0K		T = 300K	
Materials	a_0[Å]	$\Delta a/a_0$[%]	$\Delta\epsilon_g^{ZPLE}[eV]$	$\Delta a/a_0$[%]	$\Delta\epsilon_g^{T=300K}[eV]$
InAs(@ 16.97 GPa)	3.836	0.118	-0.052	0.176	-0.077
InP	3.705	0.127	-0.020	0.196	-0.031
BP	2.847	0.309	-0.014	0.342	-0.016
SiGe	3.489	0.134	-0.068	0.193	-0.097
PbS (@ 9.51 GPa)	3.719	0.177	-0.010	0.701	-0.045
PbSe (@ 2.47 GPa)	3.845	0.063	-0.007	0.577	-0.057
PbTe (@ 13.23 GPa)	4.060	0.084	-0.006	0.591	-0.016
ϵ- GaSe	6.065	0.931	-0.116	1.098	-0.135
ϵ- InSe	6.222	3.267	-0.231	3.427	-0.240
$BaTiO_3$	3.993	0.196	-0.017	0.381	-0.043

Table 8: Lattice expansion (in percent) and band gap renormalization for each material for T = 0K and T = 300K.

Based on this table, for all of the materials selected, the ZPLE band gap contribution (at T = 0K) is negative and on the order of few tens of meV. As expected from their temperature dependent volume graphs, the lattice dilatation for the hexagonal elements (GaSe and InSe) is not realistic, thus the band gap renormalization is not either. Those two materials should be disregarded within the QHA. The lead chalcogenides elements (PbX, with X = S, Se, Te) have a rather low band gap correction at T = 0K (with regards to other elements) but their thermal expansion coefficient are quite high (the volume increases rapidly with temperature). This means that at ambient temperature, the band gap contribution from lattice expansion is also important. This is due to their relatively small Debye temperature, from which the volume increases quite quickly with respect to the temperature ($\Theta_D \approx 25K$).

5.4 Zero-point renormalization from EPI

Having computed the ZPLE, the temperature dependence of the lattice parameter, and their effect on the band gap for each material, let us now characterize the zero point renormalization (ZPR) from electron-phonon interactions (EPI).

5.4.1 Q points sampling convergence

As previously stated, this property converges slowly with respect to the number of q points. Careful convergence studies are required to investigate this effect. However, the number of q point is a difficult property to scale-up, due to the important computational time needed for the DFPT calculations. To properly address this issue and speed up the convergence with respect to the q-point sampling, several different methods can be used (from the Supplementary Materials ref [28]):

- A linear extrapolation of the data points based on the expected scaling $N_q^{-1/3}$, with N_q the number of q points in the Brillouin zone;
- The Fröhlich model associated with the missing $q = 0$ part of the Brillouin zone;
- The interpolation of the DFPT potential along the q point grid.

The first method, the linear extrapolation, is very straightforward and does not requires any extra calculation to be performed (it is done using the numpy package of Python). The second method is

a bit more complex. The initial description of the Fan contribution in the 'Theoretical Background 'chapter is incomplete as it fails to mention that this contribution does not account for the q point [0.0, 0.0, 0.0] (named Γ). This region of the BZ is called Ω_0. The volume of this missing area is the BZ volume divided by the number of q points sampling, N_q :

$$\Omega_0 = \frac{\Omega_{BZ}}{(N_q)^3}. \tag{51}$$

The Fröhlich correction can be obtained with :

$$\Delta^{q=0}\mathrm{ZPR}_c^{\mathrm{AHC}} \approx -\frac{8\pi}{\Omega_0}\left(\frac{3}{4\pi\Omega_0}\right)^{1/3}(N_q)^{-1/3}K_{av}, \tag{52}$$

with K_{av} can be written :

$$K_{av} = \frac{1}{4\pi}\int_{4\pi} d\hat{q}\sum_j \left(\frac{\hat{q}.p_j(\hat{q})}{\omega_{j0}(\hat{q})\epsilon^{\infty}(\hat{q})}\right)^2, \tag{53}$$

where the dependence to $\hat{q}$ is explicitly written. This factor (and thus the Fröhlich correction) is inversely proportional to the vibrations mode ω_{j0} and to the dielectric constant, ϵ^{∞}. The slope of the correction will strongly depends on the Born effective charges of the material. This correction is also valid for the valence band, provided that the minus sign in equation 52 is changed. The full methodology of the Fröhlich model is detailed in the study done by Dr. Brousseau [28].

In this present work, both techniques are used (the linear extrapolation and the Fröhlich model) to ensure the results are as converged as can be. Fortunately, the Fröhlich correction can be deduced from a previous DDB file (meaning is takes very little time to get the correction for the $q = 0$ point). For materials with indirect band gap, both the maximum of the valence band and the minimum of conduction band position in the Brillouin zone must be evaluated separately. The plots from which the convergence is studied are based on the OTMS approximation correction. To keep this section clear, QP correction were not included in the graphs (although the two methods reported very similar results with less than 3 meV of difference for most on the materials at T = 0K). All results were obtained using $\eta = 0.01$eV (as explained previously, this variable is meant to avoid the divergence of the Fan-Migdal term of the electron-phonon self-energy). Several values for η have been tested (0.1 eV, 0.01 eV and 0.001 eV) for different materials. It appears that there is less than 1 meV of difference between the ZPR obtained with $\eta = 0.01$ eV and with $\eta = 0.001$ eV (see Appendix C, figure 73)

The goal is to obtain a 10% accuracy over all the materials. The result are illustrated as a function of N_{MP}, the number of q points sampling in the Brillouin zone for different Monkhorst-Pack grids.

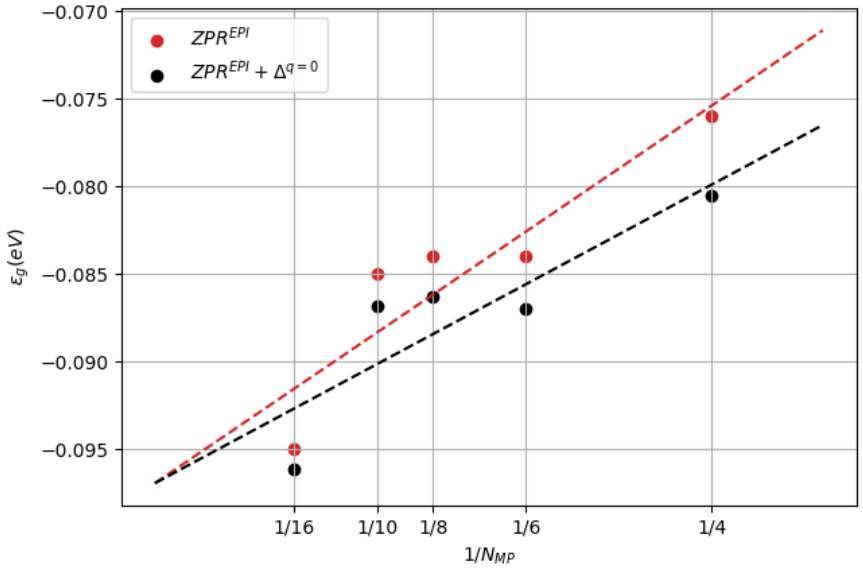

Figure 45: InP convergence study of the ZPR from EPI at the Γ point with (in black) and without (in red) the Fröhlich correction. The dotted lines are the linear extrapolation toward an infinitely dense q mesh.

The most converged value of InP (for $N_{MP} = 16$) has a 10 meV difference with the second most converged value ($N_{MP} = 10$), which is a non-negligible difference. The linear extrapolation is affected by that and the final result is guaranteed within approximately a ±5 meV certitude range. The final ZPR is taken for an infinitely dense q mesh, meaning that it is the intersection between the linear extrapolation and the vertical line $N_{MP} \to \infty$.

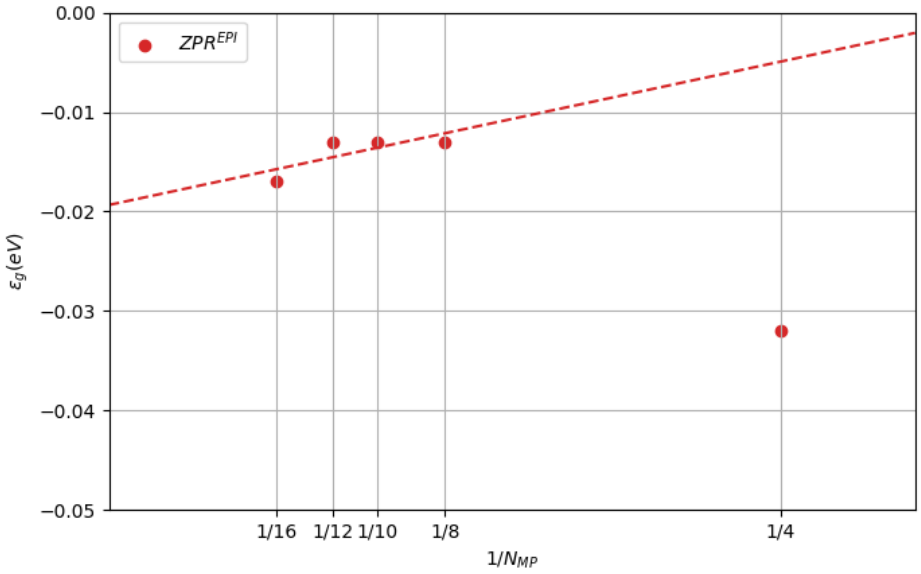

Figure 46: Same as fig. 45, for InAs . The $4 \times 4 \times 4$ q point grid was not included in the linear extrapolation as it is severely underconverged.

For the InAs, the ZPR value seems to be converged for $N_{MP} = 8, 10, 12$ but with a phonon

wavevector $N_{MP} = 16$, this value changes (4 meV of difference with the previous value). This plateau around $N_{MP} = 10, 12$ is a recurrent phenomena as it appears in other materials as well.

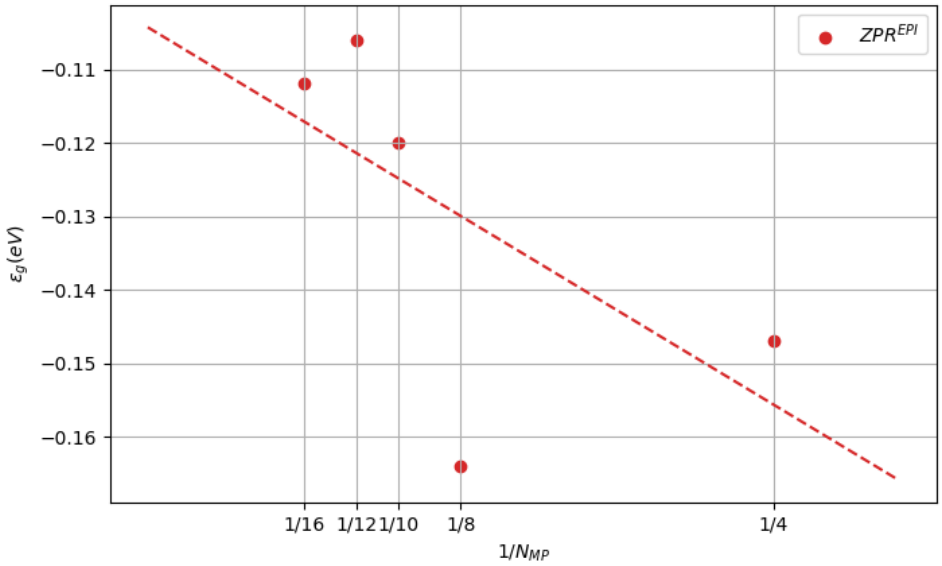

Figure 47: Same as fig. 45, for BP at the Γ and X point (for an indirect band gap).

For the BP convergence, the $8\times8\times8$ q point grid appears to be less converged than the $4\times4\times4$ q point grid. This is an unusual behavior, since one could expect the coarse grid to not include every effect of the structure, but the most converged values are in agreement with the coarser grid.

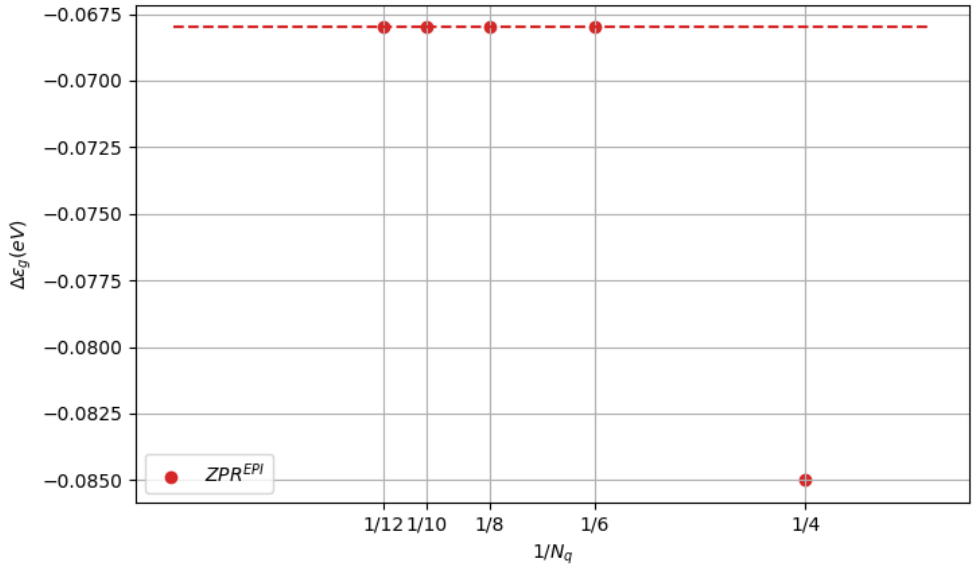

Figure 48: Same as fig. 45, for SiGe at the Γ and X point (for an indirect band gap). The $4\times4\times4$ q point grid was not included in the linear extrapolation as it is severely underconverged.

The SiGe convergence is very peculiar. All the q point grid tested output the same ZPR value ($\Delta\epsilon_g = -0.068$[eV]). Even though the unit cell has the same structure than the three last materials

(InP, InAs and BP, zincblende structure), the convergence is reached with much coarser q grids than those materials. What is more, since all the converged points have exactly the same value, the linear extrapolation is a perfectly horizontal line, meaning that the error on this extrapolation is null (as well as the difference between the final y intercept and the most converged value).

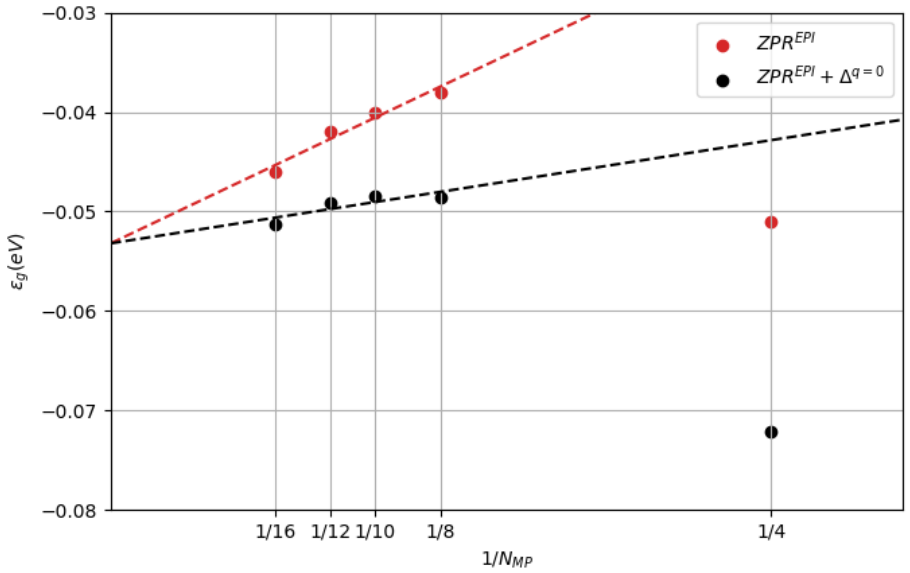

Figure 49: Same as fig. 45, for PbS at the L point. The $4 \times 4 \times 4$ q point grid was not included in the linear extrapolation as it is severely underconverged.

The PbS convergence with respect to the q point sampling is following the expected trend $\Delta\epsilon_g \propto (N_q)^{-1/3}$. In addition, the gap between the the final ZPR value and the one obtained from the most converged q grid is about 2 meV difference (with the Fröhlich correction).

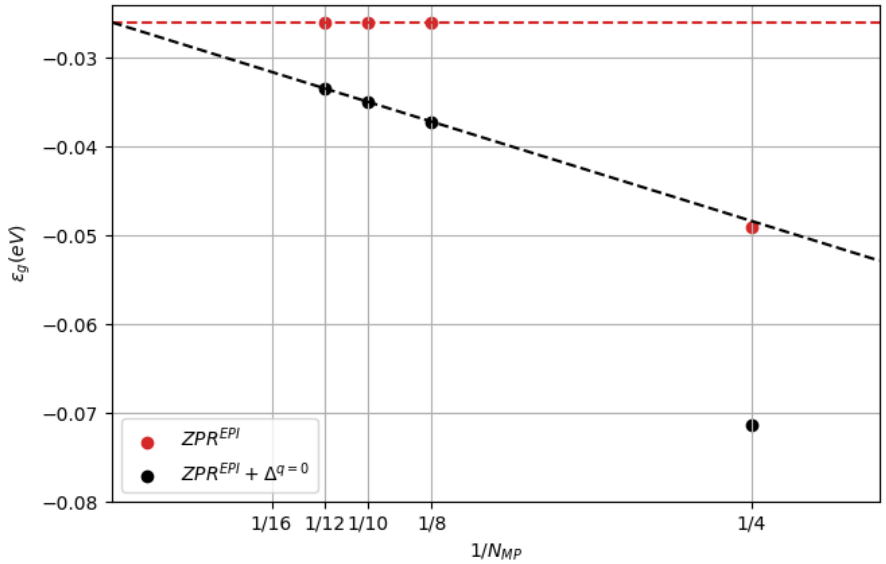

Figure 50: Same as fig. 45, for PbSe at the L point. The $4 \times 4 \times 4$ q point grid was not included in the linear extrapolation as it is severely underconverged.

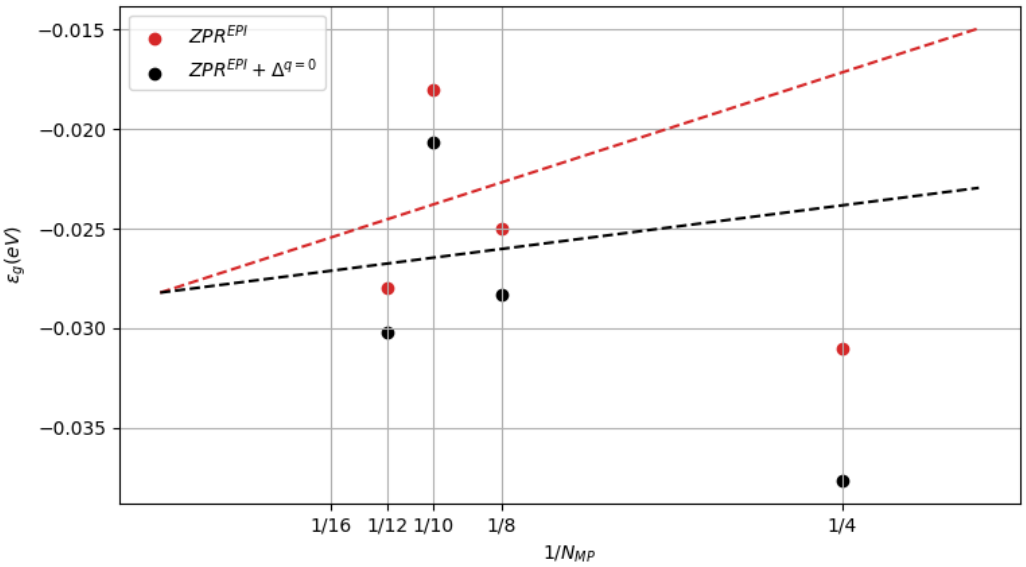

Figure 51: Same as fig. 45, for PbTe at the L point. The $4 \times 4 \times 4$ q point grid was not included in the linear extrapolation as it is severely underconverged.

While for the PbSe, all three points $N_{MP} = 8, 10, 12$ are the same value (placing them on a horizontal line), for the PbTe however, the results are a bit more scattered. However, the energy range is rather small between them (about 15 meV), showing that the final zero point renormalization from EPI for the PbTe is numerically accurate within ±10meV. Both for the PbSe and PbTe, no $16 \times 16 \times 16$ q grid was computed, due to the important additional time it would have required (including the spin-orbit coupling doubles the amount of time each calculation takes). The Fröhlich correction was computed without spin-orbit coupling coupling as it is not implemented within ABINIT (the use of fully relativistic pseudopotentials throws an error during the execution).

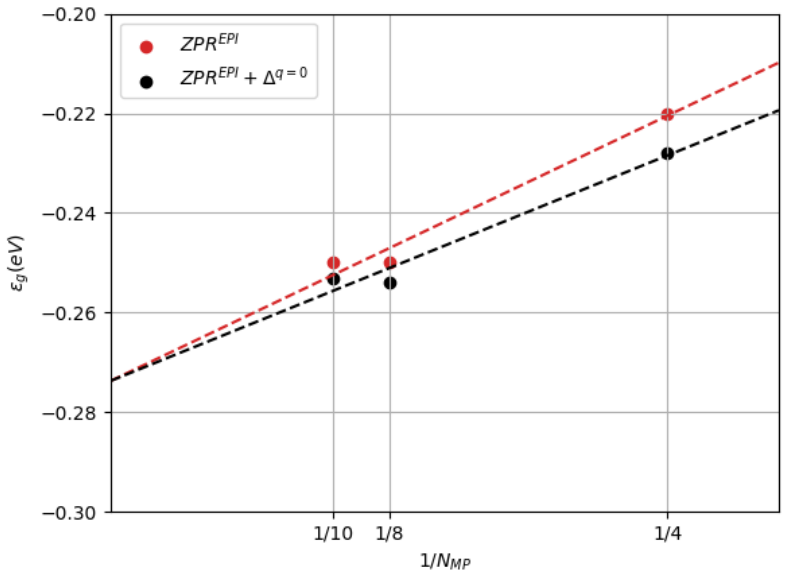

Figure 52: Same as fig. 45, for GaSe at the Γ point.

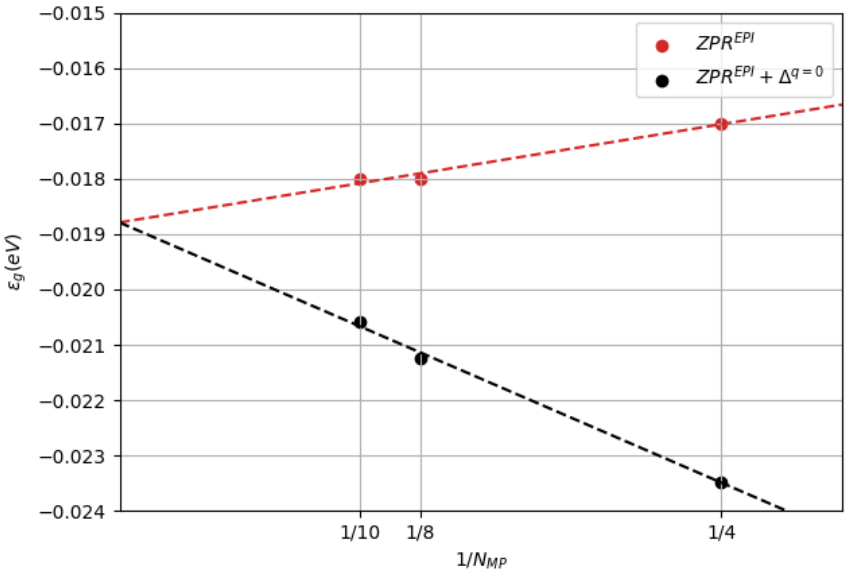

Figure 53: Same as fig. 45, for InSe at the Γ point.

Given the fact that there are only three points for hexagonal materials, the final ZPR values may not be as precise as one could wish them to be. While for the InSe, the three points are very close in value (within 2 meV), for the GaSe, an additional (more converged) point is required to drop the error gap between the final ZPR value and the most converged point (the $4 \times 4 \times 4$ q point grid is probably too coarse).

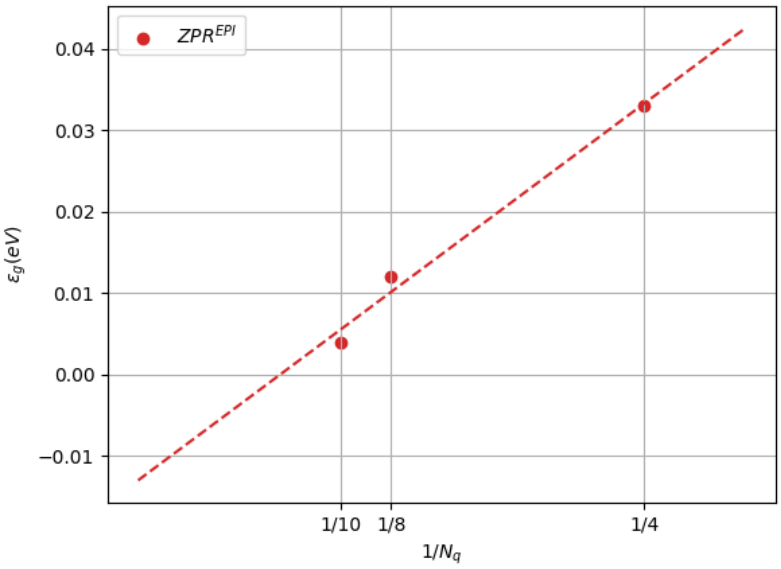

Figure 54: Same as fig. 45, for $BaTiO_3$ at the Γ and Z point.

For materials with more than 2 atoms per unit cell (namely the $BaTiO_3$, with 5 atoms and the InSe/GaSe, with 8 atoms), the computations were not performed for the $16 \times 16 \times 16$ q point grid. This would have required too much time to fit into the timescale of this work.

For all materials, when the Fröhlich slope correction is very close to the initial linear extrapolation, it was not shown on the graph (to keep it as clear as possible). This concerns typically materials with very important dielectric constant (for $BaTiO_3$, $\epsilon^{\infty} \approx 30$) or very high optical mode frequency (for BP, $\omega_{j,max} \approx 1000cm^{-1}$).

Up until this point, the extraction of the final ZPR value was the y-intercept of the linear extrapolation line. However, this may not be the most accurate method to extract it. Indeed, it treats all points the same way, even though the values closer to $1/N_{MP} = 0$ are more converged than the initial $4 \times 4 \times 4$ q point grid. The more converged values should have more weight on the slope of the line than the less converged values. There are several way to correct this :

- one way to take that into consideration is to systematically make sure that the linear extrapolation of the Fröhlich correction passes by the most converged point of the plot,
- one could also perform a fitting with appropriate weights for each point. To get increasingly important weights as the points approach $N_{MP} = 0$, the inverse square method is used. Each point thus have a weight corresponding to its number of q points value. The weight for a point i is :

$$w_i = \frac{1}{(1/N_{MP,i})^2} = N_{MP,i}^2. \tag{54}$$

The visual representations of both methods for all materials are available at appendix C (where 'Correction 1' refers to the first method and 'Correction 2' refers to the weighted least square method).

5.4.2 Results and error analysis

Table 9 gathers the ZPR from EPI with the three extraction methods for the whole material dataset, along with the Fröhlich factor to take into account the missing q = 0 piece.

Materials	Band Gap	$\Delta^{q=0}$ [meV]	ZPR^{EPI} [meV]	$\text{ZPR}_1^{\text{EPI}}$ [meV]	$\text{ZPR}_2^{\text{EPI}}$ [meV]
InAs	$\Gamma - \Gamma$	0.3	-19.3	-20.5	-19.8
InP	$\Gamma - \Gamma$	18.4	-96.9	-100.3	-104.7
BP	$\Gamma - X$	2.9	-104.2	-99.1	-86.1
SiGe	$\Gamma - X$	0.1	-68.0	-68.0	-64.8
PbS	L - L	84.7	-53.2	-53.8	-52.1
PbSe	L - L	89.4	-25.9	-25.9	-19.46
PbTe	L - L	26.6	-28.2	-31.6	-30.9
GaSe	$\Gamma - \Gamma$	31.9	-273.7	-271.2	-266.5
InSe	$\Gamma - \Gamma$	25.9	-18.7	-18.7	-18.5
$BaTiO_3$	$\Gamma - Z$	≈ 0	-12.9	-14.5	-17.5

Table 9: Main results from the zero-point renormalization from electron-phonon interaction for the material dataset (where $\Delta^{q=0}$ is the correction from the generalized Fröhlich model, ZPR^{EPI} is the linear extrapolation from the data points, $\text{ZPR}_1^{\text{EPI}}$ is the same linear extrapolation with the $\Delta^{q=0}$ correction but passing trough the most converged point and $\text{ZPR}_2^{\text{EPI}}$ is a linear fitting with weights corresponding to the inverse square of $1/N_{MP}$)

Looking at this table, the three different methods find very similar results (while the maximal difference is about 18 meV for the BP, the second maximum difference is 8 meV, for the InP). However, one needs to know how much those results can be trusted. The definition of a certitude range is a necessity. This criteria will then be used to determines the relative error on the ZPR

for each extraction method. The certitude range is defined as the difference between the most converged value computed and the final intercept for each method ZPR_i^{EPI}:

$$\mathrm{error}_i = |\mathrm{ZPR}_i^{\mathrm{q,max}} - \mathrm{ZPR}_i^{q\to\infty}|. \tag{55}$$

This arbitrary criteria can be use to assert that the real zero point renormalization value is inside this trust interval centred around $\mathrm{ZPR}_i^{q\to\infty}$.

Materials	$\mathrm{ZPR}^{\mathrm{EPI}}$ error [meV]	$\mathrm{ZPR}_1^{\mathrm{EPI}}$ error [meV]	$\mathrm{ZPR}_2^{\mathrm{EPI}}$ error [meV]	relative error [%]
InAs	± 2.3	±3.5	± 2.8	±11.9
InP	± 0.76	±4.2	± 8.6	± 0.7
BP	± 7.7	±12.8	± 25.8	±7.3
SiGe	0.0	0.0	± 3.0	0.0
PbS	± 1.9	±2.5	± 0.8	±3.5
PbSe	± 7.45	±7.45	± 13.9	± 28.7
PbTe	± 2.0	±1.4	± 0.7	±7.0
GaSe	± 23.7	±21.2	± 16.5	± 8.6
InSe	± 1.7	±1.8	± 2.0	± 9.0
$BaTiO_3$	± 16.9	±18.5	±21.5	±131.0

Table 10: Error ranges for $\mathrm{ZPR}^{\mathrm{EPI}}$ (the linear extrapolation from the data points), $\mathrm{ZPR}_1^{\mathrm{EPI}}$ (the same linear extrapolation with the $\Delta^{q=0}$ correction but passing trough the most converged point) and $\mathrm{ZPR}_2^{\mathrm{EPI}}$ (linear fitting with weight corresponding to the inverse square of $1/N_{MP}$). The relative error is computed for the simple $\mathrm{ZPR}^{\mathrm{EPI}}$, as the two other methods have very similar relative errors.

Obviously this criteria for the error definition favors the materials for which the convergence slope $\propto (N_q)^{-1/3}$ is very slow as well as materials for which the $16 \times 16 \times 16$ q point grid has been computed. This would allow a smaller certitude range. Of course, this also means that for those materials, the ZPRs are just more precise, regardless of the criteria used to express it. Overall the error ranges are rather small. The relative error is a good measure of how much the simulations can be trusted. For most of the materials, the relative error is below 10 %, which is already quite an achievement.

Based on table 10, the first initial method gives the smallest overall error range. However, it does not mean that this method give more precise result, but rather that the final ZPR value (for $1/N_{MP} \to 0$) is closer to the most converged computation done in this study. In addition to this criteria, the numerical error of the curve fitting (using the least squares method) done by Numpy could also be detailed, but it not would give any indication about the convergence of the property. This would simply give an indication of the fitting quality. Materials with only 3 points would have a smaller error even though they are less converged (and materials with more points would have a high numerical error). For example, looking at figure 54, $BaTiO_3$ have a very small numerical error on the fitting of the curve but an important error range when considering the values computed.

For the rest of this report, the results from the ZPR will be exclusively extracted with the first method (the simple linear approximation with the Fröhlich correction). Table 11 summarizes the ZPR from EPI and ZPLE contribution to the band gap at T = 0K.

Materials	KS Band Gap [eV]	ZPLE [eV]	ZPR^{EPI}[eV]		
		$\Delta\epsilon_g^{ZPLE}$	$\Delta\epsilon_g^{ZPR-EPI}$	error range	$\Delta\epsilon_g^{\text{total}}$ [eV]
InAs (@ 16.97 GPa)	0.344	-0.052	-0.019	±0.002	-0.071±0.002
InP	0.556	-0.020	-0.097	±0.001	-0.117±0.001
BP	1.228	-0.014	-0.104	±0.007	-0.118±0.007
SiGe	0.606	-0.068	-0.068	0	-0.136
PbS (@ 9.51 GPa)	0.424	-0.010	-0.053	±0.002	-0.063±0.002
PbSe (@ 2.47 GPa)	0.267	-0.007	-0.026	±0.007	-0.033±0.007
PbTe (@ 13.23 GPa)	0.247	-0.006	-0.028	±0.002	-0.034±0.002
ϵ - GaSe	1.367	-0.116	-0.273	±0.023	-0.389±0.023
ϵ - InSe	0.463	-0.231	-0.018	± 0.001	-0.249±0.001
$BaTiO_3$	2.761	-0.017	-0.013	±0.017	-0.030±0.017

Table 11: Kohn-Sham band gap, ZPLE and ZPR from EPI and total energy contribution to the band gap at T = 0K for the materials dataset

When comparing the two contributions to the band gap at T = 0K, it is clear that the two mechanisms have a very different contribution for each material. They both are negative for each material but they both could be either positive or negative. Unfortunately, it is very difficult to obtain the experimental total zero point energy level of semiconductor and recent studies approaching this problematic are scare (even more so when looking for these specific semiconductors). This is because it has no real applications as such and while the knowledge of band gaps at T = 0K is quite useful, the theoretical contribution of the ZPR from EPI and the ZPLE to this band gap at 0K is much less interesting. The main value of experimental data concerning those quantities is to validate (or invalidate) a model of the temperature dependence of the band gap.

Nevertheless, in 2002, Pässler and his coworkers have studied the renormalization energy for several semiconductors, including InAs and InP. They used a semi-empirical model from the experimental band gap temperature dependence to find the renormalization energy within 10% [72]. For the InAs and InP, they respectively find 21 meV and 54 meV, which is far off the values obtained in this work (respectively 71 meV and 117 meV). For both materials, there is more than a factor of 2 between experience and simulations. However, in this work, InAs was put under pressure, so the phonon spectrum and electronic bands differ a bit from the experimental ones. Also the extraction of the experimental zero point energy requires a band gap measurement for several temperatures to extract a linear behavior. Looking at figure 55, this linear behavior is far from perfect and an error or imprecision could easily arise. At this stage, it is not clear whether theory of experiment, or both, have to be blamed for such discrepancy.

While this analysis has been made for a virtual temperature of 0K, the two mechanisms (ZPLE and ZPR from EPI) are also responsible for the temperature dependence of the band gap.

5.5 Band gap temperature dependence

As previously explained in the 'Theoretical Background' chapter, the electronic band gap is affected by a temperature change, mainly via the phonon energy. This temperature-dependent band gap responds to temperature changes via the two mechanisms. If the temperature increases, the lattice parameters change and thus the electronic structure also change. In addition, if the temperature increases, the phonon population increases, the effect of EPI will be stronger, also leading to a change in the band gap. By summing the two contributions (ZPLE and ZPR from EPI), one can determined the total temperature dependence for a chosen material. The two contributions are detailled in the appendix D for the four materials chosen in this section.

In this section, simulations and experimental data from scientific literature are compared for the InAs (under pressure), InP and SiGe. These three materials have been selected due to the presence of several studies regarding the temperature dependence of their band gap. In addition, the results obtained in this work for the simple cubic zincblende materials (with $F\bar{4}3m$ space group) are relevant and trust-worthy. Other materials, such as ϵ - GaSe and ϵ - InSe present an important error in the estimation of the zero point lattice expansion and would not allow for a fair comparison between simulation and experiences.

As neither the ZPLE band gap contribution nor the ZPR from EPI at T = 0K are usually available for experimental data, the y scale of the figures 55 to 57 is arbitrary shifted to best fit the simulation of temperature dependence of the band gap (only the energy difference between T = 0K and the energy at temperatures above 0K, $\Delta\epsilon_g$, is considered here).

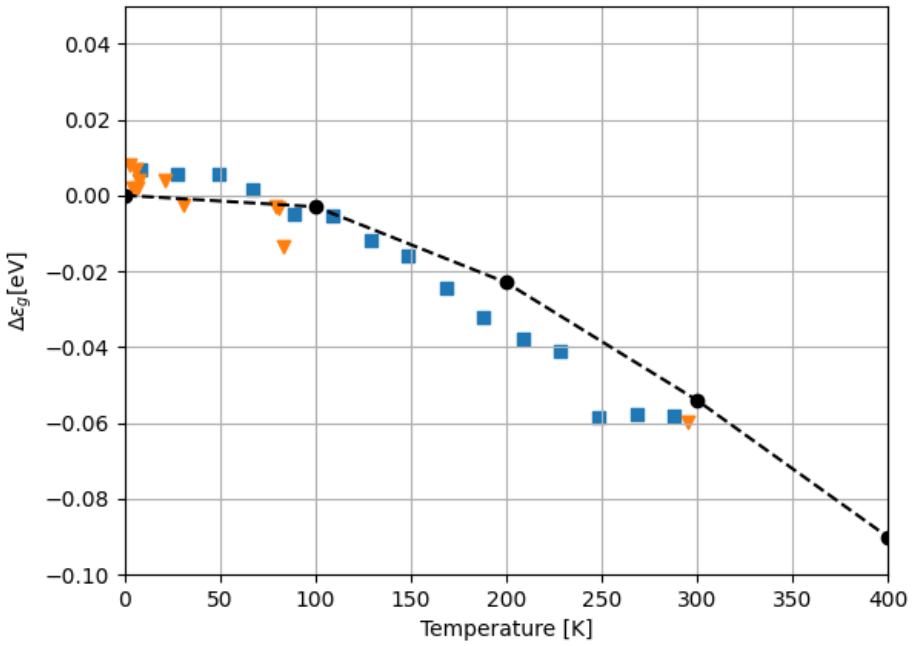

Figure 55: Temperature dependence of the band gap for InP. The dotted black line is the temperature dependence due to both lattice expansion and EPI (computed in this work). Dots are the experimental data (blue squares taken from [74] and orange triangles taken from [75])

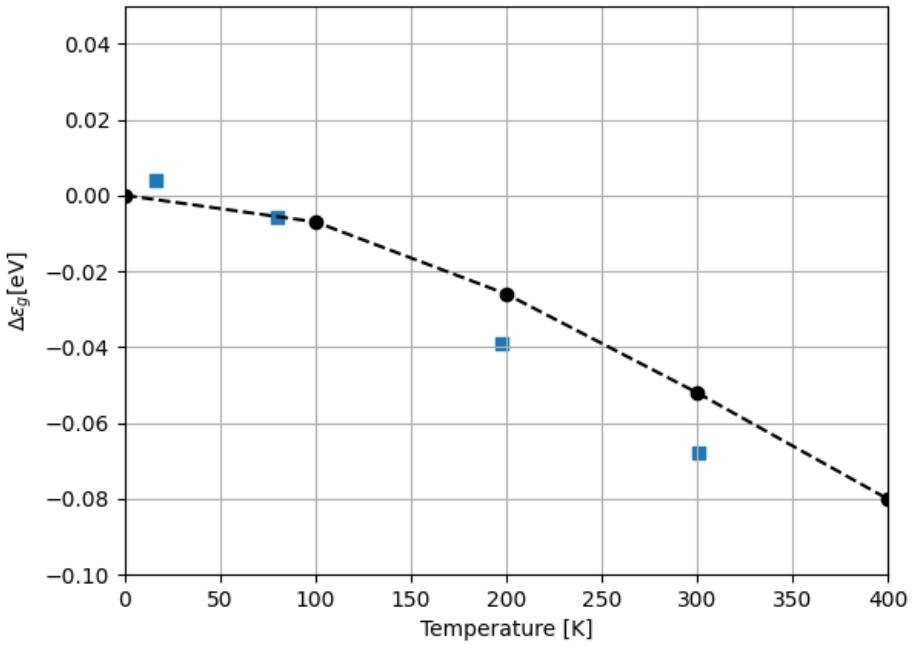

Figure 56: Temperature dependence of the band gap for InAs. The dotted black line is the temperature dependence due to both lattice expansion and EPI (computed in this work). Blue squares are the experimental data (taken from Ref [76])

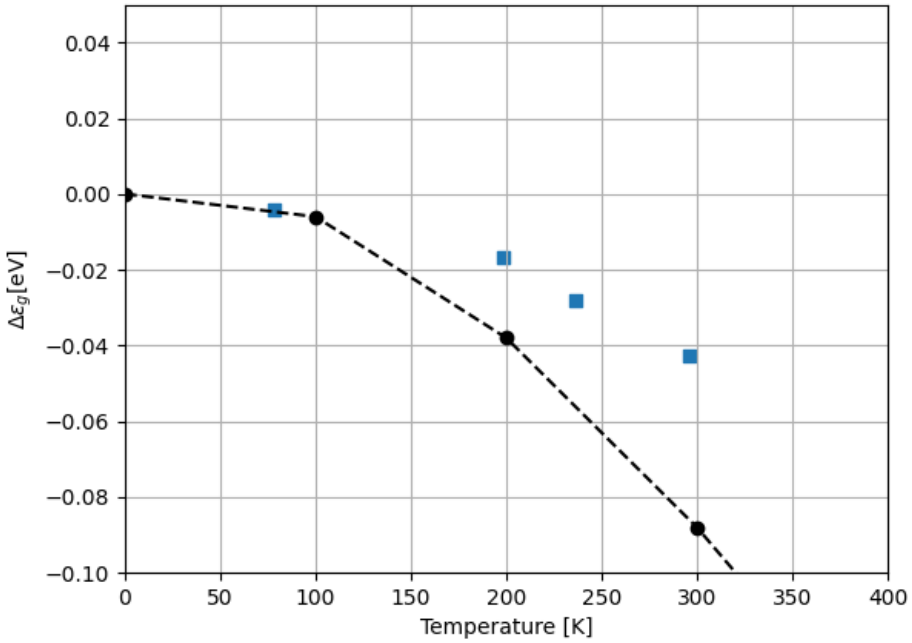

Figure 57: Temperature dependence of the band gap for SiGe (for a 55% Si). The dotted black line is the temperature dependence due to both lattice expansion and EPI (computed in this work). Blue squares are the experimental data (taken from Ref [46])

Based on the figures 55 to 57, it seems that simulations done in this work tend to underestimate the effects of temperature on the band gap renormalization. Since there are no distinction in experimental data between the ZPLE and ZPR from EPI, it is not possible to identify the error with respect to the two computed contributions. The experimental data however are potentially subject to several measurement errors and/or inaccuracies. For the InAs, the structure studied was put under pressure to open its band gap (around 17 GPa of uniform stress) while the experimental data was taken at atmospheric pressure. Also, one have to keep in mind that the SiGe is an alloy, meaning that the temperature dependence is function of the silicon concentration. For the data reported in fig 57, the Si concentration is 55% while in the simulations ab initio, it is 50% Si, 50% Ge. This may induce an error. Finally, the input structure of the SiGe is zincblende cubic when in reality, it is a mix of several phases in one sample, with interfaces, boundaries and defects between the different phases (nothing like the perfect case scenario simulated in this work).

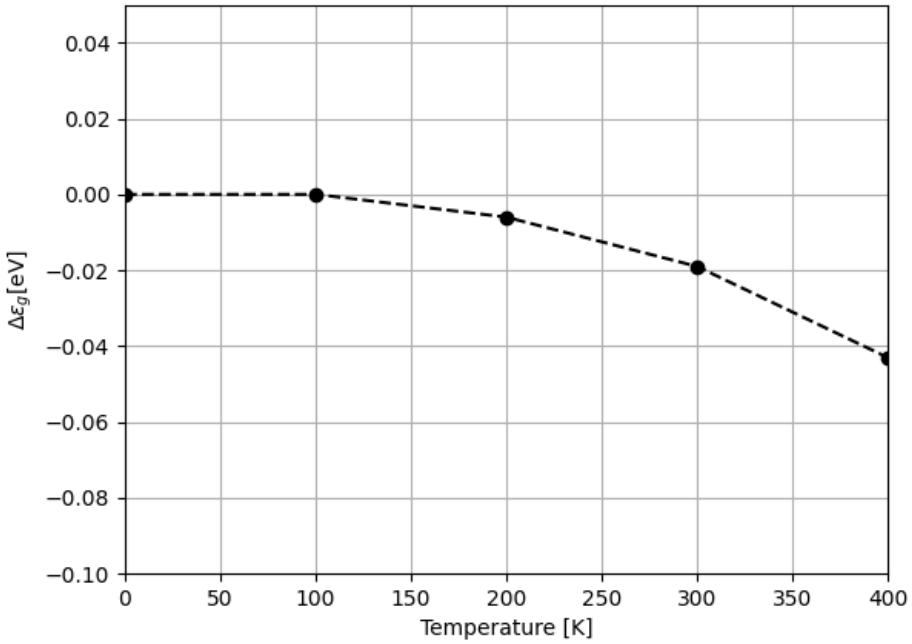

Figure 58: Temperature dependence of the band gap for BP. The dotted black line is the temperature dependence due to both lattice expansion and EPI (computed in this work).

As it can be expected, the BP band gap temperature dependance has a very flat behavior, due to its important Debye Temperature Θ_D. Unfortunately, no experimental data were found to compare the simulations and real-life samples.

6 Conclusion

In this work, the zero-point renormalization and temperature dependence for several semiconductors were investigated via their two main contributions : the zero point lattice expansion and the zero point renormalization from electron-phonon interaction. The zero point lattice expansion has been studied within the quasiharmonic approximation with volume-constrained zero static internal stress approximation as the reference volume. The minimal Gibbs energy was found using a fourth degree polynomial expression, from which the volumetric temperature dependence is deduced (and, from that, the zero point lattice expansion and its contribution to the band gap). The zero point renormalization from electron phonon interaction was studied from the adiabatic AHC formalism, theoretically identifying the Fan-Migdal term and the Debye-Waller term of the self-energy. The Kohn-Sham band gap was then corrected with the 'on-the-mass-shell' approximation for both the maximum of the valence band and the minimum of the conduction band. Extensive convergence studies were done to find the ZPR from EPI within the smallest error range possible. Summing the ZPLE and the ZPR from EPI, the total zero point energy was found for a set of ten semiconductors, with varying structures and properties. For few materials, the relative temperature dependence of the band gap was computed and compared to experimental data.

While the initial structural relaxation of the unit cells found very similar lattice parameters to the experimental ones (for most of the material the error is below 1%), the Kohn-Sham electronic band structure calculations were an underestimation of the reality. This is a known problem within the DFT formalism, partially solved by the use of GW approach. GW Perturbation Theory (GWPT) includes the EPI to compute the linear response of materials to perturbations (not used in this work). For the few cases where the band gap was null, artificial pressure has been applied on the structure to open its band gap.

The ZLPE was found to be on the order of few tens of percent of the lattice constant for each material except for ϵ - GaSe and ϵ - InSe for which the v-ZSISA quasiharmonic approximation shows that the phonon contribution to the volume increase is too important with regard to the Born-Oppenheimer volume. This was probably because of their strong anisotropy not well described within the v-ZSISA QHA. For the other materials, the ZPLE band gap contribution was in the range between [6;68] meV.

The ZPR from EPI was computed as well for different q point grid and several linear extrapolations (with the Fröhlich correction) were used to determine the most numerically accurate value with its error range. The relative error determines within what range the final ZPR value can be trusted. For most of the material, the relative error is below 10 %, meaning the computations were converged. However, when comparing our simulations with experimental values, both for the zero point total energy or for the temperature dependence of the band gap (for certain materials), the results obtained did not quite match. For InAs and InP, a factor of 2 was reported. This was troubling since the simulations are numerically converged. One possible explanation is that the inaccurate extraction method from which the experimental zero point energy is obtained (from the slope of the band gap temperature dependence) induces an error in its value. In addition, experimental values are scare in scientific literature since the zero point energy level is not a figure of merit in any technology and its knowledge does not have any impact other than theoretical (only its contribution to the total band gap is important).

One of the biggest inconvenience of this type of first principles calculations is the time taken for the DFPT computation. There is a trade-off to be found between the wanted accuracy and the time one is willing to take to get a result. This time problem can be reduced when working with the proper infrastructure and optimizing the computational resources but to a certain extent. One recent alternative to this long and computationally demanding phonon spectrum calculation could be to use machine learning prediction. In some promising studies, authors reported a two orders of magnitude acceleration compared to first principles calculations (but it come at the cost of accuracy and numerical precision)[77], [78], [79].

A Electronic Structures

This section gathers all KS electronic structures obtained.

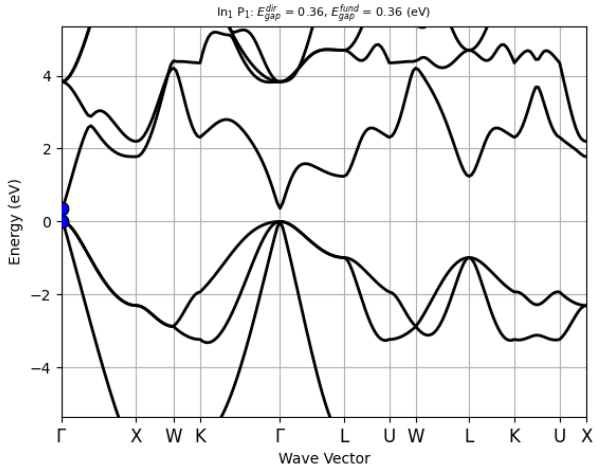

(a) InP

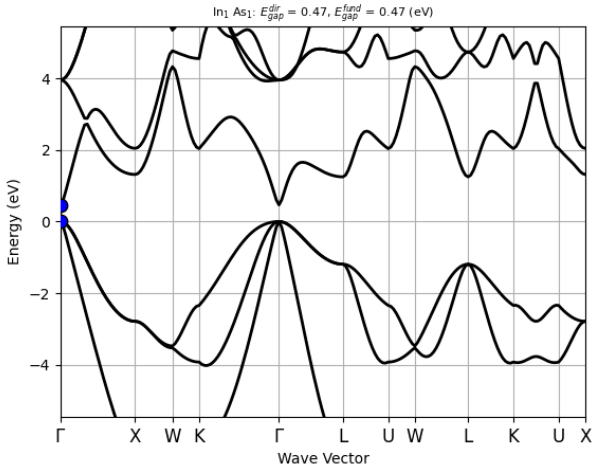

(b) InAs

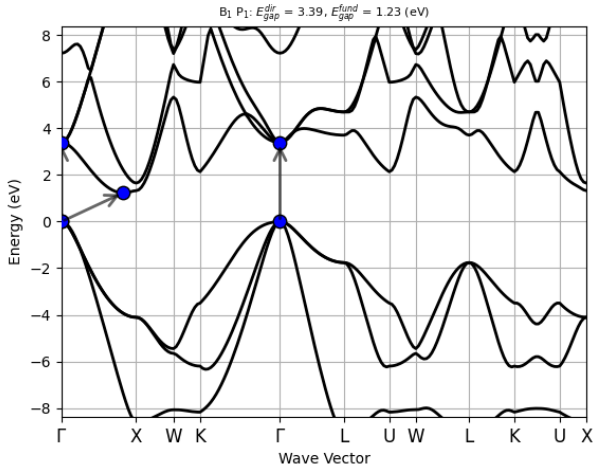

(c) BP

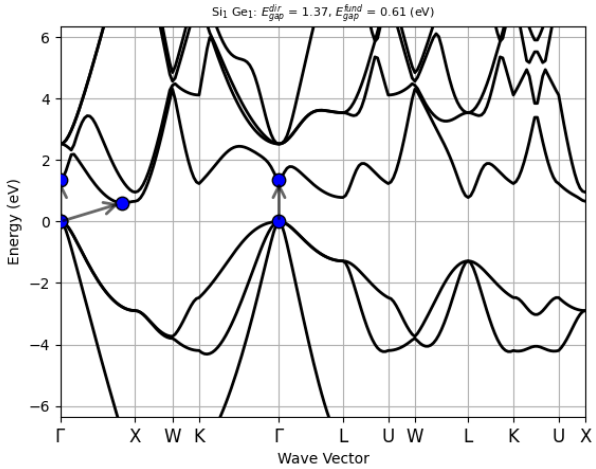

(d) SiGe

Figure 59: KS electronic band structures for InAs, InP, BP, SiGe

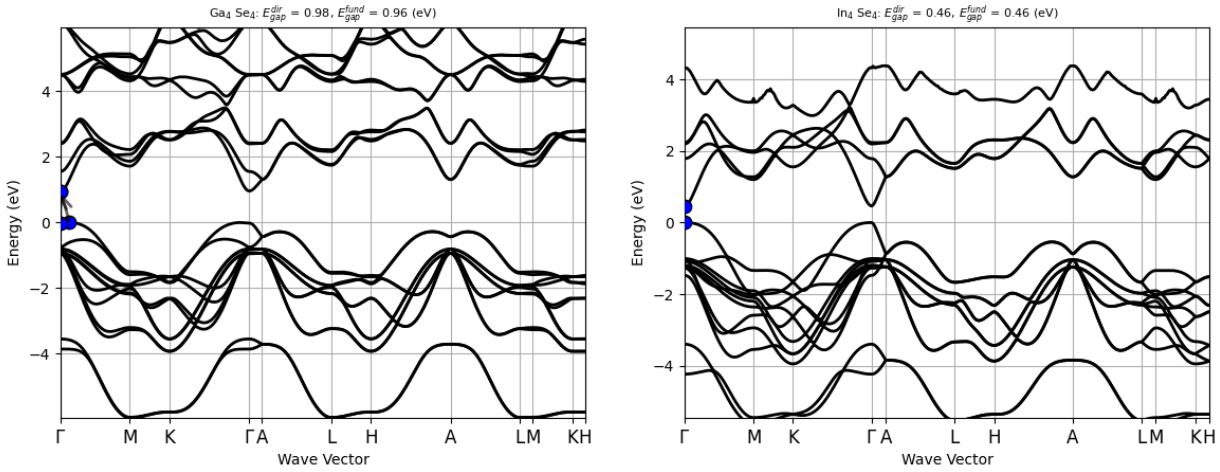

(a) GaSe (b) InSe

Figure 60: KS electronic band structures for GaSe, InSe

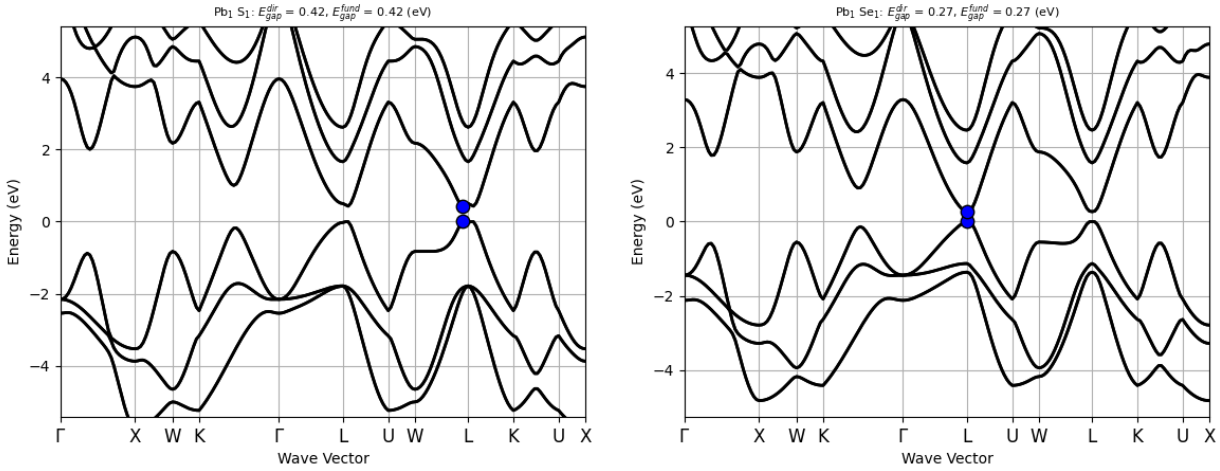

(a) PbS (b) PbSe

Figure 61: KS electronic band structures for PbS, PbSe

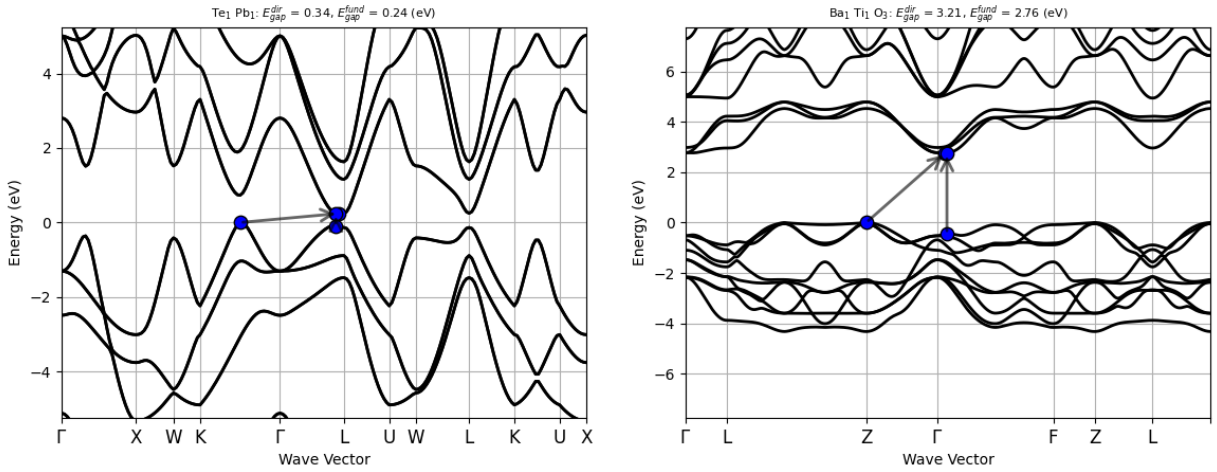

(a) PbTe (b) BaTiO3

Figure 62: KS electronic band structures for PbTe and BaTiO3

B Phonon density of state

This section gathers all phonon density of state for fully relaxed structures without pressure.

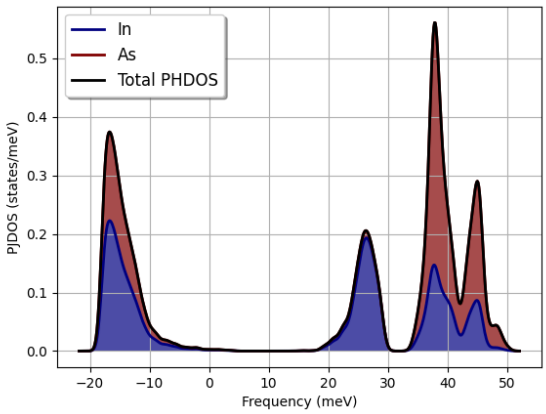

Figure 63: InAs

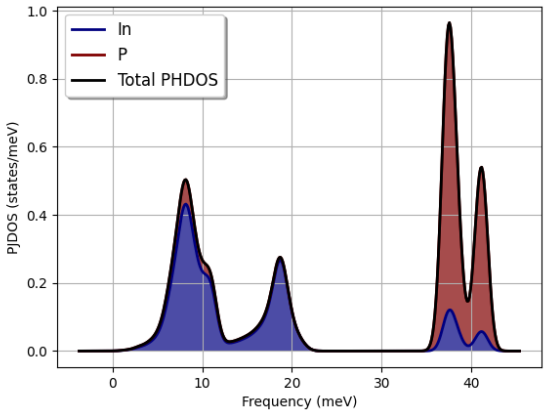

Figure 64: InP

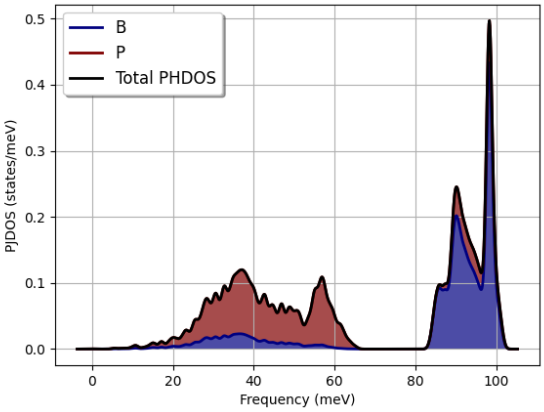

Figure 65: BP

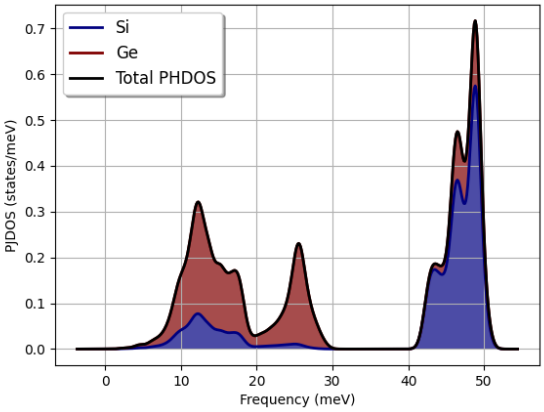

Figure 66: SiGe

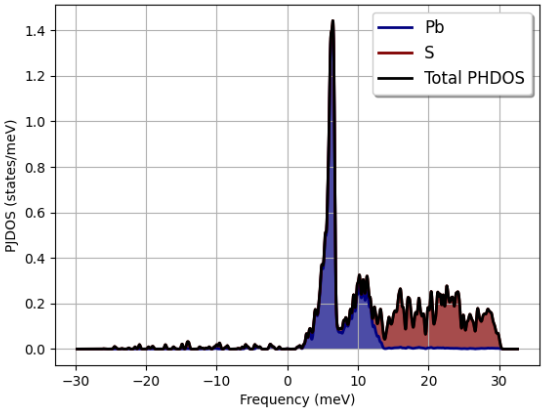

Figure 67: PbS

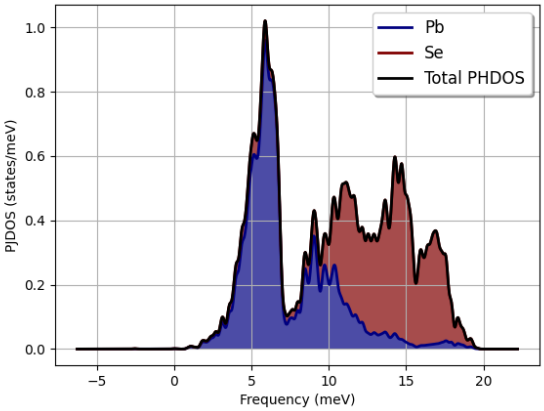

Figure 68: PbSe

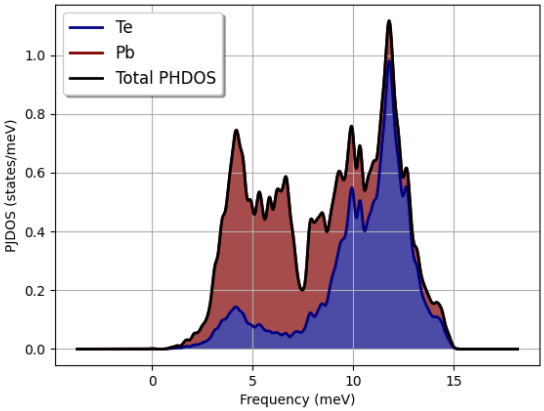

Figure 69: PbTe

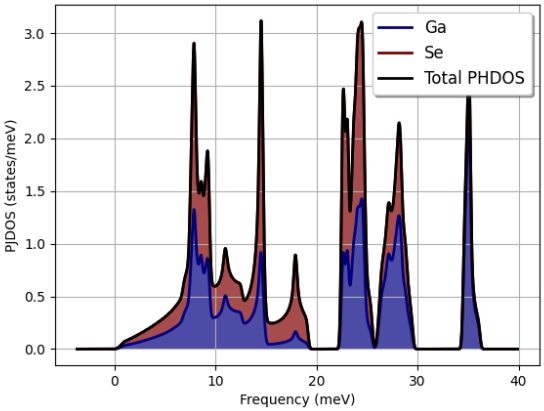

Figure 70: GaSe

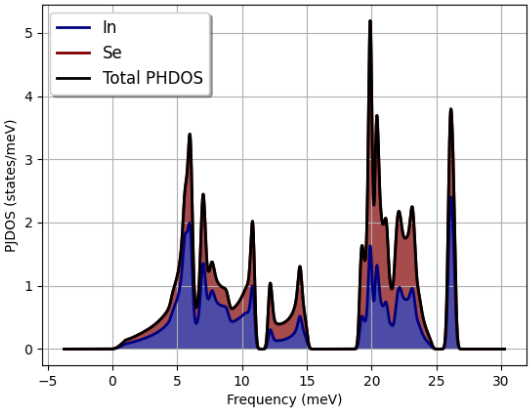

Figure 71: InSe

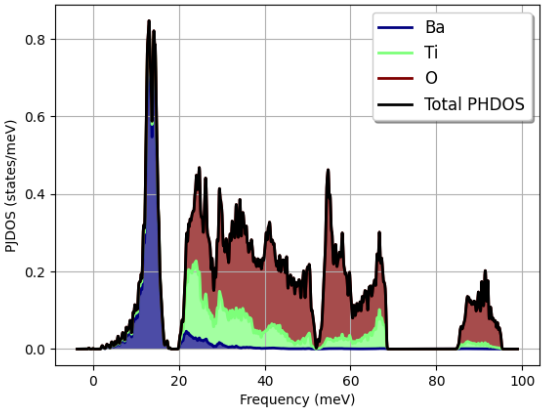

Figure 72: $BaTiO_3$

C ZPR Extraction

This section gathers the differents methods to extract the final value of the ZPR from EPI as well as the η convergence.

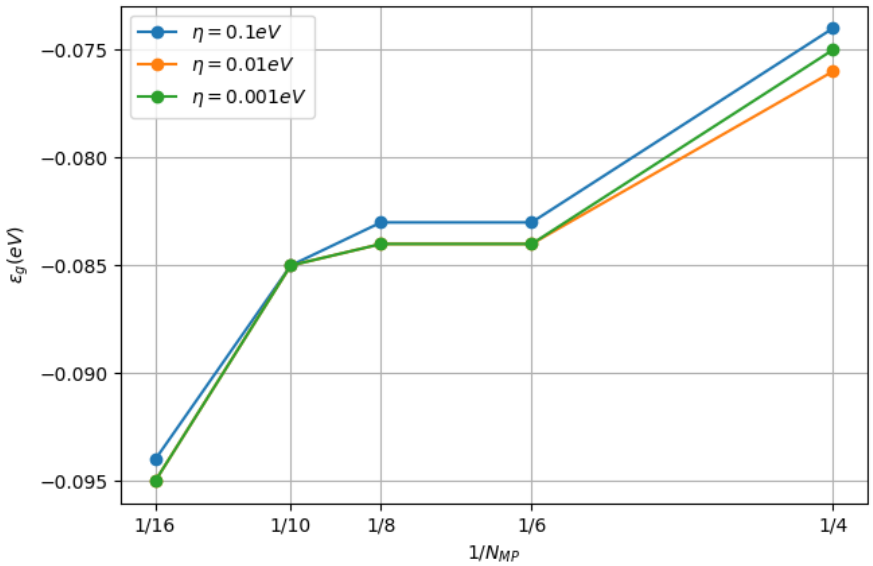

Figure 73: Convergence with respect to η for the InP

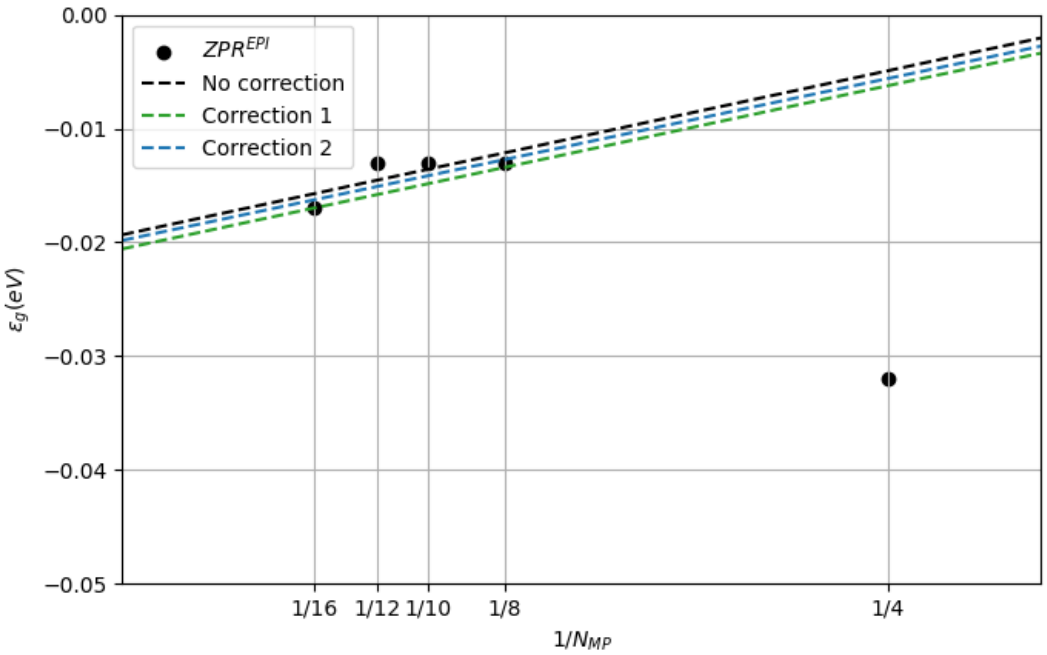

Figure 74: Zero point renormalisation as a function of the number of division in the BZ for InAs. The black dotted line is the simple linear extrapolation from the original ZPR points, corrected by the Fröhlich model, 'Correction 1' is the linear extrapolation passing through the most converged point and 'Correction 2' is the least square fitting method

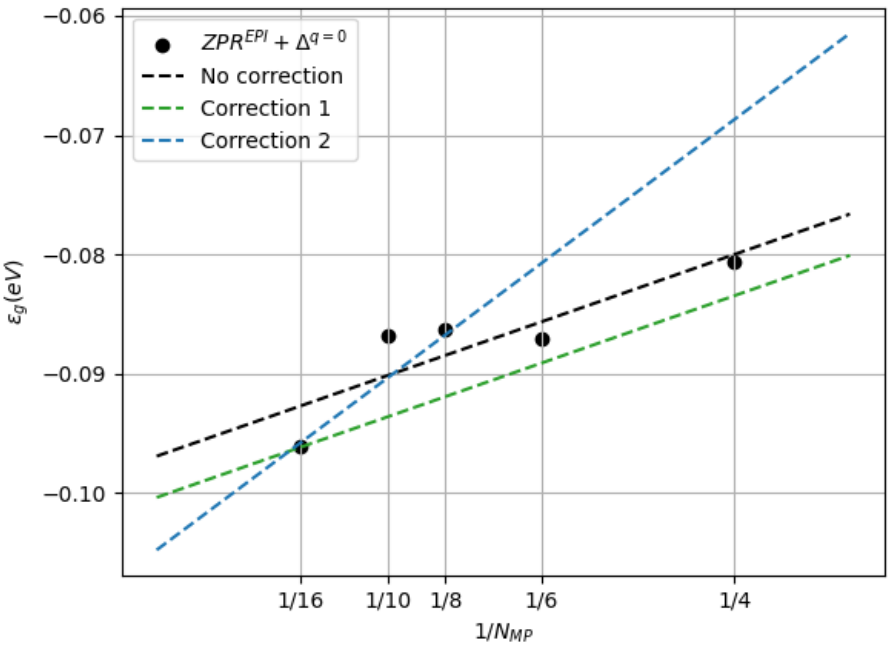

Figure 75: Same as fig 74, for InP

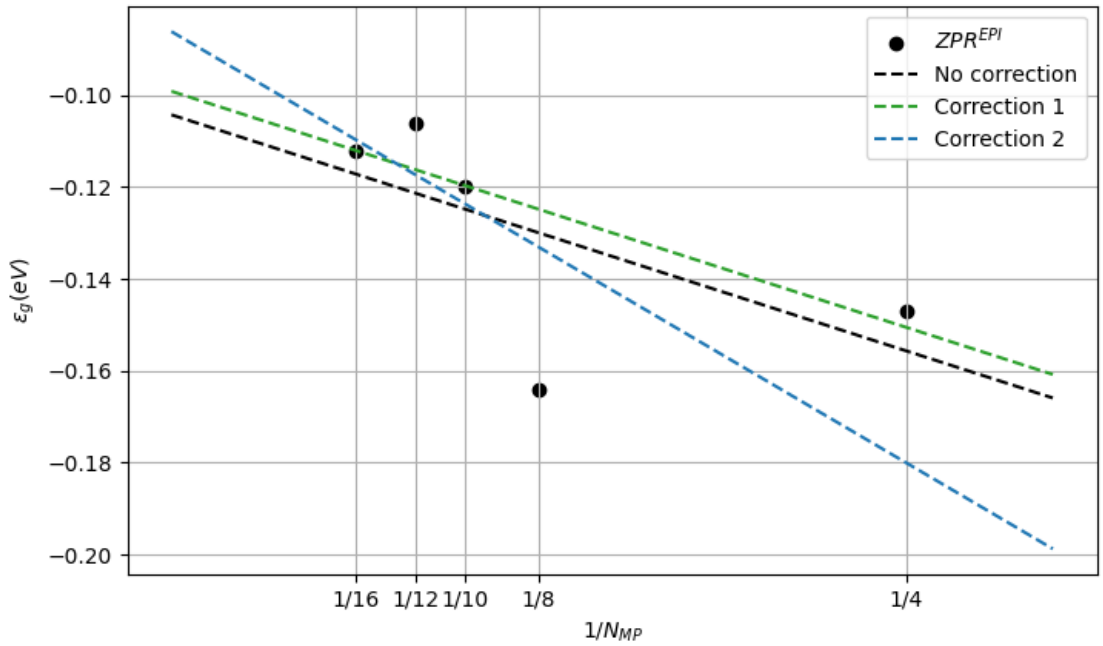

Figure 76: Same as fig 74, for BP

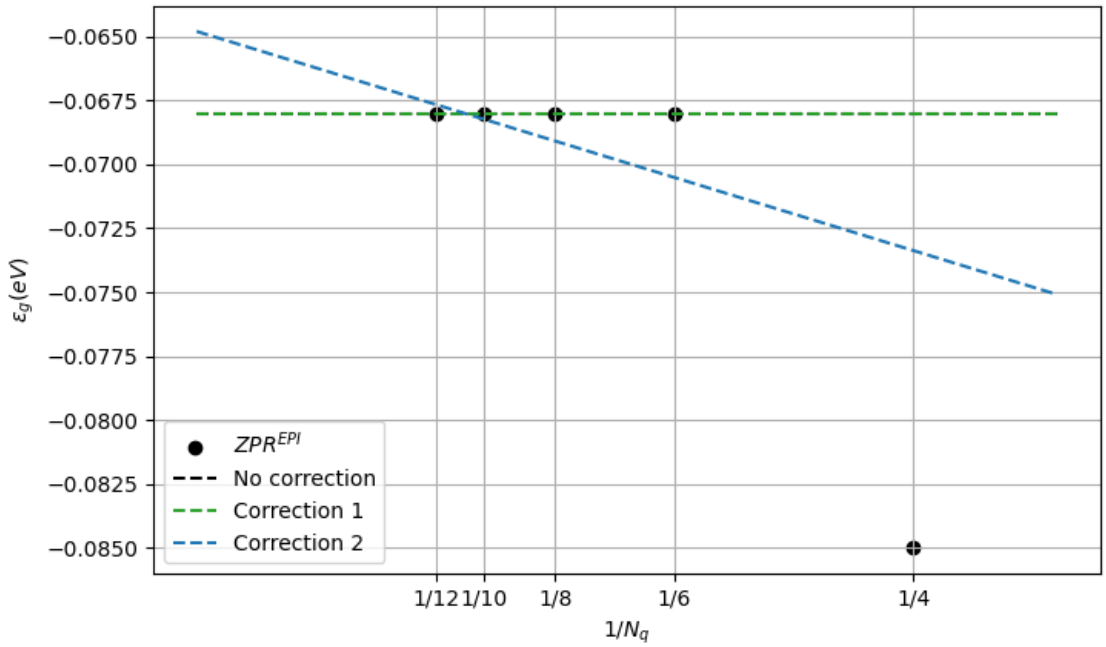

Figure 77: Same as fig 74, for SiGe

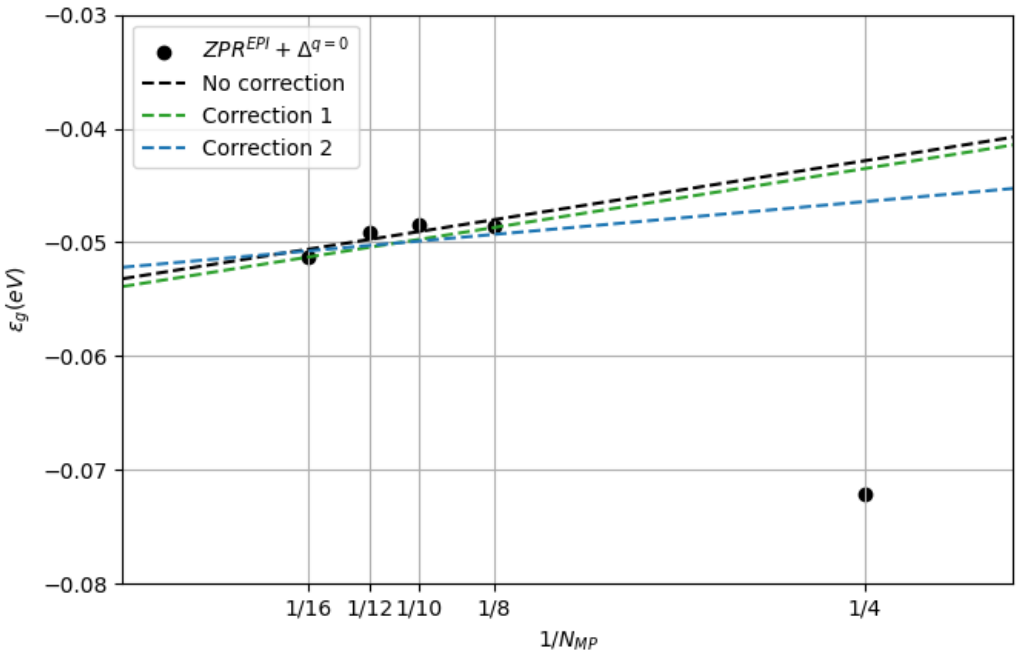

Figure 78: Same as fig 74, for PbS

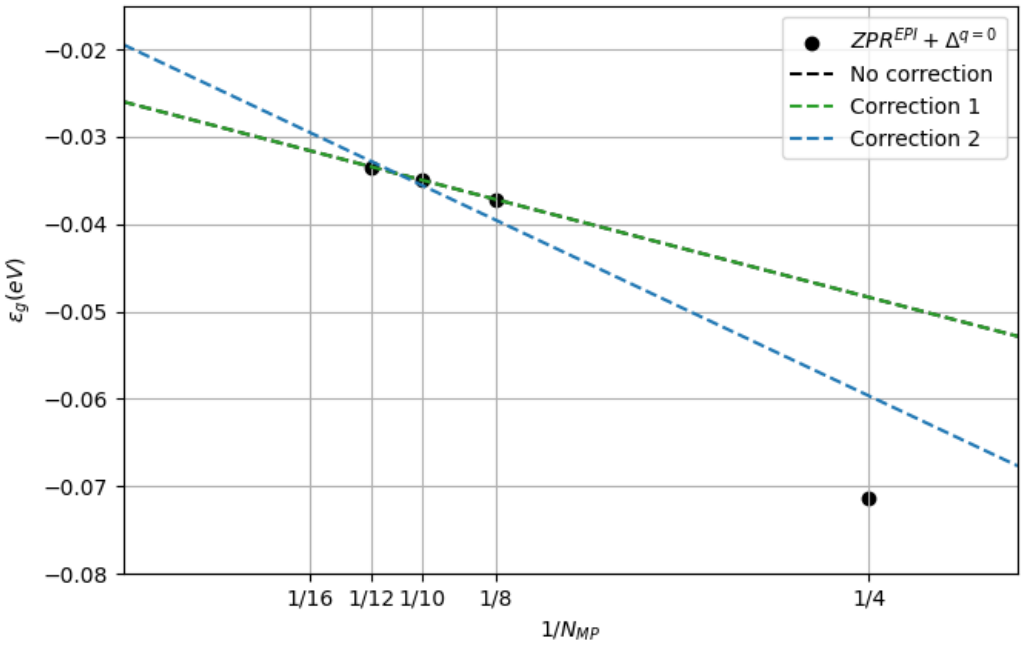

Figure 79: Same as fig 74, for PbSe

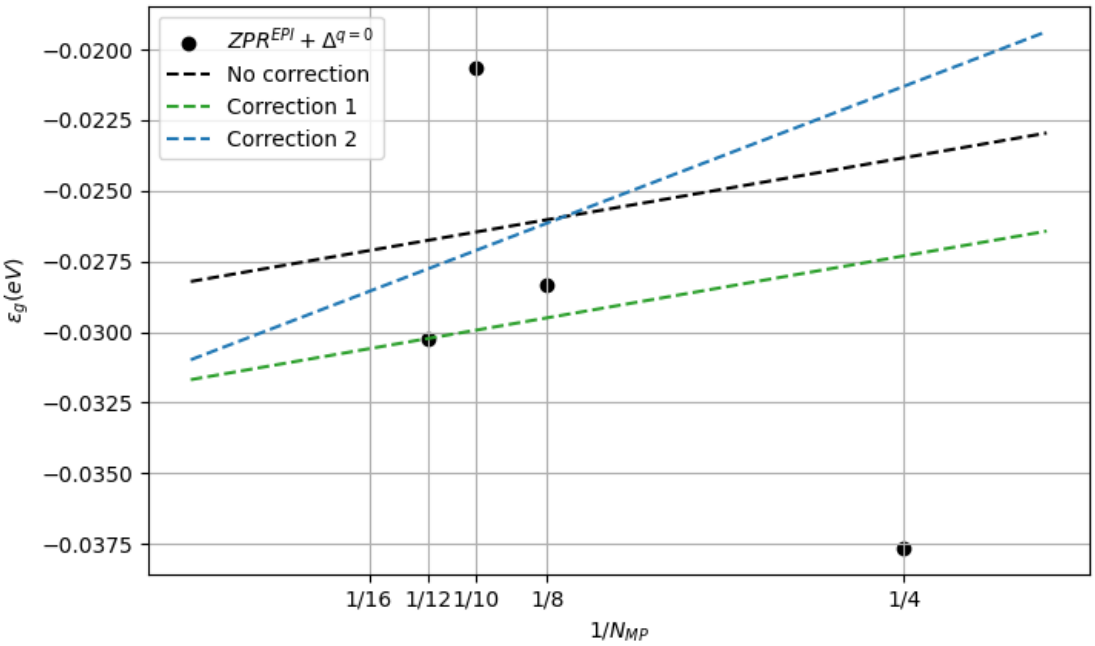

Figure 80: Same as fig 74, for PbTe

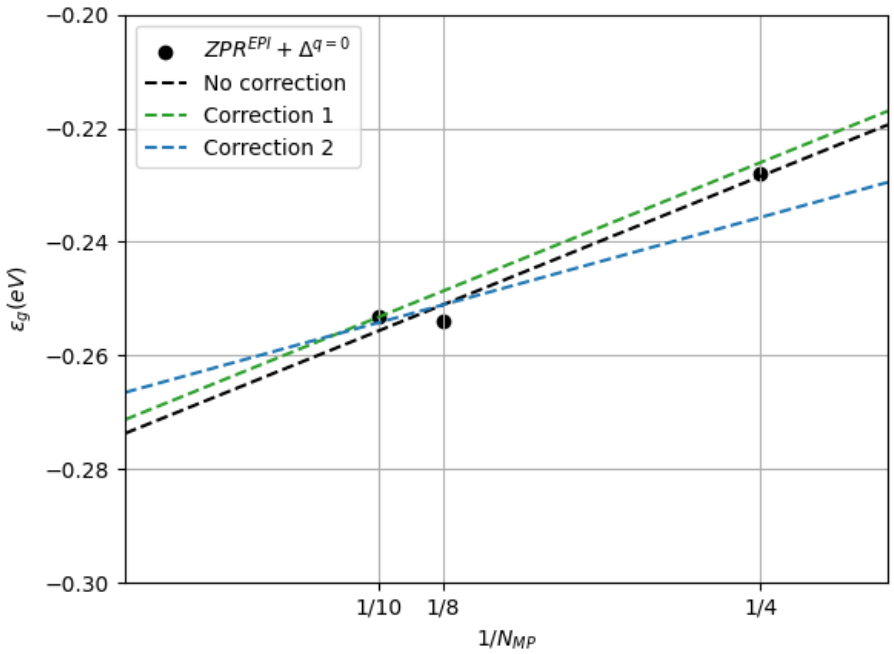

Figure 81: Same as fig 74, for GaSe

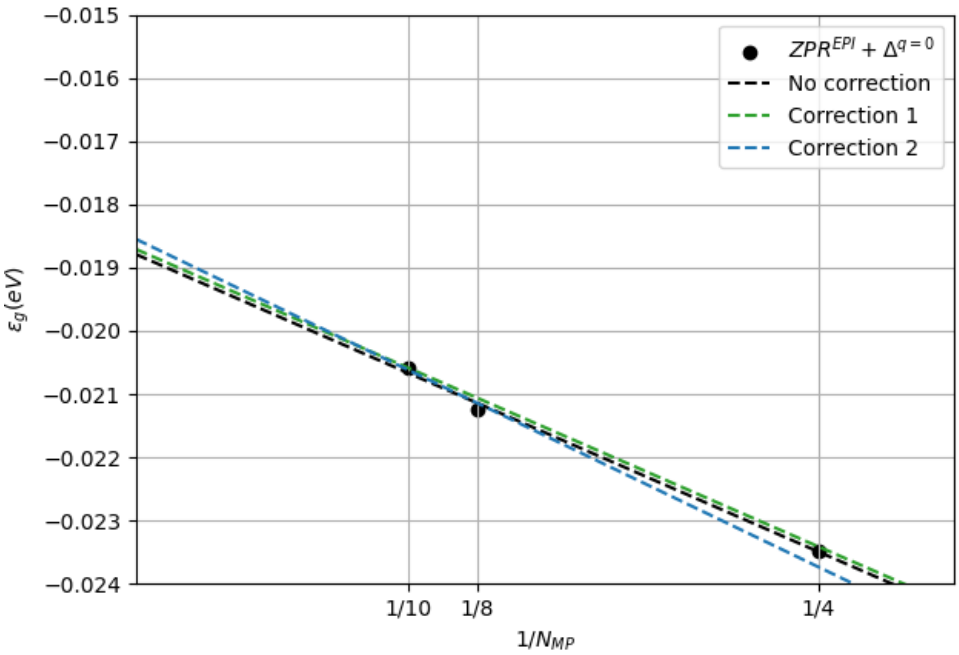

Figure 82: Same as fig 74, for InSe

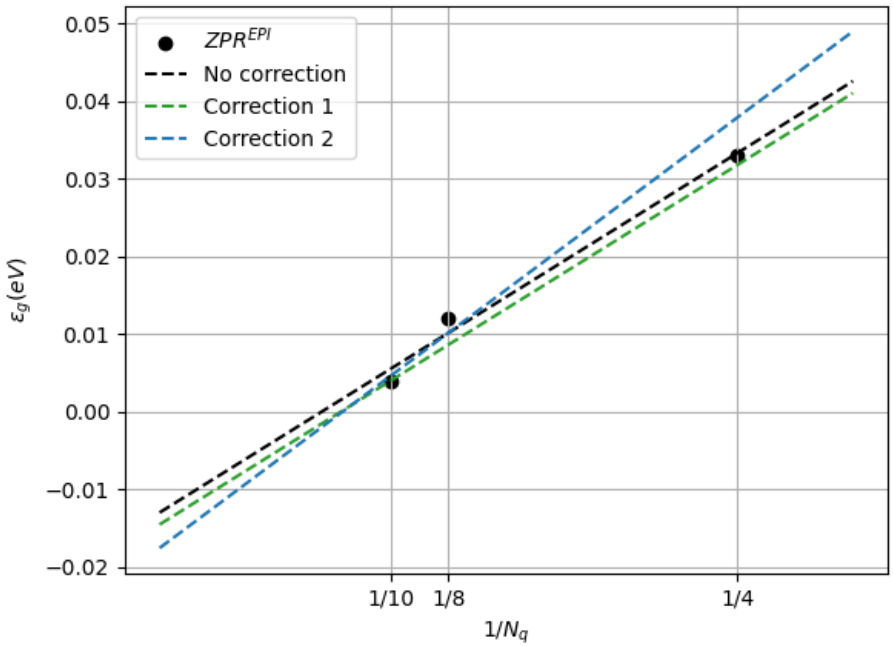

Figure 83: Same as fig 74, for $BaTiO_3$

D Temperature Dependence for InAs, InP, BP and SiGe

In this section, the graphs showing the different contribution of the ZPLE and ZPR from EPI for InAs, InP, BP and SiGe are plotted for a range of temperature from 0K to 700K

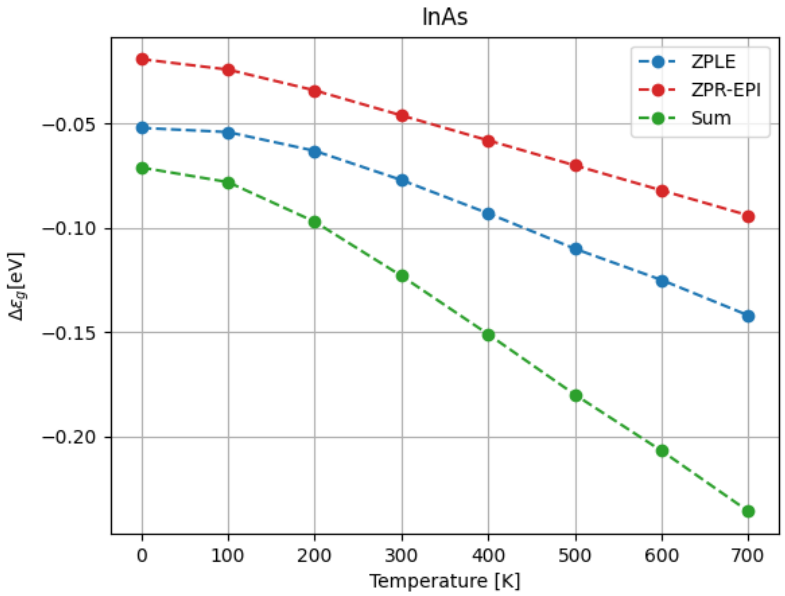

Figure 84: Temperature dependence of both the zero point lattice expansion and the zero point renormalisation from electron-phonon interaction for the InAs

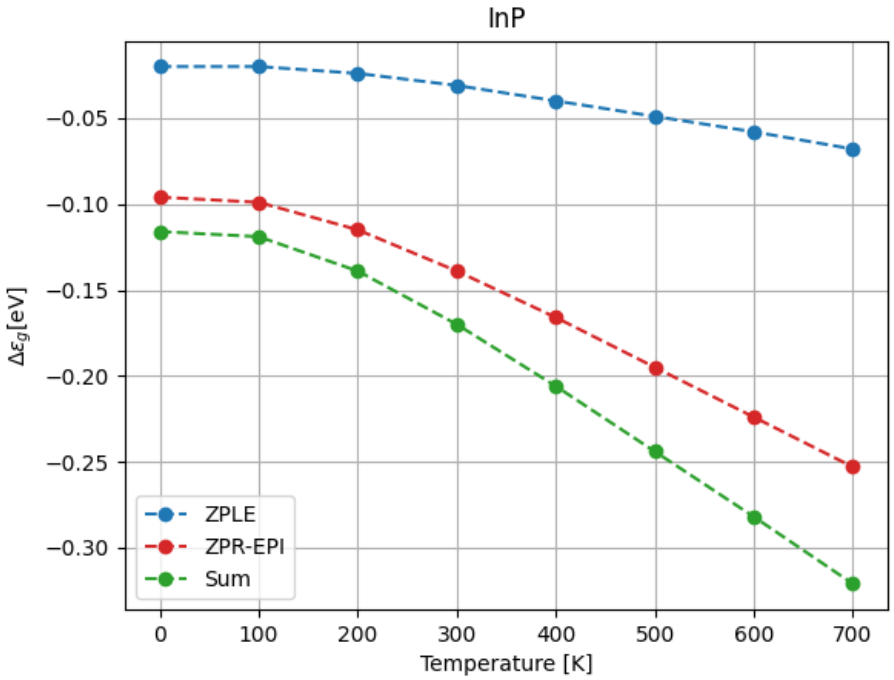

Figure 85: Same as fig. 84, for InP

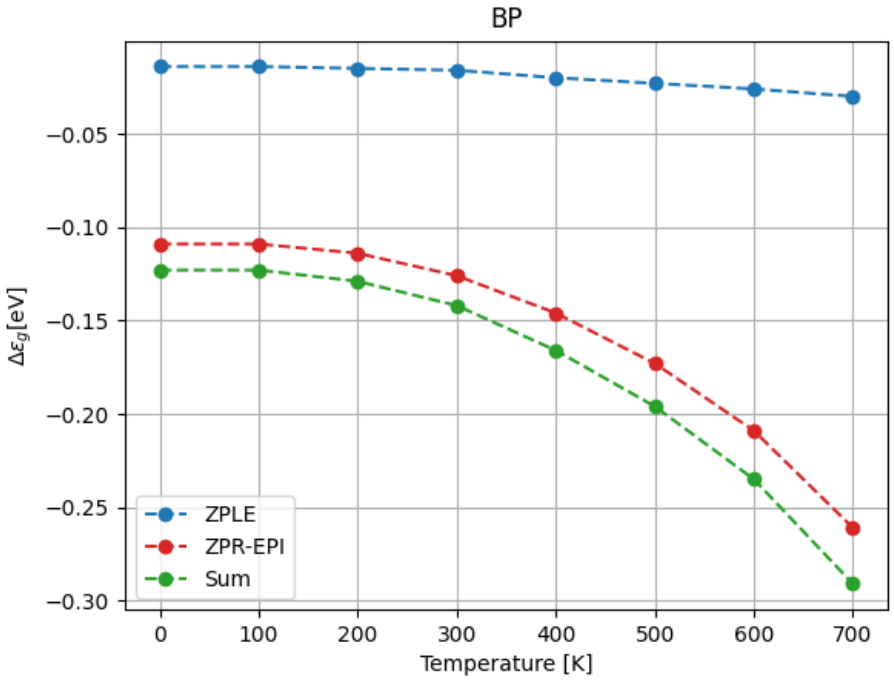

Figure 86: Same as fig. 84, for BP

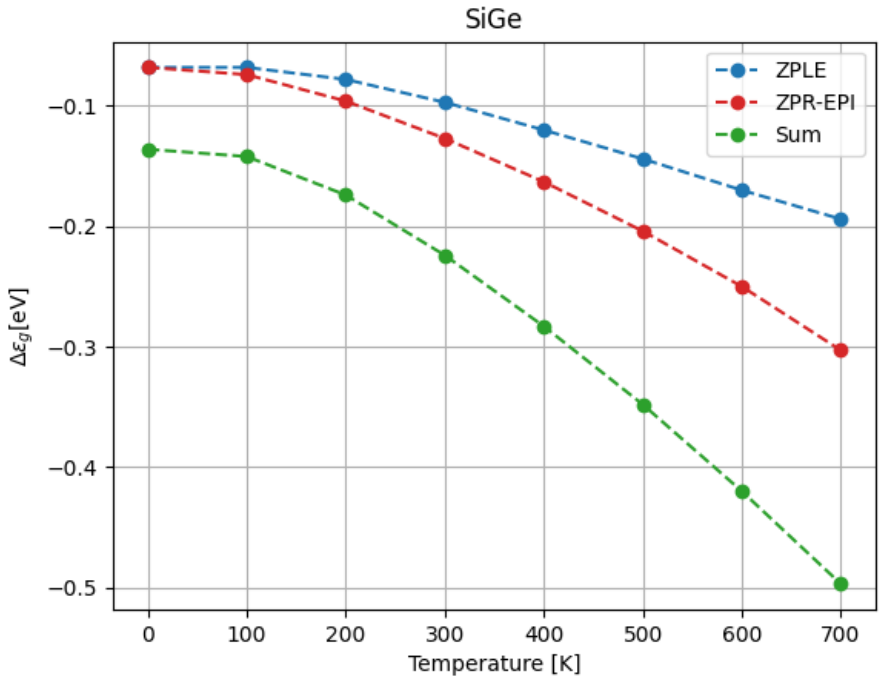

Figure 87: Same as fig. 84, for SiGe

References

[1] Renogy. *https://www.renogy.com/blog/ solar-panel-efficiency -and-cost-over-time/* (2024).

[2] Anubhav Jain et al. *APL Materials* **1**.1 (2013), 011002.

[3] John P Perdew. *International Journal of Quantum Chemistry* **28**.S19 (1985), 497–523.

[4] Samare Rostami and X. Gonze. *10.48550/arXiv.2407.08002* (July 2024).

[5] Y.P. Varshni. *Physica* **34**.1 (1967), 149–154.

[6] K. P. O'Donnell and X. Chen. *Applied Physics Letters* **58**.25 (June 1991), 2924–2926.

[7] A. Manoogian and A. Leclerc. *physica status solidi (b)* **92**.1 (1979), K23–K27.

[8] Roland Pässler. *Phys. Rev. B* **66** (8 2002), 085201.

[9] Wissam Saidi, Samuel Ponce, and Bartomeu Monserrat. *The Journal of Physical Chemistry Letters* **7** (Dec. 2016).

[10] W. Kohn and L. J. Sham. *Phys. Rev.* **140** (4A 1965), A1133–A1138.

[11] Diola Bagayoko. *AIP Advances* **4**.12 (2014), 127104.

[12] John P. Perdew, Kieron Burke, and Matthias Ernzerhof. *Phys. Rev. Lett.* **77** (18 1996), 3865–3868.

[13] M.J. van Setten et al. *Computer Physics Communications* **226** (2018), 39–54.

[14] Lars Hedin. *Phys. Rev.* **139** (3A 1965), A796–A823.

[15] P B Allen and V Heine. *Journal of Physics C: Solid State Physics* **9**.12 (1976), 2305.

[16] P. B. Allen and M. Cardona. *Phys. Rev. B* **23** (4 1981), 1495–1505.

[17] P. B. Allen and M. Cardona. *Phys. Rev. B* **27** (8 1983), 4760–4769.

[18] H. Y. Fan. *Phys. Rev.* **78** (6 1950), 808–809.

[19] H. Y. Fan. *Phys. Rev.* **82** (6 1951), 900–905.

[20] Harvey Brooks. Advances in Electronics and Electron Physics **7** (1955). Ed. by L. Marton, 85–182.

[21] P Güttinger. *Forces in molecules", Phys. Rev* **56** (1939), 340–343.

[22] S. Poncé et al. *Phys. Rev. B* **90** (21 Dec. 2014), 214304.

[23] Véronique Brousseau-Couture and Michel Côté (2021). Ed. by M. B. Paranjape et al., 305–313.

[24] Stefano Baroni et al. *Rev. Mod. Phys.* **73**.2 (2001), 515–562.

[25] Xavier Gonze. *Phys. Rev. B* **55**.16 (1997), 10337–10354.

[26] Feliciano Giustino. *Rev. Mod. Phys.* **89** (1 2017), 015003.

[27] Jean Paul Nery et al. *Phys. Rev. B* **97** (11 2018), 115145.

[28] Véronique Brousseau-Couture et al. *Phys. Rev. B* **106** (8 2022), 085137.

[29] L. Sirleto et al. Woodhead Publishing Series in Electronic and Optical Materials (2010). Ed. by Baojun Li and Soo Jin Chua, 61–96.

[30] Nicklas Anttu. *Crystals* **13**.9 (2023).

[31] Viet-Anh Ha et al. *Phys. Rev. Mater.* **4** (6 2020), 065401.

[32] R. J. Archer et al. *Phys. Rev. Lett.* **12** (19 1964), 538–540.

[33] Young-Kai Chen et al. ().

[34] J-P. Raskin. *LELEC2541 Advanced transistors UCLouvain* (2023).

[35] Kerstin Hummer, Andreas Grüneis, and Georg Kresse. *Phys. Rev. B* **75** (19 2007), 195211.

[36] G. Springholz et al. *Applied Physics Letters* **79**.9 (Aug. 2001), 1225–1227.

[37] Su-Huai Wei and Alex Zunger. *Phys. Rev. B* **55** (20 1997), 13605–13610.

[38] H Zogg and Akihiro Ishida. "IV-VI (lead chalcogenide) infrared sensors and lasers". *Infrared Detectors and Emitters: Materials and Devices*. Springer, 2001, pp. 43–75.

[39] Cheng-Long Zhang et al. *Phys. Rev. Mater.* **4** (9 2020), 091201.

[40] Alexandre Gouskov, Jean Camassel, and Léone Gouskov. *Progress in Crystal Growth and Characterization* **5** (1982), 323–413.

[41] V N Brudnyi, S Yu Sarkisov, and A V Kosobutsky. *Semiconductor Science and Technology* **30**.11 (2015), 115019.

[42] Ankur Gupta, Tamilselvan Sakthivel, and Sudipta Seal. *Progress in Materials Science* **73** (2015), 44–126.

[43] Mingjin Dai et al. *Advanced Materials Technologies* **7**.12 (2022), 2200321.

[44] Zhibin Yang and Jianhua Hao. *Advanced Materials Technologies* **4**.8 (2019), 1900108.

[45] Gopal Pethuraja et al. *Materials Sciences and Applications* **03** (Mar. 2012).

[46] Rubin Braunstein, Arnold R. Moore, and Frank Herman. *Phys. Rev.* **109** (3 1958), 695–710.

[47] O. Busch G. Vogt. *Helvetica Physica Acta* **33** (1960).

[48] J.F.W. Schiz et al. *Electron Devices, IEEE Transactions on* **48** (Dec. 2001), 2492–2499.

[49] K. Ismail, J. O. Chu, and B. S. Meyerson. *Applied Physics Letters* **64**.23 (June 1994), 3124–3126.

[50] Hailin Zhang et al. *Solar Energy* **233** (2022), 421–434.

[51] N.A. Noor et al. *Journal of Solid State Chemistry* **263** (2018), 115–122.

[52] Nurul Razak, Noriza Ahmad Zabidi, and Ahmad Rosli. *AIP Conference Proceedings* **1875** (Aug. 2017), 020017.

[53] Vandana B. Parmar et al. *Materials Today: Proceedings* (2023).

[54] Maryam Elmahgary et al. *Scientific Reports* **13** (Mar. 2023).

[55] Fan Yang et al. *Materials Research Bulletin* **96** (2017), 372–378.

[56] Artemios Karvounis et al. *Advanced Optical Materials* **8** (Nov. 2020).

[57] X. Gonze et al. *Computational Materials Science* **25**.3 (2002), 478–492.

[58] D. R. Hamann. *Phys. Rev. B* **88** (8 2013), 085117.

[59] O. E. Oyewande et al. *IOP Conference Series: Earth and Environmental Science* **655**.1 (2021), 012045.

[60] Seung-Hwan Kim and Sheng S. Li. *Physica E: Low-dimensional Systems and Nanostructures* **16**.2 (2003), 199–208.

[61] Víctor Mendoza-Estrada et al. *Revista Facultad de Ingeniería* **26**.46 (2017), 81–91.

[62] R.W.G. Wyckoff. *Krieger* **Malabar** (1986).

[63] A. Baida and M. Ghezali. *Computational Condensed Matter* **17** (2018), e00333.

[64] H. Weiss (Eds.) O. Madelung M. Schulz. *Springer, Berlin/Heidelberg/New York* **Science and Technology**.17 (1982).

[65] Humaira Takia et al. *International Journal of Physics* **10**.2 (2022), 102–110.

[66] K H Hellwege; O Madelung; M Schulz; H Weiss; W Freyland. *Crystal and solid state physics. Semiconductors.* **17, Subvolume F**.Springer Verlag (1983).

[67] Hannan Elsayed Sadek Abdelgelil. "Electronic and thermoelectric properties of InSe, GaSe and InGaSe2 superlattices". PhD thesis. Facultat de Fsica, 2017.

[68] Robert A. Evarestov and Andrei V. Bandura. *Journal of Computational Chemistry* **33**.11 (2012), 1123–1130.

[69] Benoit Van Troeye, Marc Torrent, and Xavier Gonze. *Physical Review B* **93**.14 (2016), 144304.

[70] Benoit Van Troeye et al. *Phys. Rev. B* **95** (2 2017), 024112.

[71] Srinivasan et al Krishnamurthy. *Applied Physics Letters* **47**.2 (July 1985), 160–162.

[72] Roland Pässler. *physica status solidi (b)* **236**.3 (2003), 710–728.

[73] Jonathan M. Skelton et al. *Phys. Rev. B* **89** (20 2014), 205203.

[74] Attilio Zilli et al. *ACS nano* **9** (Mar. 2015).

[75] L. Pavesi et al. *Phys. Rev. B* **44** (16 Oct. 1991), 9052–9055.

[76] Peiji Geng et al. *Journal of Physics D: Applied Physics* **50** (Sept. 2017).

[77] Ziqi Guo et al. *npj Computational Materials* **9**.1 (2023), 95.

[78] AN Filanovich and AA Povzner. *Metallurgical and Materials Transactions A* **52** (2021), 4290–4298.

[79] Yulou Ouyang et al. *Physical Review B* **105**.11 (2022), 115202.

UNIVERSITÉ CATHOLIQUE DE LOUVAIN
École polytechnique de Louvain
Rue Archimède, 1 bte L6.11.01, 1348 Louvain-la-Neuve, Belgique | **www.uclouvain.be/epl**